Study of the morphology effect of MnO_2 on Carbon dot-based nanosensor for the detection of biomolecules

Thesis submitted in fulfillment of requirements

for the degree of

Doctor of Philosophy

by

Neeraj

(Regn. No: 901909023)

Under the supervision of

Dr. Soumen Basu
(Professor)

Dr. Banibrata Maity
(Assistant Professor)

SCHOOL OF CHEMISTRY & BIOCHEMISTRY

THAPAR INSTITUTE OF ENGINEERING AND TECHNOLOGY,

(Deemed to be University)

PUNJAB, INDIA

November, 2022

CERTIFICATE

This is to certify that thesis entitled "Study of the morphology effect of MnO_2 on Carbon dot-based nanosensor for the detection of biomolecules", being submitted by Ms. Neeraj in fulfilment of the requirement for the award of the Degree of Doctor of Philosophy in the School of Chemistry and Biochemistry, Thapar Institute of Engineering and Technology, Patiala, is a record of candidate's own independent and original research work carried out by her under my supervision and guidance. The matter presented in the thesis has not been submitted in part or full for the award of any degree in any other University or Institute. (Supervisors) Dr. Soumen Basu (Professor) and Dr. Banibrata Maity (Assistant Professor), School of Chemistry and Biochemistry Thapar Institute of Engineering and Technology Patiala- 147004, Punjab (India).

(Supervisor)
Dr. Soumen Basu
Professor
School of Chemistry and Biochemistry
TIET, Patiala- 147004, Punjab (India)

(Supervisor)
Dr. Banibrata Maity
Assistant Professor
School of Chemistry and Biochemistry
TIET, Patiala- 147004, Punjab (India)

(Head)
Dr. Satnam Singh
Professor
School of Chemistry and Biochemistry
TIET, Patiala- 147004, Punjab (India)

CANDIDATE'S DECLARATION

I, hereby declare that the work presented in the thesis entitled "Study of the morphology effect of MnO_2 on Carbon dot-based nanosensor for the detection of biomolecules", in fulfillment of the requirement for the award of the Degree of Doctor of Philosophy, School of Chemistry and Biochemistry, Thapar Institute of Engineering and Technology, Patiala, is an authentic record of my own work carried out under the supervision of Dr. Soumen Basu, Professor, and Dr. Banibrata Maity, Assitant Professor, School of Chemistry and Biochemistry, Thapar Institute of Engineering and Technology, Patiala, India. The matter embodied in this thesis has not been submitted in part or full to any other university or institute for the award of any degree in India or Abroad.

Neeraj

.....

Neeraj

ACKNOWLEDGMENT

First of all, I would like to thank the Almighty for giving me strength, patience, and courage to fulfil this project.

Through this section of thesis, I would like to express my heartiest thankfulness to all those who encouraged and supported me in many ways for the accomplishment of this study and made it an unforgettable journey for me. I would like to express my sincere thanks to my supervisors **Dr. Soumen Basu** and **Dr. Banibrata Maity** for allowing me to work on my Ph.D. under their guidance and continuous support. I would like to thank both the supervisors for encouraging and supporting me in each step of this study. I would like to thank Dr. Soumen Basu for giving me opportunity to work in CSIR project. I am also grateful to CSIR and TIET, Patiala for fellowship during my PhD journey.

I would like thank to **Prof. Prakash Gopalan**, Director, and **Prof. Rafat Siddique** Dean R & SP for financial support. Many thanks to **Prof. Satnam Singh**, Head of School of Chemistry and Biochemistry Thapar Institute of Engineering and Technology, Patiala for his ever-helping attitude and good wishes. I would also like to express my special regards to the members of my doctoral committee, **Prof. Satnam Singh**, **Prof. Bonamali Pal**, and **Prof. Puneet Sharma** for their perceptive comments, advices and scientific discussions. Special thanks to all the teaching faculty of the department for their cooperation and guidance. Special thanks to **Prof. Vijay Luxami** for lifetime facility. Also, special thanks to Mr. Chander Thakur, Mr. Hemant, Mr. Shekar, Mr. Vishwanath, and office staff Mr. Mayank Sharma for their cooperation and timely support.

I want to thank everyone who helped with instrumental facilities; TIET Patiala, SAI labs, CeNS Bengaluru, LPU Jalandhar, IIT Roorkee, and Sprint Testing Solutions. I warmly thank to my senior **Dr. Shagun Kainth** who supported me and was always a part of the discussion of my work. I, especially, want to acknowledge a special person, **Dr. Surbhi Sharma,** whom I met very late in life during my Ph.D. journey. She has an unmatchable and inspiring personality who has taught me how to find positivity in difficult times and always encouraged me to rock in every aspect. I would like to thank **Dr. Aanchal Rathi,** my friend as well as my senior in lab. She helped me a lot in various problems and always supported me during my PhD journey. Special thanks to **Aayushi Kundu** who always supported and motivated me as a younger sister. I also want to thank **Shelly** and **Mansi Kapoor** for great time and moral support. I want to thank my other lab mates **Dr. Divya Monga, Aashna, Anushka Garg, Ranjeet Kumar Jha,**

Zaid Bin Siddique, Pritam for co-operating with me. I would also want to acknowledge cute **Janis Goyal** for encouraging me with her smile. I will always be thankful to **Geetika and Manish Singla** for their precious friendship. Special thanks to **Rekha Thakur, Rohini, Palak Sharma, Saurabh, Priya Kamboj, Sunidhi Sharma, Mandeep Kaur, Sakshi, Hemant, Komal, Aashima, Simran, Sonali** whose smiling faces always inspired me.

My heartful gratitude to my grandmother **Mrs. Savitri Devi** for her love and blessings. I will be always grateful to my father **Mr. Mulkh Raj** and my mother **Mrs. Manjit Kaur** for their unconditional love which I would never be able to pay back. I thank them for giving me opportunity to pursue higher studies and encouraging me to do research. My warm thanks to my younger brother, **Sahil Sohal,** who is a strong pillar of strength in my research journey. He never let me fall and I always had his back and I know that he would be the happiest to see me touching height of success. I also thank to my other family members.

I want to acknowledge the special person in my life whom I admire the most **Mr. Parminder Singh**. He supported me in each step and each day of my Ph.D. journey. I feel very lucky and blessed to have him in my life. He was always motivated to focus on my work and inspired me to have big dreams in life. The biggest credit for my success and accomplishments goes to him.

Besides this, I am thankful to everyone who knowingly and unknowingly helped me with the successful completion of this work.

Neeraj

.....

Neeraj

TABLE OF CONTENTS

Chapter 3

Morphology-Dependent Performance of MnO_2 Nanostructure Carbon Dots-Based Biosensors for the Detection of Glutathione

Chapter 4

Deciphering the Mechanism of Inner Filter Effect on Heteroatom Doped Carbon dots-MnO_2 Nanoprobe for Selective Detection of Glutathione

Chapter 5

Morphology Effect of 1-D MnO_2 Nanostructure on Heteroatom Doped Carbon Dots Based Biosensor for Selective Detection of Glutathione

Chapter 6

Transformation of Bulk MnO_2 to Fluorescent Quantum Dots for Selective and Sensitive Detection of Ferric ions and Ascorbic acid by Turn-Off-On Strategy

ABSTRACT

The thesis entitled "**Study of the morphology effect of MnO_2 on Carbon dot-based nanosensor for the detection of biomolecules**" is divided into six chapters.

Chapter-1. It describes the background of sensor, nanosensor, and fluorescent nanomaterials along with literature survey and scope of the work. This Chapter explains the detail information about the carbon dots (Cdots) with its synthesis approaches, fluorescence mechanism, optical properties, and effect of heteroatom doping. The different fluorescence quenching mechanisms of Cdots in the presence of quencher and different photophysical parameters were also discussed in this Chapter. The exceptional properties of MnO_2 and its different morphologies available were also described in this chapter. The importance of biomolecules in living beings and their need for detection by fluorescent probe was explained.

Chapter-2. A fluorescent nanosensor based on carbon dots and different-size MnO_2 nanospheres has been synthesized for rapid detection of glutathione (GSH). Water-soluble and highly fluorescent Cdots were prepared by the microwave method using ascorbic acid as the precursor. MnO_2 nanospheres of different sizes (large, medium, and small) were prepared by varying the concentration ratio of methionine and $KMnO_4$ at room temperature, which was confirmed by HRTEM analysis. The different sizes of MnO_2 nanospheres in Cdots result in quenching of the fluorescence intensity, quantum yields, and average lifetime values, which suggest that the fluorescence resonance energy transfer mechanism occurs between the Cdots and MnO_2 nanospheres. The variations of all the photophysical parameters and fluorescence turn off properties of Cdots are significantly tuned depending on the size of the nanospheres. Moreover, detection of GSH in the presence of different-size Cdots@MnO_2 systems has been explored. GSH causes the redox reaction in the presence of MnO_2, which leads to transformation from MnO_2 to Mn^{2+}. As a result, fluorescence restoration (turn-on) of Cdots was observed. The large MnO_2 nanospheres showed the lowest detection limit of 15 µM for GSH. The synthesized sensing system was very fast, simple, economical, and environmentally-friendly for the detection of the GSH level.

Chapter-3. A facile, sensitive, and selective fluorescent nanosensor for the detection of GSH. In this protocol, Cdots with a high quantum yield were synthesized by a microwave-assisted pyrolysis technique. Moreover, different shapes of the MnO_2 nanostructure were also prepared by the hydrothermal technique. A comparative photophysical study of different morphology-dependent Cdots@MnO_2 nanostructure-based biosensors was explored, which showed

different results for the quenching values of ("turn-off") fluorescence intensity, quantum yields, electron transfer rate, and average lifetime. The structure, property, and performance of nanomaterials are interdependent. Therefore, the different shapes of MnO_2, that is, nanoflowers (NFs), nanorods (NRs), and a mixture of NFs/NRs was prepared by the hydrothermal method owing to different specific areas (23-69 m^2g^{-1}) which put the impact on their sensing activity. It was observed that the variation in the different photophysical parameters of fluorescent Cdots such as quantum yield (ϕ), average lifetime values [τ_{av} (ns)], radiative (k_r) rate constant, non-radiative (k_{nr}) rate constant, rate of electron transfer (k_{ET}), the efficiency of electron transfer (ϕ_{EET}), FRET efficiency (E), and Förster distance (R_0) were dependent on the different shapes of the MnO_2 nanostructure. These results indicate that the transfer of energy occurs between the Cdots and different shapes of MnO_2 nanostructures based on fluorescence resonance energy transfer at different charge-transfer rates. The recovery rate ("turn-on") of fluorescence of Cdots with the addition of GSH was obtained best for the NF structure by conversion of MnO_2 to Mn^{2+}, and the limit of detection was obtained as ~19 μM for GSH. The developed sensing probes were rapid, easy, cheap, and eco-friendly for the determination of GSH.

Chapter-4. Heteroatom doping on Cdots is developed as an efficient approach to modify its optical and electronic properties. Herein, nitrogen-sulfur doped Cdots (N, S-Cdots)-MnO_2 nanospheres was used as "on-off-on" biosensor for the selective detection of glutathione (GSH) and also for intracellular imaging. N, S-Cdots have been synthesized through high-temperature treatment for 5 min. The value of quantum yield was evaluated to be high for the N, S-Cdots i.e., 73.42 %. N, S-Cdots showed very high fluorescence quenching efficiency in the presence of MnO_2 nanospheres due to the inner filter effect (IFE) and also showed the highest fluorescence recovery rate after the addition of GSH in the prepared system. N, S-Cdots-MnO_2 nanospheres as a sensing system satisfy the Parker equation to confirm the IFE as a quenching mechanism. No variation in the average lifetime values of N, S-Cdots after the addition of MnO_2 nanospheres confirms the IFE. MnO_2 nanospheres and GSH involves a redox reaction between them which leads to the removal of Cdots from MnO_2 nanosphere's surface and further, the fluorescence restoration of the Cdots was achieved. The limit of detection (LOD) for GSH was determined to be 80 nM. The heteroatom doping in the structure of Cdots has a significant role in the sensitive detection of GSH. The prepared-sensor is rapid, economical, less toxic, and highly applicable in diagnosing diseases.

Chapter-5. Structural versatility of MnO_2 nanostructures plays a significant role in biosensing applications. So, we have prepared simple and selective "turn-off-on" sensing probes for the

detection of GSH, based on nitrogen, sulfur co-doped carbon dots (N, S-Cdots) and different morphologies of one dimensional (1-D) MnO_2 nanostructures. N, S-Cdots with a high fluorescence quantum yield (73.42 %) were prepared by a green approach through high-temperature pyrolysis in just 5 min. The different morphologies of 1-D MnO_2 nanostructures (nanowires with varying aspect ratios and nanorods) were synthesized through a hydrothermal method by varying the reaction period (8, 10, and 12 h). MnO_2 nanowires prepared at 8 h showed a high specific surface area (34 m^2g^{-1}) with a large aspect ratio. They showed significant fluorescence quenching, Stern-Volmer constants, and binding constants in the presence of N, S-Cdots. Further, ultraviolet-visible absorption, zeta potential, and time decay studies showed that the quenching mechanism of the developed sensing system was the inner filter effect, which was further confirmed by using the Parker equation. The N, S-Cdots-MnO_2 nanowire (with a high aspect ratio) sensing system showed the best limit of detection, i.e., 28.5 µM for GSH. This fast, simple, eco-friendly, and cost-effective sensing system can be further used for real-time biosensing and bio-imaging application.

Chapter-6. MnO_2 nanostructure has a unique light absorption ability and redox feature, due to which it is mainly used as a fluorescence quencher. However, its quantum dots can also act as a self-fluorescent nanomaterial with exclusive properties for sensing applications. Therefore, a cheap and straightforward route for fabricating citric acid-functionalized MnO_2 quantum dots (CA-MnO_2 QDs) was proposed through one-step ultrasonication of bulk MnO_2 in the presence of citric acid as acidifying and stabilizing agent. The prepared CA-MnO_2 QDs exhibited high photostability, good water solubility, high photoluminescence (PL) stability from pH range 5 to 9, and significant fluorescence quantum yield value, i.e., 13.3 %. Further, CA-MnO_2 QDs was used for the detection of Fe^{3+} ions with a detection limit of 43 nM, based on dynamic quenching. The fluorescence quenching mechanism was confirmed by determining different photophysical parameters such as fluorescence quantum yield, average lifetime values, radiative constants (k_r), non-radiative rate constants (k_{nr}), rate of electron transfer (k_{ET}), and electron transfer efficiency (Φ_{EET}). The CA-MnO_2 QDs in the presence of Fe^{3+} was used for the detection of ascorbic acid with a detection limit of 90 nM based on the redox reaction between Fe^{3+} ions and AA. Furthermore, the developed sensing probe was also used to detect Fe^{3+} ions and AA in real samples, i.e., iron and AA supplements, respectively.

LIST OF FIGURES

Chapter 3

Chapter 4

Chapter 5

Chapter 6

LIST OF TABLES

Chapter 6

LIST OF SCHEMES

LIST OF ABBREVIATIONS

Cdots	Carbon dots
U-Cdots	Undoped carbon dots
N-Cdots	Nitrogen-doped carbon dots
S-Cdots	Sulfur-doped carbon dots
N, S-Cdots	Nitrogen, Sulfur-doped carbon dots
Q	Quencher
PL	Photoluminescence
QCE	Quantum confinement effect
IFE	Inner filter effect
FRET	Förster resonance energy transfer
PET	Photoinduced electron transfer
GSH	Glutathione
AA	Ascorbic acid
Cys	Cysteine
CA	Citric acid
MnO_2	Manganese oxide
0-D	Zero-dimensional
1-D	One-dimensional
2-D	Two-dimensional
3-D	Three-dimensional
NR	Nanorods
NT	Nanotubes
NW	Nanowires
NS	Nanospheres
NF	Nanoflowers
QDs	Quantum dots
LOD	Limit of detection
UV-Vis	Ultraviolet-visible
FTIR	Fourier transform infrared spectroscopy
TEM	Transmission electron microscopy
HRTEM	High resolution transmission electron microscopy

XPS	X-ray photoelectron spectroscopy
FESEM	Field emission scanning electron microscope
EDS	Energy-dispersive X-ray spectroscopy
XRD	X-ray diffraction
BET	Brunauer−Emmett−Teller
SAED	Selected area diffraction
TCSPC	Time-correlated single-photon counting
RSD	Relative standard deviation
IRF	Instrument response function
e.g.	Example
w.r.t.	With respect to
no.	Number
ES	Excited state
GS	Ground state

LIST OF SYMBOLS

µM	Micro-Molar
mM	Milli-Molar
nM	Nano-Molar
µl	Micro-Litre
ml	Milli-Litre
ns	nanosecond
M	Molar
ϕ	Fluorescence quantum yield
τ_{av}	Average lifetime
k_r	Radiative rate constant
k_{nr}	Non-radiative rate constant
k_{ET}	Rate of electron transfer
ϕ_{EET}	Efficiency of the electron transfer
R_0	Förster distance
r	Separation distance
E	FRET efficiency
λ_{ex}	Excitation wavelength
λ_{em}	Emission wavelength
J(λ)	Spectral overlap integral
F_{obsd}	Observed PL intensity
F_{cor}	Corrected PL intensity
mV	Milli-Volts
K_{SV}	Stern-Volmer constant
CF	Correction factor
A_{ex}	Absorbance at the maximum excitation wavelength
A_{em}	Absorbance at maximum emission wavelength
E_{obsd}	Observed suppressed efficiency
E_{cor}	Corrected suppressed efficiency

CHAPTER-1

Introduction and Literature

1.1 Background

1.1.1 Sensor

The sensor is a device that can sense the physical changes and alter them into signals (such as optical, electrical, and mechanical) that can be measured.[1] Sensor can be mainly divided based on the types of transducer used. The transducer is defined as a device that converts one type of energy into a readable signal.[2] There are majorly three kinds of transducers which are electrochemical, optical, and mechanical.[3] Figure 1.1 represents the working scheme of the sensor.

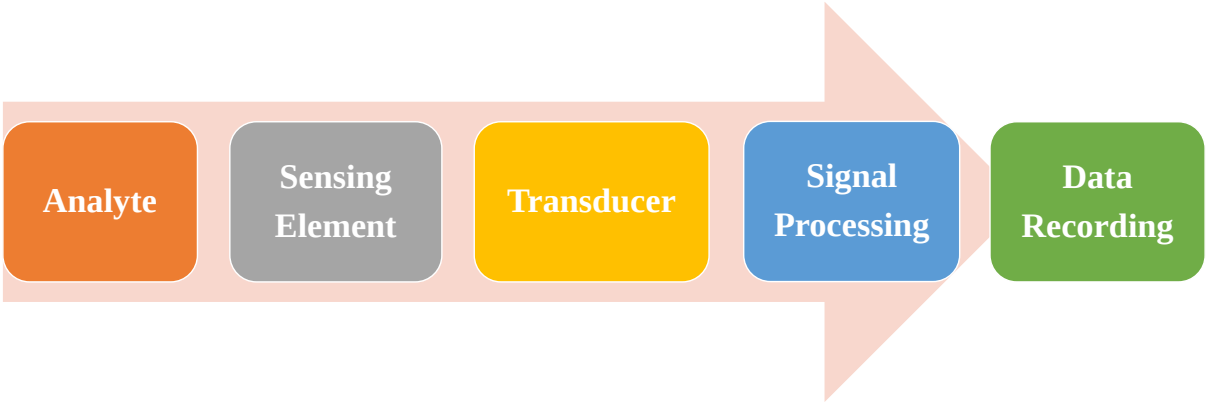

Figure 1.1: The working scheme of the sensor.[4]

1.1.2 Nanosensor

Advancements in the period of nanotechnology result in the construction of nanosensors. Nanosensor is a kind of sensor based on nanomaterials that can measure the change (such as physical, biological, chemical).[5,6] Nanosensors show specific behavior due to the presence of targeted ligands on the nanomaterials.[7] The functional groups present in the ligand attract the particular analyte and the nanomaterials participate in the sensitivity and alter the signals from one type to the another.[3] Nanomaterials can be defined as a material with having the smallest dimension in the range of 100 nm.[1] Nanomaterial showed very extraordinary properties in comparison with bulky ones. The natural intermolecular spacing and interaction between the molecules at the nanoscale level can be used in various sensing applications. There are many biological organisms like antibodies, viruses, proteins, bacteria, etc. in the nanometer range and they are called as nano-biological materials.[8] Nanomaterials can easily enter to the cells to resolve many problems. Nanosensors are also further classified

as electrochemical, optical, and mass nanosensors based on the type of transducer used. Nowadays, optical nanosensors are in great demand owing high sensitivity, good selectivity, and excellent detection capability. The optical nanosensor is based on the different optical techniques which are fluorescence, colorimetry, chemiluminescence, photoelectrochemistry, and resonance Rayleigh scattering.[9] Optical nanosensor measures absorbance, fluorescence, and Raman scattering. In case of optical techniques, study of samples can be recorded through the particular emission and excitation wavelengths of the exact target analytes.[10,11] Fluorescent nanosensors have many advantages such as exceptional sensitivity, rapid response, and simple operations, which enable their application in environmental monitoring, biological research, and diagnosis of diseases.[12]

1.1.3 Fluorescent nanosensor

A fluorescent nanosensor is based on the fluorescence optical detection technique. Many nanomaterials such as quantum dots, gold nanoparticles, fluorescent conjugated polymer nanoparticles, upconversion nanoparticles, etc. are used for the development of fluorescent nanosensors. The quantum dots based on semiconductors like CdSe and CdTe are synthesized by complicated methods and they have high toxic nature, poor stability, and very less biocompatibility. Metal nanoparticles like gold nanoparticles are highly expensive and less stable. There are different organic dyes available such as rhodamine, fluorescein, cyanine, and coumarin used in fluorescence nanosensors. These organic fluorescent dyes have many disadvantages such as low solubility, less biocompatibility, and high photobleaching.[13] Also, the fluorescent dyes have a narrow range of excitation which unsatisfied the requirement for different excitation wavelengths. Therefore, there is a need to develop environment-friendly material with excellent fluorescence properties, cheap, high stability, and good biocompatibility for the construction of fluorescent nanosensors. In recent times, carbon-based nanomaterials with significant properties are used as fluorescent probe for sensing applications.

1.1.4 Carbon dots (Cdots)

In recent times, Cdots are carbon nanomaterials that act as a proficient substitute for other fluorescent nanomaterials due to having exceptional biocompatibility, good water solubility, photo-stability, and tunable photoluminescence (PL).[14,15] Cdots are very small size fluorescent carbon nanomaterials with diameter below 10 nm.[16] The structure of Cdots contains mainly two parts including carbon core and surface defects (Figure 1.2).[17] Among many quantum dots (QDs) and fluorescent organic dyes, the Cdots showed high water solubility, good confront to photobleaching, strong chemical inert behavior, and simple modification.[18] Cdots show extraordinary physical, electronic, optical, and chemical properties due to their

specific structure which contains nanocrystalline cores with sp^2 carbon domains and further contains an amorphous carbon matrix (sp^3 hybridized).[19]

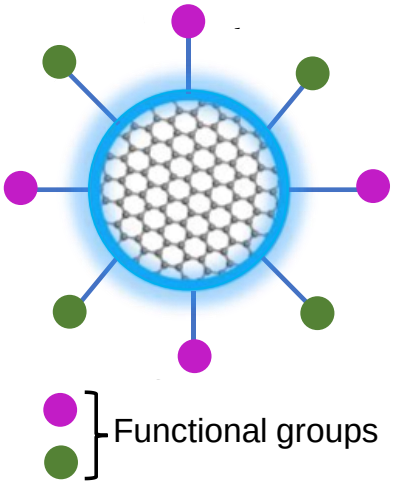

Figure 1.2. The structural depiction of Cdots.

The synthesis of Carbon dots can be divided into two methods i.e., "top-down" and "bottom-up". The "top-down" method includes the cutting of large carbonaceous resources like carbon nanotubes (CNTs), carbon black, graphite, carbon fibers, and many others. into small Cdots through different methods such as electrochemical, solvothermal treatment, acid treatment, and chemical oxidation. In contrast, the "bottom-up" method includes the carbonization or pyrolysis of small carbon sources for example citric acid, ascorbic acid, glucose, etc. by using hydrothermal treatment, microwave irradiations, and high-temperature treatment. The purification of the developed product can be done to obtain the Cdots with high purity and mono-dispersity through centrifugation, filtration, and dialysis bags.[20] The "top-down" approach produces the Cdots at a large scale but it shows many limitations like non-uniform size, severe synthesis method, low yield, and need for special conditions. While, the "bottom-up" approach showed high control on the different intrinsic properties such as size, lattice dimensions, the morphology of Cdots and also leads to the development of a large number of Cdots having an environmentally friendly nature. Cdots have unique electronic properties due to which they can donate and accept the electrons. This results in producing chemiluminescence and electrochemical-luminescence which make them applicable in different fields such as optronics, sensors, and catalysis.

1.1.5 Photoluminescence (PL) mechanism of Cdots

The origin of PL of Cdots depends upon various factors, for example, QCE, surface chemical group, and molecular fluorescence.[21] Cdots with many emissive colors were

developed by different routes till now, but their fluorescence mechanism is under debate. Generally, the fluorescence of Cdots is dependent upon the relationship between the sp^2 domains in the carbon core and surface functional groups. The size of quantum dots should be less than the exciton Bohr radius for QCE to be occur.[22] The QCE denotes the conversion of the valence band and the conduction band from the continuous energy band into discrete energy levels. Further, the band gap gets enhanced with the reduction in the size of nanomaterial which leads to the band gap transition in the range of ultraviolet-visible and also effectively modifies the fluorescence quantum yield. Cdots with large conjugated sp^2 domains and a smaller number of surface chemical groups, the fluorescence depends upon the QCE of conjugated sp^2 domains.[23,24] As the size of Cdots conjugated sp^2 domain increases, the band gap decreases, and the redshift in the emission peak is occur (Figure 1.3).

Another factor responsible for the fluorescence of Cdots is surface defect states. The surface defects correspond to the boundary or surface region of the Cdots which is different from carbon core. The boundary region of Cdots consists of many functional groups with sp^2 and sp^3 hybrid carbons.

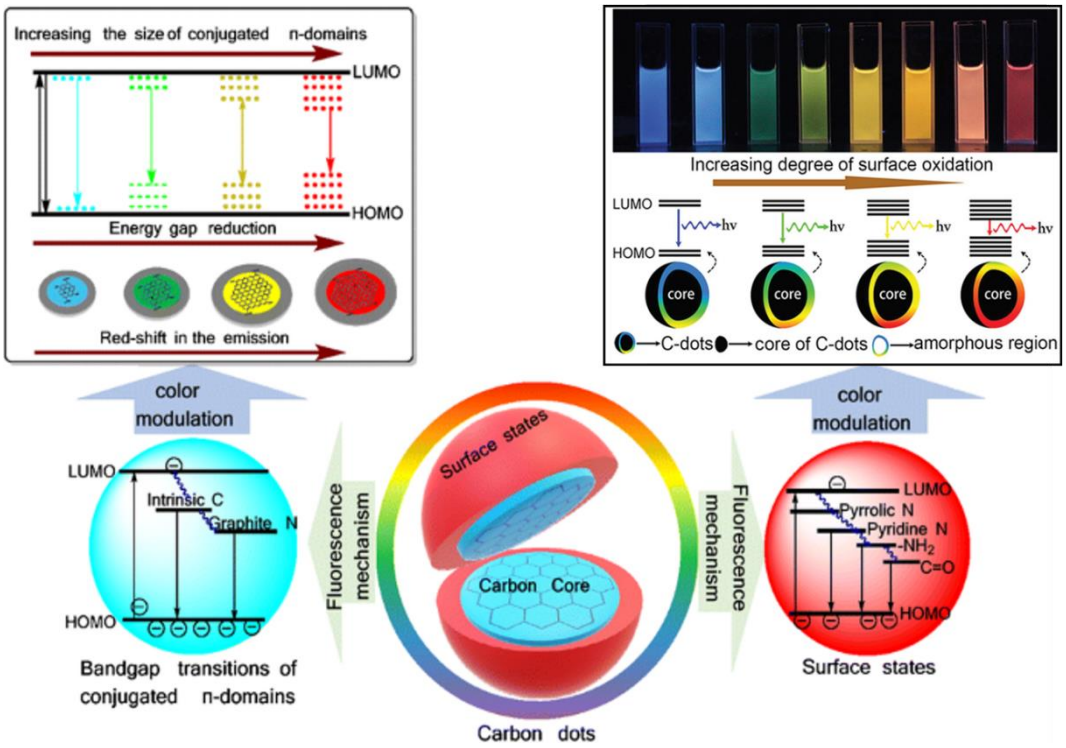

Figure 1.3. The structure of carbon dots and their fluorescence mechanisms.[22,25]

The surface defect fluorescence is based on the relaxation of radiations from ES to GS. When the radiations of a particular wavelength irradiate the Cdots, the photon with equivalent

optical band gap energy will undergo transition and get assembled in the traps of surface defects and then come back to the ground state (GS) with visible light emission. The increase in the surface oxidation of the Cdots results in a greater number of surface defects which leads to red shift in the emission peak (Figure 1.3).[25]

The molecular fluorescence mechanism is originated from the fluorescence center which consists of organic fluorophores developed through the carbonization of small molecules. Several small fluorescent molecules get attached to the surface or inside the carbon skeleton and display emissions directly.

1.1.6 Optical and photophysical properties of Cdots

The absorption and PL properties of Cdots are dependent upon the different particle sizes and distribution of surface defects.[26] Generally, carbon dots exhibit a strong absorption spectrum in the UV region and also extended in the visible range. Mostly, the prepared Cdots in the literature represent the absorbance with a range of 280-360 nm owing π-π^* as well as n-π^* transitions. The optical absorption band can be modified by surface modifications or functionalization.[27] The PL spectra provide evidence for the number of emitted photons from the excited state (ES). The excitation-dependent and excitation-independent PL behavior of Cdots are still in debate. In the excitation-independent, the sample represents the same PL emission spectra at different excitation wavelengths, whereas in the excitation-dependent, the PL emission spectra get varied with the change in the excitation wavelengths. In the literature, different mechanisms were described for both excitation-dependent and independent PL emission of Cdots. The excitation-dependent PL emission can be modified by changing its excitation wavelength only and with no requirement to control the structure of Cdots. Thus, this can be useful in various applications. The energy band gap variation because of the size distribution of Cdots, results in excitation-dependent PL emission correlated with the QCE.[28] But, excitation-independent PL emission was found in the case of large size distributions of Cdots. This proves that size is not only the factor for the excitation-dependent PL emission.[29] Among the different sizes, shapes, or surfaces of Cdots developed by different methods, some of them still have the same excitation-dependent PL properties.[30] The excitation-dependent PL properties of Cdots are due to their different sizes, surface defects, QCE, conjugated sp^2 π-domains, and zig–zag edge sites.[31] Also, the presence of many functional groups on the edges of Cdots lead to introduce many ESs which result in radiative recombination of excited electrons and further lead to PL emission at different wavelengths.[32] The surface defects are also responsible for the excitation-dependent PL emission in Cdots. But there is no united

agreement for surface state defects on the excitation-dependent PL emission due to having non-radiative traps. Generally, the fluorescence average lifetime as well as quantum yield parameters are one of the significant features of Cdots. The fluorescence properties of Cdots increases when the radiative rate constant (k_r), quantum yield (ϕ) enhances and the non-radiative rate (k_{nr}) constant decreases. The ratio of the no. of photons emitted and no. of photons absorbed is known as Quantum yield. The fluorescence quantum yield (ϕ) of Cdots was determined w.r.t. reference solution by using equation 1.1:

$$\phi_S = \phi_R \times \frac{A_S}{A_R} \times \frac{(Abs)_R}{(Abs)_S} \times \frac{\eta_S^2}{\eta_R^2} \quad (1.1)$$

Where, subscripts "S" indicates the parameters for sample and "R" for reference. "Abs" denotes absorbance while "A" and "η" are the well-known parameters represents the area under fluorescence emission and refractive index of solvent.

The average lifetime of Cdots governs the time spent in ES as well about their emission feature. The average time, a molecule spent in the ES former to come back to the GS through radiative and non-radiative deactivation pathways depicts its lifetime. The fluorescence average lifetime for the Cdots can be represented as

$$k_r = \frac{\phi_f}{\tau_f} \quad (1.2)$$

$$\frac{1}{\tau_f} = k_r + k_{nr} \quad (1.3)$$

Where, the parameters 'k_r' and 'k_{nr}', represents radiative and non-radiative rate constant while 'ϕ_f' and 'τ_f' measures fluorescence quantum yield and average lifetime value, respectively.

1.1.7 Effect of heteroatom doping on carbon dots

In recent times, PL emission efficiency can be improved or modified effectively by heteroatom doping with different elements like nitrogen, sulfur, and many others.[33] Heteroatom doping of Cdots affects the size and surface functionalization of Cdots, which put an impact on its PL properties.[34] The heteroatom doping of Cdots can be achieved by two main approaches which are one-step method and multi-step method.[35] In the one-step method, there is one pot reaction between carbon source and heteroatom source by hydrothermal method, high-temperature treatment, microwave irradiations, or chemical vapor deposition. The major requirement of one-step methods is the presence of a doping source in the starting material to obtain doped Cdots. While, the multi-step method includes the synthesis of Cdots from a

carbon source as a first step and further, the second step includes the doping of heteroatoms by specific chemical and physical methods. The doping of heteroatom in the structure of Cdots modulates their electrical properties by decreasing band gap and enhancing optical absorption.[36] Therefore, it desires to study the emissive states present in doped Cdots and the role of doped heteroatoms in the emissive mechanism.[37] Many researchers have significantly varied the electronic structure and optical properties of Cdots by mono-doping or co-doping non-metallic elements.[38] Co-doped Cdots with heteroatoms like N, B, S, and P improve the quantum yield of undoped or mono-doped Cdots by generating additional coordination sites and providing more defects in the structure of prepared Cdots.[39] It was reported that heteroatom doped GQDs with large size atoms like N, S, or small size atoms like P, B as compared to C showed exceptional properties.[40] Co-doped Cdots have extraordinary electronic structures due to the synergistic effect among the different heteroatoms.[41] The modification in the PL properties of Cdots by heteroatom doping leads to enhancing its application in the field of sensing.

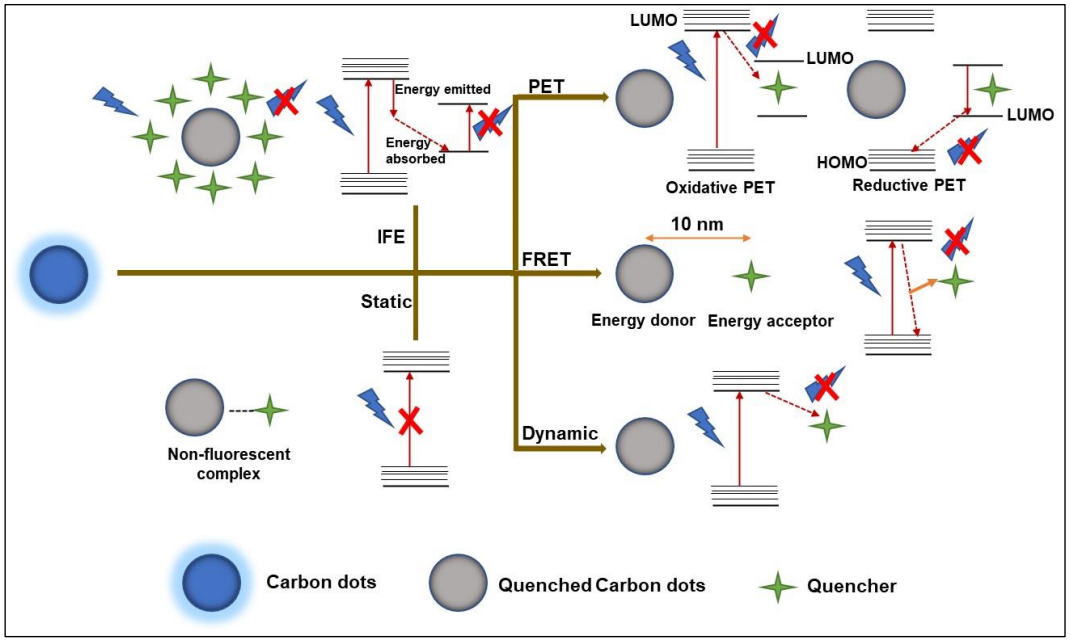

Figure 1.4: Different fluorescence quenching mechanisms of Cdots.

1.1.8 Fluorescence quenching mechanisms of Cdots

The sensing application of Cdots is based on the interactions between the Cdots and different analytes in which PL intensity gets quenched or enhanced by suppressing the effect of quenching.[42] There are different fluorescence quenching mechanisms of Cdots such as static or dynamic quenching, inner filter effect (IFE), fluorescence resonance energy transfer

(FRET), and photoinduced electron transfer (PET) (Figure 1.4).[43] The static and dynamic fluorescence quenching mechanisms are based on complexation and collisional deactivation, respectively.[44] The static quenching occurs when the interaction between Cdots and quencher results in the formation of the non-fluorescent complex. When the light gets absorbed by a non-fluorescent complex then it instantly comes back to the GS with no photon emission.[45] In the case of the static quenching, the ratio of PL lifetime of the ES to the GS is equal to unity ($\tau_0/\tau = 1$) and also the GS complex formation leads to varying the absorption spectra of Cdots.

In dynamic quenching, the Cdots come back to GS from ES due to the collision of the quencher and Cdots in which transfer of energy occurs. The average lifetime decay of the Cdots gets varied with and without the addition of a quencher. In dynamic quenching, the ES of Cdots is affected by the addition of a quencher while there is no significant variation in the UV-vis absorption spectrum of Cdots. To further confirm the static or dynamic quenching the Stern-Volmer equation is used.[34]

$$\frac{F_0}{F} = 1 + K_{SV}[Q] \tag{1.4}$$

where, the PL intensity of Cdots without and with the addition of quencher are corresponding to F_0 and F. K_{SV} signifies the Stern-Volmer quenching constant while [Q] stands for concentration of quencher. In case of dynamic quenching, K_{SV} is equal to $K_q\tau_0$, where τ_0 represents the lifetime of emissive ESs of Cdots and K_q signifies the biomolecular quenching rate constant.[71] Furthermore, to understand the stoichiometry and the interaction strength between the Cdots with quencher, the binding constant values were evaluated based on the changes in the fluorescence intensity using the 1:1 linear Benesi−Hildebrand method according to the following equation:[46]

$$\frac{1}{F_0 - F} = \frac{1}{F_0 - F_1} + \frac{1}{K[Q](F_0 - F)} \tag{1.5}$$

where, F_0 and F are the PL intensities without and with the addition of quencher. F_1 denotes the PL intensity for the 1:1 stoichiometric Cdots-quencher. The parameter K represents the binding constant values for Cdots and quencher. In case of energy transfer, k_{ET} signifies the rate of electron transfer which has been estimated using the following equation:

$$k_{ET} = \frac{1}{\tau_{DA}} - \frac{1}{\tau_D} \tag{1.6}$$

where τ_{DA} and τ_D represent the average lifetime values of Cdots with the addition and without addition of quencher.

The efficiency of the electron transfer (ϕ_{EET}) is determined using the following equations:

$$\phi_{EET} = 1 - \frac{\phi_{DA}}{\phi_D} = 1 - \frac{\tau_{DA}}{\tau_D} \quad (1.7)$$

where the parameters ϕ_{DA} and ϕ_D are the quantum yields of the Cdots in the presence and absence of quencher.

PET is a deactivation process in which electron transfer occurs between the Cdots and quencher with the formation of cation and anion radicals, respectively.[18] In the case of PET, the Cdots can behave as electron donor or electron acceptor and similarly, the quencher can also act as electron acceptor or electron donor. An internal redox reaction occurs between the ES of Cdots and quencher which can act as electron donor or electron acceptor. In this quenching mechanism, the complex of electron donor and acceptor come back to the GS with no photon emission.

FRET is an electrodynamics phenomenon based on long-range dipole-dipole interactions among the Cdots and quencher.[43] It happens only if the emission spectrum of Cdots (donor) present in ES merges with the absorption spectra of Q (acceptor) present in the GS. The separation in the donor and acceptor should lies between 1-10 nm for the occurrence of the FRET mechanism. In the FRET mechanism, the average lifetime reduces with enhancing the concentration of quencher.[47] The spectral overlap integral [J(λ)] of Cdots-quencher was calculated using the following equation:

$$J(\lambda) = \frac{\int_0^\infty F_D(\lambda)\varepsilon_A(\lambda)\lambda^4 D\lambda}{\int_0^\infty F_D(\lambda)d\lambda} \quad (1.8)$$

The parameter $F_D(\lambda)$ represents the normalized PL intensity of donor (only Cdots) in the wavelength range $\lambda + d\lambda$, and $\varepsilon_A(\lambda)$ denotes the molar extinction coefficient of the acceptor (quencher). Further, the FRET efficiency (E) of the Cdots in the presence of quencher has been estimated using the following equation:[45]

$$E = \frac{k_{ET}}{k_r + k_{ET} + k_{nr}} \quad (1.9)$$

where, k_{ET} corresponds to rate of electron transfer, k_r corresponds to radiative constant and k_{nr} corresponds to nonradiative rate constant. Moreover, we have also estimated the Förster distance (R_0) for Cdots and quencher by using the following formula:[45]

$$R_0 = 0.211[\kappa^2\eta^{-4}\Phi_D J(\lambda)]^{1/6} \quad (1.10)$$

R_0 represents the distance from the center of donor (Cdots) to acceptor (quencher), where the energy transfer efficiency becomes 50%. κ^2 denotes the relative orientation factor of the transition dipoles of the donor and the acceptor in isotropic solution, η demonstrate the viscosity of medium, and ϕ_D and J(λ) are the fluorescence quantum yield of the donor and the spectral overlap integral, respectively. Moreover, the separable distance (r) among Cdots and quencher can be evaluated from the respective FRET efficiency values by using the following formula:[45]

$$E = \frac{1}{1+(\frac{r}{R_0})^6} \tag{1.11}$$

IFE arises if absorption spectra correspond to quencher inhibits all transition by Cdots. As a result, the spectral overlapping has been observed across the absorption spectra of the quencher and transition states of Cdots. Mostly, IFE-based sensing platform does not involve covalent bonding or intermolecular interactions among the fluorescent material and quencher.[48] The separation among fluorescent material and quencher must be greater than 10 nm. Significantly, the IFE cannot relate to static or dynamic quenching due to the same response governed by absorption spectrum of Cdots in the variable concentration of quencher, result in lack of formation of new material.

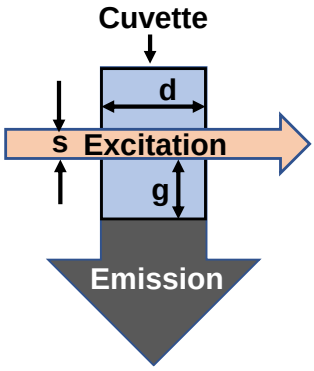

Figure 1.5. The parameters used in Parker equation.

Furthermore, to clarify the IFE process the following Parker equation (1.12) can be used.[43]

$$\frac{F_{cor}}{F_{obsd}} = \frac{2.3dA_{ex}}{1-10^{-dA_{ex}}}\ 10^{gA_{em}}\ \frac{2.3sA_{em}}{1-10^{-sA_{em}}} \tag{1.12}$$

where "F_{obsd}" and "F_{cor}" refer to observed PL intensity and corrected PL intensity after eradicating IFE from "F_{obsd}". "A_{ex}" and "A_{em}" denotes the absorbance values at maximum

excitation and emission wavelength, respectively. “s” corresponds to the width of the excitation beam (Figure 1.5). The distance from the excitation beam’s edge to the edge of the cuvette is signified as ‘g’ and the width of the cuvette is denoted as ‘d’ (Figure 1.5).

1.1.9 Strategy for detection of biomolecules using Cdots

There are major two types of strategies for detection of biomolecules including the “turn-off” and “turn-off-on” strategies. In the “turn-off-on” strategy, the quencher firstly deteriorates fluorescence properties of Cdots and then, these are recovered by the addition of target analyte. It was found that the “turn-off-on” strategy is much more selective and sensitive in comparison to the “turn-off” strategy because there are more chances for the interference of other analytes with target molecules in the case of “turn-off” strategy as compared to the “turn-off-on” strategy. Therefore, we choose “turn-off-on” strategy for the detection of biomolecules using various quenchers.

1.1.10 Detection of biomolecules

There are various biomolecules such as GSH, uric acid (UA), dopamine (DA), AA, glucose, Cys, choline, etc., which help in maintaining the metabolism of the human body.[49] For example, glutathione (GSH), the major nonprotein thiol, is present in mammalian and eukaryotic cells and regarded as a tripeptide, which is composed of three amino acids, i.e., glycine, L-cysteine, and L-glutamic acid.[50] Among all small intracellular molecular thiols, GSH assists in many cellular functions such as protection of intracellular redox reactions, xenobiotic metabolism, intracellular signal transduction, gene regulation, damage of liver, etc.[51,52] Similarly, ascorbic acid (AA, also called vitamin C) acts as an antioxidant and also plays a great role in different biochemical processes in living organisms and its quantitative detection is very helpful in pharmaceutical analysis.[53,54] But, the imbalance in the amount of these biomolecules in the human body creates many diseases such as AIDS, mental disorders, cancer, Parkinson’s, and many others. Therefore, sensing of biomolecules plays an important role across wide range applications likely medical analysis, drug delivery, environmental science, as well in the food industry which leads to raising the demand for developing easy, highly sensitive, extremely selective, and economical biosensors.[55] Nowadays, there are many techniques for the detection of various biomolecules such as surface-enhanced Raman spectroscopy (SERS),[56,57] the colorimetric method,[58–60] electrochemical method,[61] surface plasmon resonance,[62,63] high-performance liquid chromatography, etc. However, these techniques have many limitations such as expensive equipment, less sensitivity, time-consuming, and difficult handling, which decrease their use in the repetitive detection of biomolecules. Fluorescence spectroscopy is a dominant optical technique and is a non-

destructive, highly sensitive, and simple detection technique.[64,65] The metal-carbon nanocomposite are highly used for the sensing application.[66] Biomolecules have great affinity for metal surfaces.[67] So, the combinations of Cdots and metal oxide-based quenchers used as promising sensor for the detection of biomolecules. There are various sensing probes reported in the literatures for the detection of biomolecules (Table 1.1).

Table 1.1: Detection of several biomolecules based on different sensing probes with specific sensing methods.

Sr. no.	Sensing Probe	Sensing Method	Bio-molecule	Detection Range	LOD	Ref.
1.	MnO_2NSPs@ GNR composites	Electrochemical	Glucose	0.1-1.4 mM	50 μM	[68]
2.	MnO_2 NWs-ErGO/GCE	Electrochemical	DA	0.01-80 μM	1.0 nM	[69]
3.	BSA-templated MnO_2NPs	Chemilumine-scence	Glucose	50 μM-15.8 mM	44.7 μM	[70]
4.	Ag_2SQD/MnO_2 nanosheet	Fluorescence	GSH	0.3-1.2 mM	60 μM	[71]
5.	CoOOH nanosheets	Colorimetric	GSH	33 μM- 1.3 mM	13.7 μM	[72]
6.	N-GQDs-V_2O_5 nanosheet	Fluorescence	Cys	0.1-15 μM	50 nM	[73]
7.	AuNCs@BSA-MnO_2NSs	Fluorescence	GSH	0-0.5 mM	20 μM	[74]
8.	Carbon dot-KI_3	Fluorescence	L-Tyrosine	0.931-5.35 μM	2.614 μM	[75]
9.	N-rGO-$Co(OH)_2$	Electrochemical	DA UA	50 μM-15.8mM	10 nM 100 nM	[76]
10.	MnO_2NFs/N-rGO	Electrochemical	DA UA	6-100 μM	0.036 μM 0.029 μM	[77]
11.	AgNPs-BSA-MnO_2 NSs/GCE	Electrochemi-luminescence	Cholesterol	0.21-1667 μM	0.07 μM	[78]
12.	MnO_2 NSs@ Biotin-QDs	Fluorescence	GSH	0.05-1.5 mM	16.3μM	[79]
13.	Naphthalene derivate containing piazselenole (NDP)	Colorimetric	GSH	0-80 mM	0.178 mM	[80]
14.	Cobalt phthalocyanine (CoPc) and multiwalled carbon nanotubes	Differential pulse voltammetry	GSH	0.5-7 mM	100 μM	[81]

	functionalized with carboxyl groups ($MWCNT_f$)					
15.	Disposable paper-based printed electroanalytical strip	Cyclic voltammetry	GSH	0-10 mM	60 μM	[82]
16.	Carbon dots@MnO_2 NSs	Fluorescence	AA	0−80 μM	2.89 μM	[83]

1.1.11 Manganese Oxide (MnO_2) nanomaterial as a quencher

Among various transition metal oxides, MnO_2 has been broadly considered an active material for the detection of biomolecules because of its unique physical, optical, and electrochemical properties. MnO_2 has obtained a great interest in various research fields due to its unique electrochemical properties, high charge transfer rate, large active surface area, non-toxic nature, and inexpensive cost.[84] Moreover, various applications of MnO_2 nanostructures are due to their structural versatility, different oxidation states such as +2, +3, or +4 of Mn present in these nanostructures, and their simultaneous existence of distinct valance states across same crystallite.[85,86] MnO_2 nanostructures are extensively used as highly capable biosensors and photochemical and supercapacitor materials in biofuel-based biosensors and semiconductors.[87,88] MnO_2 nanoparticles of large surface area have great ability to absorb light due to which it can be used as an effective fluorescent quencher, which further got tremendous attraction in the rise of "turn off−on" fluorescence sensing platforms.[89] MnO_2 or MnO_2-based nanomaterials with different morphology have variations in their properties. Therefore, they were considered for a highly sensitive sensing platform to detect different biomolecules.

Shape control is one of the most significant techniques for enhancing the quality as well as the catalytic activity of nanomaterials. The different shapes of MnO_2 include NR, NT, NW, NS, NF, Nanosheets, and various other shapes can be synthesized, and also their properties are changed with the variation in shape or morphology.[90,91] Figure 1.6 represents various morphologies of MnO_2 with four dimensions including all 0-D to 3-D. Various methods for the preparation of different morphologies of MnO_2 have been reported which include lithography, the electron beam method, templates, the precipitation method, the sol−gel method, electrospinning, as well as the electrodeposition method.[92] All these methods were reported as most acceptable due to their simplicity, biocompatibility, economical, and versatility points of

view. The variations in crystal parameters, phase structure, and surface morphology of MnO_2 showed high catalytic activity and oxidative reactivity.[87] The activity of the nanomaterials is dependent upon the structure of the surface and active sites present on it.

Moreover, various reductive biomolecules can be oxidized by MnO_2 nanostructure due to its oxidizing property that will confine the selectivity of sensing platforms.[93] Hence, the synthesis of a self-fluorescent MnO_2 nanomaterial with particular functional groups is also great filed of research. The morphology or shape associated with the crystal phase of the MnO_2 nanostructure may have an impact on its sensing activity, and therefore, examining the relationship between the morphologies of MnO_2 materials and their sensing activities under the same crystalline phase has become a great field of interest.

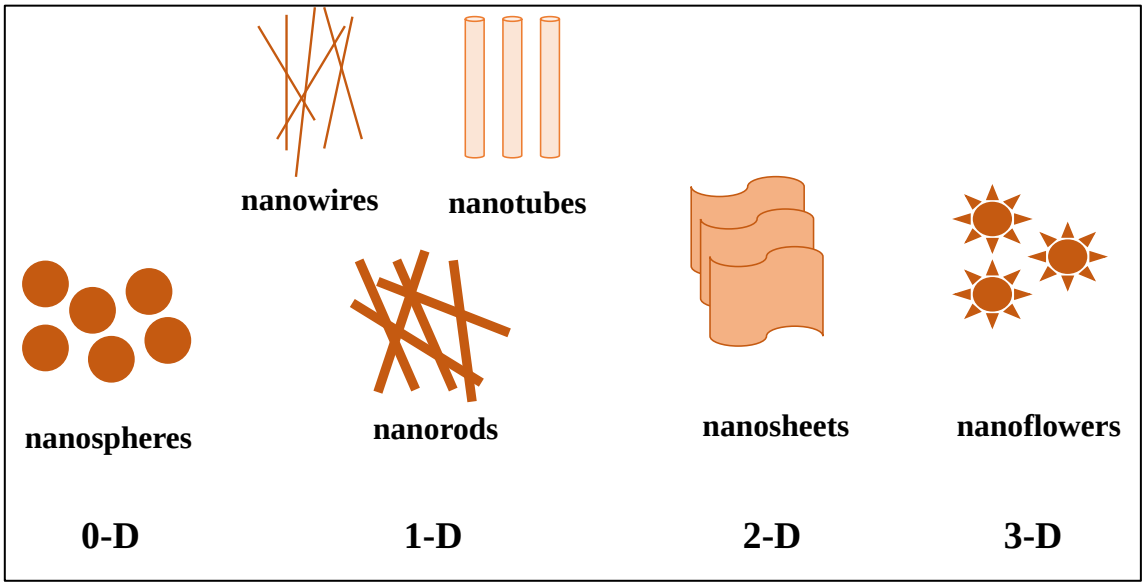

Figure 1.6. Different morphologies or shapes of MnO_2 nanostructure with four different dimensions (0-D, 1-D, 2-D, and 3-D).[4]

1.2 Lacunae and possibilities

Based on the literature review some research gaps are outlined and given below:

- There are only a few studies found on the study of all photophysical parameters of Cdots.
- The impact of variation in shape/size of MnO_2 nanostructure on all photophysical parameters of Cdots has not been explored.
- Mostly MnO_2 nanosheets were used as quencher with Cdots for the detection of biomolecules.

- Few studies were done related to the selectivity and sensitivity of different shapes and sizes of MnO_2 nanostructure by fluorescence spectroscopy for the detection of biomolecules.

1.3 Objectives

The main purpose of this work is to prepare different shapes/sizes of MnO_2 for the sensitive and selective detection of biomolecules. The specific objectives are as follows:

- Synthesis of fluorescent carbon dots (Cdots) and MnO_2 nanostructures with varying size and shape.
- Studying the different photophysical parameters of Cdots-MnO_2 composites.
- Optimization the limit of detection of biomolecules by Cdots-MnO_2 composite nanosensors.

References

(1) Mousavi, S. M.; Hashemi, S. A.; Zarei, M.; Amani, A. M.; Babapoor, A. Nanosensors for Chemical and Biological and Medical Applications. *Med. Chem. (Los. Angeles).* **2018**, *08* (08). https://doi.org/10.4172/2161-0444.1000515.

(2) Meng, Z.; Stolz, R. M.; Mendecki, L.; Mirica, K. A. Electrically-Transduced Chemical Sensors Based on Two-Dimensional Nanomaterials. *Chem. Rev.* **2019**, *119* (1), 478–598. https://doi.org/10.1021/acs.chemrev.8b00311.

(3) Munawar, A.; Ong, Y.; Schirhagl, R.; Tahir, M. A.; Khan, W. S.; Bajwa, S. Z. Nanosensors for Diagnosis with Optical, Electric and Mechanical Transducers. *RSC Adv.* **2019**, *9* (12), 6793–6803. https://doi.org/10.1039/C8RA10144B.

(4) Sohal, N.; Maity, B.; Shetti, N. P.; Basu, S. Biosensors Based on MnO 2 Nanostructures: A Review. *ACS Appl. Nano Mater.* **2021**, *4* (3), 2285–2302. https://doi.org/10.1021/acsanm.0c03380.

(5) Adam, T.; Dhahi, T. S. Nanosensors: Recent Perspectives on Attainments and Future Promise of Downstream Applications. *Process Biochem.* **2022**, *117*, 153–173. https://doi.org/10.1016/j.procbio.2022.03.024.

(6) Javaid, M.; Haleem, A.; Singh, R. P.; Rab, S.; Suman, R. Exploring the Potential of Nanosensors: A Brief Overview. *Sensors Int.* **2021**, *2*, 100130. https://doi.org/10.1016/j.sintl.2021.100130.

(7) Srivastava, A. K.; Dev, A.; Karmakar, S. Nanosensors and Nanobiosensors in Food and Agriculture. *Environ. Chem. Lett.* **2018**, *16* (1), 161–182. https://doi.org/10.1007/s10311-017-0674-7.

(8) Ahmad, F.; Salem-Bekhit, M. M.; Khan, F.; Alshehri, S.; Khan, A.; Ghoneim, M. M.; Wu, H.-F.; Taha, E. I.; Elbagory, I. Unique Properties of Surface-Functionalized Nanoparticles for Bio-Application: Functionalization Mechanisms and Importance in Application. *Nanomaterials* **2022**, *12* (8), 1333. https://doi.org/10.3390/nano12081333.

(9) Hao, L.; Xue, L.; Huang, F.; Cai, G.; Qi, W.; Zhang, M.; Han, Q.; Wang, Z.; Lin, J. A Microfluidic Biosensor Based on Magnetic Nanoparticle Separation, Quantum Dots Labeling and MnO_2 Nanoflower Amplification for Rapid and Sensitive Detection of Salmonella Typhimurium. *Micromachines* **2020**, *11* (3), 281. https://doi.org/10.3390/mi11030281.

(10) Umapathi, R.; Park, B.; Sonwal, S.; Rani, G. M.; Cho, Y.; Huh, Y. S. Advances in Optical-Sensing Strategies for the on-Site Detection of Pesticides in Agricultural Foods. *Trends Food Sci. Technol.* **2022**, *119*, 69–89. https://doi.org/10.1016/j.tifs.2021.11.018.

(11) Lee, M. H.; Kim, J. S.; Sessler, J. L. Small Molecule-Based Ratiometric Fluorescence Probes for Cations, Anions, and Biomolecules. *Chem. Soc. Rev.* **2015**, *44* (13), 4185–4191. https://doi.org/10.1039/C4CS00280F.

(12) Gao, M.; Tang, B. Z. Fluorescent Sensors Based on Aggregation-Induced Emission: Recent Advances and Perspectives. *ACS Sensors* **2017**, *2* (10), 1382–1399. https://doi.org/10.1021/acssensors.7b00551.

(13) Yoo, D.; Park, Y.; Cheon, B.; Park, M.-H. Carbon Dots as an Effective Fluorescent Sensing Platform for Metal Ion Detection. *Nanoscale Res. Lett.* **2019**, *14* (1), 272. https://doi.org/10.1186/s11671-019-3088-6.

(14) Sakdaronnarong, C.; Sangjan, A.; Boonsith, S.; Kim, D. C.; Shin, H. S. Recent Developments in Synthesis and Photocatalytic Applications of Carbon Dots. *Catalysts* **2020**, *10* (3), 320. https://doi.org/10.3390/catal10030320.

(15) Espina-Casado, J.; Fontanil, T.; Fernández-González, A.; Cal, S.; Obaya, Á. J.; Díaz-García, M. E.; Badía-Laíño, R. Carbon Dots as Multifunctional Platform for Intracellular PH Sensing and Bioimaging. In Vitro and in Vivo Studies. *Sensors Actuators B Chem.*

2021, *346*, 130555. https://doi.org/10.1016/j.snb.2021.130555.

(16) Li, M.; Chen, T.; Gooding, J. J.; Liu, J. Review of Carbon and Graphene Quantum Dots for Sensing. *ACS Sensors* **2019**, *4* (7), 1732–1748. https://doi.org/10.1021/acssensors.9b00514.

(17) Namdari, P.; Negahdari, B.; Eatemadi, A. Synthesis, Properties and Biomedical Applications of Carbon-Based Quantum Dots: An Updated Review. *Biomed. Pharmacother.* **2017**, *87*, 209–222. https://doi.org/10.1016/j.biopha.2016.12.108.

(18) Sun, X.; Lei, Y. Fluorescent Carbon Dots and Their Sensing Applications. *TrAC Trends Anal. Chem.* **2017**, *89*, 163–180. https://doi.org/10.1016/j.trac.2017.02.001.

(19) Li, L.; Dong, T. Photoluminescence Tuning in Carbon Dots: Surface Passivation or/and Functionalization, Heteroatom Doping. *J. Mater. Chem. C* **2018**, *6* (30), 7944–7970. https://doi.org/10.1039/C7TC05878K.

(20) Wu, Z. L.; Liu, Z. X.; Yuan, Y. H. Carbon Dots: Materials, Synthesis, Properties and Approaches to Long-Wavelength and Multicolor Emission. *J. Mater. Chem. B* **2017**, *5* (21), 3794–3809. https://doi.org/10.1039/C7TB00363C.

(21) Zhou, J.; Zhou, H.; Tang, J.; Deng, S.; Yan, F.; Li, W.; Qu, M. Carbon Dots Doped with Heteroatoms for Fluorescent Bioimaging: A Review. *Microchim. Acta* **2017**, *184* (2), 343–368. https://doi.org/10.1007/s00604-016-2043-9.

(22) Yan, F.; Sun, Z.; Zhang, H.; Sun, X.; Jiang, Y.; Bai, Z. The Fluorescence Mechanism of Carbon Dots, and Methods for Tuning Their Emission Color: A Review. *Microchim. Acta* **2019**, *186* (8), 583. https://doi.org/10.1007/s00604-019-3688-y.

(23) Sk, M. A.; Ananthanarayanan, A.; Huang, L.; Lim, K. H.; Chen, P. Revealing the Tunable Photoluminescence Properties of Graphene Quantum Dots. *J. Mater. Chem. C* **2014**, *2* (34), 6954–6960. https://doi.org/10.1039/C4TC01191K.

(24) Kwon, W.; Lee, G.; Do, S.; Joo, T.; Rhee, S.-W. Size-Controlled Soft-Template Synthesis of Carbon Nanodots toward Versatile Photoactive Materials. *Small* **2014**, *10* (3), 506–513. https://doi.org/10.1002/smll.201301770.

(25) Liu, M. L.; Chen, B. Bin; Li, C. M.; Huang, C. Z. Carbon Dots: Synthesis, Formation Mechanism, Fluorescence Origin and Sensing Applications. *Green Chem.* **2019**, *21* (3), 449–471. https://doi.org/10.1039/C8GC02736F.

(26) Dhenadhayalan, N.; Lin, K.-C.; Suresh, R.; Ramamurthy, P. Unravelling the Multiple Emissive States in Citric-Acid-Derived Carbon Dots. *J. Phys. Chem. C* **2016**, *120* (2), 1252–1261. https://doi.org/10.1021/acs.jpcc.5b08516.

(27) Wang, J.; Qiu, J. A Review of Carbon Dots in Biological Applications. *J. Mater. Sci.* **2016**, *51* (10), 4728–4738. https://doi.org/10.1007/s10853-016-9797-7.

(28) Barman, M. K.; Patra, A. Current Status and Prospects on Chemical Structure Driven Photoluminescence Behaviour of Carbon Dots. *J. Photochem. Photobiol. C Photochem. Rev.* **2018**, *37*, 1–22. https://doi.org/10.1016/j.jphotochemrev.2018.08.001.

(29) Maiti, S.; Kundu, S.; Roy, C. N.; Das, T. K.; Saha, A. Synthesis of Excitation Independent Highly Luminescent Graphene Quantum Dots through Perchloric Acid Oxidation. *Langmuir* **2017**, *33* (51), 14634–14642. https://doi.org/10.1021/acs.langmuir.7b02611.

(30) Gan, Z.; Xu, H.; Hao, Y. Mechanism for Excitation-Dependent Photoluminescence from Graphene Quantum Dots and Other Graphene Oxide Derivates: Consensus, Debates and Challenges. *Nanoscale* **2016**, *8* (15), 7794–7807. https://doi.org/10.1039/c6nr00605a.

(31) Langer, M.; Paloncýová, M.; Medveď, M.; Pykal, M.; Nachtigallová, D.; Shi, B.; Aquino, A. J. A.; Lischka, H.; Otyepka, M. Progress and Challenges in Understanding of Photoluminescence Properties of Carbon Dots Based on Theoretical Computations. *Appl. Mater. Today* **2021**, *22*, 100924. https://doi.org/10.1016/j.apmt.2020.100924.

(32) Hu, S. Tuning Optical Properties and Photocatalytic Activities of Carbon-Based "Quantum Dots" Through Their Surface Groups. *Chem. Rec.* **2016**, *16* (1), 219–230. https://doi.org/10.1111/tcr.201500225.

(33) Li, F.; Yang, D.; Xu, H. Non-Metal-Heteroatom-Doped Carbon Dots: Synthesis and Properties. *Chem. - A Eur. J.* **2019**, *25* (5), 1165–1176. https://doi.org/10.1002/chem.201802793.

(34) Xu, Q.; Kuang, T.; Liu, Y.; Cai, L.; Peng, X.; Sreenivasan Sreeprasad, T.; Zhao, P.; Yu, Z.; Li, N. Heteroatom-Doped Carbon Dots: Synthesis, Characterization, Properties, Photoluminescence Mechanism and Biological Applications. *J. Mater. Chem. B* **2016**, *4* (45), 7204–7219. https://doi.org/10.1039/C6TB02131J.

(35) Miao, S.; Liang, K.; Zhu, J.; Yang, B.; Zhao, D.; Kong, B. Hetero-Atom-Doped Carbon

Dots: Doping Strategies, Properties and Applications. *Nano Today* **2020**, *33*, 100879. https://doi.org/10.1016/j.nantod.2020.100879.

(36) Xu, H.; Zhou, S.; Xiao, L.; Yuan, Q.; Gan, W. Time-Efficient Syntheses of Nitrogen and Sulfur Co-Doped Graphene Quantum Dots with Tunable Luminescence and Their Sensing Applications. *RSC Adv.* **2016**, *6* (43), 36554–36560. https://doi.org/10.1039/c6ra05175h.

(37) Yang, G.; Wu, C.; Luo, X.; Liu, X.; Gao, Y.; Wu, P.; Cai, C.; Saavedra, S. S. Exploring the Emissive States of Heteroatom-Doped Graphene Quantum Dots. *J. Phys. Chem. C* **2018**, *122* (11), 6483–6492. https://doi.org/10.1021/acs.jpcc.8b01385.

(38) Liu, Z.; Mo, Z.; Liu, N.; Guo, R.; Niu, X.; Zhao, P.; Yang, X. One-Pot Synthesis of Highly Fluorescent Boron and Nitrogen Co-Doped Graphene Quantum Dots for the Highly Sensitive and Selective Detection of Mercury Ions in Aqueous Media. *J. Photochem. Photobiol. A Chem.* **2020**, *389*, 112255. https://doi.org/10.1016/j.jphotochem.2019.112255.

(39) Xu, Y.; Wang, S.; Hou, X.; Sun, Z.; Jiang, Y.; Dong, Z.; Tao, Q.; Man, J.; Cao, Y. Coal-Derived Nitrogen, Phosphorus and Sulfur Co-Doped Graphene Quantum Dots: A Promising Ion Fluorescent Probe. *Appl. Surf. Sci.* **2018**, *445*, 519–526. https://doi.org/10.1016/j.apsusc.2018.03.156.

(40) Qu, D.; Sun, Z.; Zheng, M.; Li, J.; Zhang, Y.; Zhang, G.; Zhao, H.; Liu, X.; Xie, Z. Three Colors Emission from S,N Co-Doped Graphene Quantum Dots for Visible Light H2 Production and Bioimaging. *Adv. Opt. Mater.* **2015**, *3* (3), 360–367. https://doi.org/10.1002/adom.201400549.

(41) Xu, Q.; Liu, Y.; Gao, C.; Wei, J.; Zhou, H.; Chen, Y.; Dong, C.; Sreeprasad, T. S.; Li, N.; Xia, Z. Synthesis, Mechanistic Investigation, and Application of Photoluminescent Sulfur and Nitrogen Co-Doped Carbon Dots. *J. Mater. Chem. C* **2015**, *3* (38), 9885–9893. https://doi.org/10.1039/C5TC01912E.

(42) Zuo, P.; Lu, X.; Sun, Z.; Guo, Y.; He, H. A Review on Syntheses, Properties, Characterization and Bioanalytical Applications of Fluorescent Carbon Dots. *Microchim. Acta* **2016**, *183* (2), 519–542. https://doi.org/10.1007/s00604-015-1705-3.

(43) Zu, F.; Yan, F.; Bai, Z.; Xu, J.; Wang, Y.; Huang, Y.; Zhou, X. The Quenching of the

Fluorescence of Carbon Dots: A Review on Mechanisms and Applications. *Microchim. Acta* **2017**, *184* (7), 1899–1914. https://doi.org/10.1007/s00604-017-2318-9.

(44) Anusuya, T.; Kumar, V.; Kumar, V. Hydrophilic Graphene Quantum Dots as Turn-off Fluorescent Nanoprobes for Toxic Heavy Metal Ions Detection in Aqueous Media. *Chemosphere* **2021**, *282*, 131019. https://doi.org/10.1016/j.chemosphere.2021.131019.

(45) Lakowicz, J. R. *Principles of Fluorescence Spectroscopy*; Lakowicz, J. R., Ed.; Springer US: Boston, MA, 2006. https://doi.org/10.1007/978-0-387-46312-4.

(46) Hildebrand, J. H.; Benesi, H. A. Interaction of Iodine with Aromatic Hydrocarbons. *Nature* **1949**, *164* (4179), 963–963. https://doi.org/10.1038/164963b0.

(47) Sun, X.; Lei, Y. Fluorescent Carbon Dots and Their Sensing Applications. *TrAC Trends Anal. Chem.* **2017**, *89*, 163–180. https://doi.org/10.1016/j.trac.2017.02.001.

(48) Yang, B.; Li, X.; Wang, L.; An, J.; Wang, T.; Zhang, F.; Ding, B.; Li, Y. A Water-Stable MOF-$AgClO_4$-Abtz as Fluorescent Sensor for Detection of Folic Acid Based on Inner Filter Effect. *Talanta* **2020**, *217*, 121019. https://doi.org/10.1016/j.talanta.2020.121019.

(49) Wang, Q.; Liu, S.; Fu, L.; Cao, Z.; Ye, W.; Li, H.; Guo, P.; Zhao, X. S. Electrospun γ-Fe_2O_3 Nanofibers as Bioelectrochemical Sensors for Simultaneous Determination of Small Biomolecules. *Anal. Chim. Acta* **2018**, *1026*, 125–132. https://doi.org/10.1016/j.aca.2018.04.010.

(50) Zhang, X. L.; Zheng, C.; Guo, S. S.; Li, J.; Yang, H. H.; Chen, G. Turn-on Fluorescence Sensor for Intracellular Imaging of Glutathione Using g-C_3N_4 Nanosheet-MnO_2 Sandwich Nanocomposite. *Anal. Chem.* **2014**, *86* (7), 3426–3434. https://doi.org/10.1021/ac500336f.

(51) He, L.; Xu, Q.; Liu, Y.; Wei, H.; Tang, Y.; Lin, W. Coumarin-Based Turn-On Fluorescence Probe for Specific Detection of Glutathione over Cysteine and Homocysteine. *ACS Appl. Mater. Interfaces* **2015**, *7* (23), 12809–12813. https://doi.org/10.1021/acsami.5b01934.

(52) Le, X. A.; Le, T. N.; Kim, M. Il. Dual-Functional Peroxidase-Copper Phosphate Hybrid Nanoflowers for Sensitive Detection of Biological Thiols. *Int. J. Mol. Sci.* **2021**, *23* (1), 366. https://doi.org/10.3390/ijms23010366.

(53) Peng, J.; Ling, J.; Zhang, X.-Q.; Zhang, L.-Y.; Cao, Q.-E.; Ding, Z.-T. A Rapid,

Sensitive and Selective Colorimetric Method for Detection of Ascorbic Acid. *Sensors Actuators B Chem.* **2015**, *221*, 708–716. https://doi.org/10.1016/j.snb.2015.07.002.

(54) Meng, H.; Yang, D.; Tu, Y.; Yan, J. Turn-on Fluorescence Detection of Ascorbic Acid with Gold Nanolcusters. *Talanta* **2017**, *165*, 346–350. https://doi.org/10.1016/j.talanta.2016.12.047.

(55) Kumar, S.; Bukkitgar, S. D.; Singh, S.; Pratibha; Singh, V.; Reddy, K. R.; Shetti, N. P.; Venkata Reddy, C.; Sadhu, V.; Naveen, S. Electrochemical Sensors and Biosensors Based on Graphene Functionalized with Metal Oxide Nanostructures for Healthcare Applications. *ChemistrySelect* **2019**, *4* (18), 5322–5337. https://doi.org/10.1002/slct.201803871.

(56) Ham, J.; Yun, B. J.; Koh, W.-G. SERS-Based Biosensing Platform Using Shape-Coded Hydrogel Microparticles Incorporating Silver Nanoparticles. *Sensors Actuators B Chem.* **2021**, *341*, 129989. https://doi.org/10.1016/j.snb.2021.129989.

(57) Juang, R.-S.; Wang, K.-S.; Cheng, Y.-W.; Fu, C.-C.; Chen, W.-T.; Liu, C.-M.; Chien, C.-C.; Jeng, R.-J.; Chen, C.-C.; Liu, T.-Y. Floating SERS Substrates of Silver Nanoparticles-Graphene Based Nanosheets for Rapid Detection of Biomolecules and Clinical Uremic Toxins. *Colloids Surfaces A Physicochem. Eng. Asp.* **2019**, *576*, 36–42. https://doi.org/10.1016/j.colsurfa.2019.05.042.

(58) Li, F.; Wang, X.; Liu, J.; Hu, Y.; He, J. Double-Layered Microfluidic Paper-Based Device with Multiple Colorimetric Indicators for Multiplexed Detection of Biomolecules. *Sensors Actuators B Chem.* **2019**, *288*, 266–273. https://doi.org/10.1016/j.snb.2019.02.116.

(59) Zhang, Y.; Song, J.; Pan, Q.; Zhang, X.; Shao, W.; Zhang, X.; Quan, C.; Li, J. An Au@NH_2-MIL-125(Ti)-Based Multifunctional Platform for Colorimetric Detections of Biomolecules and Hg^{2+}. *J. Mater. Chem. B* **2020**, *8* (1), 114–124. https://doi.org/10.1039/C9TB02183C.

(60) Sena-Torralba, A.; Torné-Morató, H.; Parolo, C.; Ranjbar, S.; Farahmand Nejad, M. A.; Álvarez-Diduk, R.; Idili, A.; Hormozi-Nezhad, M. R.; Merkoçi, A. A Novel Ratiometric Fluorescent Approach for the Modulation of the Dynamic Range of Lateral Flow Immunoassays. *Adv. Mater. Technol.* **2022**, 2101450. https://doi.org/10.1002/admt.202101450.

(61) Bukkitgar, S. D.; Shetti, N. P.; Kulkarni, R. M.; Halbhavi, S. B.; Wasim, M.; Mylar, M.; Durgi, P. S.; Chirmure, S. S. Electrochemical Oxidation of Nimesulide in Aqueous Acid Solutions Based on TiO_2 Nanostructure Modified Electrode as a Sensor. *J. Electroanal. Chem.* **2016**, *778*, 103–109. https://doi.org/10.1016/j.jelechem.2016.08.024.

(62) Gómez-de Pedro, S.; Lopes, D.; Miltsov, S.; Izquierdo, D.; Alonso-Chamarro, J.; Puyol, M. Optical Microfluidic System Based on Ionophore Modified Gold Nanoparticles for the Continuous Monitoring of Mercuric Ion. *Sensors Actuators B Chem.* **2014**, *194*, 19–26. https://doi.org/10.1016/j.snb.2013.12.076.

(63) S. S. dos Santos, P.; M. M. M. de Almeida, J.; Pastoriza-Santos, I.; C. C. Coelho, L. Advances in Plasmonic Sensing at the NIR—A Review. *Sensors* **2021**, *21* (6), 2111. https://doi.org/10.3390/s21062111.

(64) Krishna Kumar, A. S.; Lu, C.-Y.; Tseng, W.-L. Two in One: Poly(Ethyleneimine)-Modified MnO_2 Nanosheets for Ultrasensitive Detection and Catalytic Reduction of 2,4,6-Trinitrotoluene and Other Nitro Aromatics. *ACS Sustain. Chem. Eng.* **2021**, *9* (3), 1142–1151. https://doi.org/10.1021/acssuschemeng.0c06224.

(65) Ponlakhet, K.; Phooplub, K.; Phongsanam, N.; Phongsraphang, T.; Phetduang, S.; Surawanitkun, C.; Buranachai, C.; Loilome, W.; Ngeontae, W. Smartphone-Based Portable Fluorescence Sensor with Gold Nanoparticle Mediation for Selective Detection of Nitrite Ions. *Food Chem.* **2022**, *384*, 132478. https://doi.org/10.1016/j.foodchem.2022.132478.

(66) Qian, L.; Durairaj, S.; Prins, S.; Chen, A. Nanomaterial-Based Electrochemical Sensors and Biosensors for the Detection of Pharmaceutical Compounds. *Biosens. Bioelectron.* **2021**, *175*, 112836. https://doi.org/10.1016/j.bios.2020.112836.

(67) Limo, M. J.; Sola-Rabada, A.; Boix, E.; Thota, V.; Westcott, Z. C.; Puddu, V.; Perry, C. C. Interactions between Metal Oxides and Biomolecules: From Fundamental Understanding to Applications. *Chem. Rev.* **2018**, *118* (22), 11118–11193. https://doi.org/10.1021/acs.chemrev.7b00660.

(68) Vukojević, V.; Djurdjić, S.; Ognjanović, M.; Fabián, M.; Samphao, A.; Kalcher, K.; Stanković, D. M. Enzymatic Glucose Biosensor Based on Manganese Dioxide Nanoparticles Decorated on Graphene Nanoribbons. *J. Electroanal. Chem.* **2018**, *823*, 610–616. https://doi.org/10.1016/j.jelechem.2018.07.013.

(69) He, Q.; Liu, J.; Liu, X.; Li, G.; Chen, D.; Deng, P.; Liang, J. A Promising Sensing Platform toward Dopamine Using MnO_2 Nanowires/Electro-Reduced Graphene Oxide Composites. *Electrochim. Acta* **2019**, *296*, 683–692. https://doi.org/10.1016/j.electacta.2018.11.096.

(70) Si, X.; Song, X.; Xu, K.; Zhao, C.; Wang, J.; Liu, Y.; He, S.; Jin, M.; Li, H. Bovine Serum Albumin-Templated MnO_2 Nanoparticles Are Peroxidase Mimics for Glucose Determination by Luminol Chemiluminescence. *Microchem. J.* **2019**, *149*, 104050. https://doi.org/10.1016/j.microc.2019.104050.

(71) Shu, Y.; Gao, J.; Chen, J.; Yan, J.; Sun, J.; Jin, D.; Xu, Q.; Hu, X. A Near−infrared Fluorescent Sensor Based on the Architecture of Low−toxic Ag_2S Quantum Dot and MnO_2 Nanosheet for Sensing Glutathione in Human Serum Sample. *Talanta* **2021**, *221*, 121475. https://doi.org/10.1016/j.talanta.2020.121475.

(72) Li, J.; Jiao, L.; Xu, W.; Yan, H.; Chen, G.; Wu, Y.; Hu, L.; Gu, W. Cobalt Oxyhydroxide Nanosheets Integrating with Metal Indicator Enable Sensitive Detection of Glutathione. *Sensors Actuators, B Chem.* **2021**, *329*, 129247. https://doi.org/10.1016/j.snb.2020.129247.

(73) Ganganboina, A. B.; Dutta Chowdhury, A.; Doong, R. N-Doped Graphene Quantum Dots-Decorated V_2O_5 Nanosheet for Fluorescence Turn Off–On Detection of Cysteine. *ACS Appl. Mater. Interfaces* **2018**, *10* (1), 614–624. https://doi.org/10.1021/acsami.7b15120.

(74) Lin, S.; Cheng, H.; Ouyang, Q.; Wei, H. Deciphering the Quenching Mechanism of 2D MnO_2 Nanosheets towards Au Nanocluster Fluorescence to Design Effective Glutathione Biosensors. *Anal. Methods* **2016**, *8* (19), 3935–3940. https://doi.org/10.1039/C6AY00199H.

(75) Nebu, J.; Anu, K. S.; Anjali Devi, J. S.; Aparna, R. S.; Aswathy, A. O.; Lekha, G. M.; Sony, G. Pottasium Triiodide Enhanced Turn-off Sensing of Tyrosine in Carbon Dot Platform. *Microchem. J.* **2019**, *146*, 12–19. https://doi.org/10.1016/j.microc.2018.12.021.

(76) Ejaz, A.; Jeon, S. Synthesis and Application of Electrochemically Reduced N-RGO-$Co(OH)_2$ Nanocomposite for Concurrent Detection of Biomolecules. *Electrochim. Acta* **2017**, *235*, 709–719. https://doi.org/10.1016/j.electacta.2017.03.036.

(77) Wan, X.; Yang, S.; Cai, Z.; He, Q.; Ye, Y.; Xia, Y.; Li, G.; Liu, J. Facile Synthesis of MnO_2 Nanoflowers/N-Doped Reduced Graphene Oxide Composite and Its Application for Simultaneous Determination of Dopamine and Uric Acid. *Nanomaterials* **2019**, *9* (6), 847. https://doi.org/10.3390/nano9060847.

(78) Yang, D. P.; Guo, W.; Cai, Z.; Chen, Y.; He, X.; Huang, C.; Zhuang, J.; Jia, N. Highly Sensitive Electrochemiluminescence Biosensor for Cholesterol Detection Based on AgNPs-BSA-MnO_2 Nanosheets with Superior Biocompatibility and Synergistic Catalytic Activity. *Sensors Actuators, B Chem.* **2018**, *260*, 642–649. https://doi.org/10.1016/j.snb.2018.01.096.

(79) Liu, J.; Meng, L.; Fei, Z.; Dyson, P. J.; Jing, X.; Liu, X. MnO_2 Nanosheets as an Artificial Enzyme to Mimic Oxidase for Rapid and Sensitive Detection of Glutathione. *Biosens. Bioelectron.* **2017**, *90*, 69–74. https://doi.org/10.1016/j.bios.2016.11.046.

(80) Zeng, X.; Zhang, X.; Zhu, B.; Jia, H.; Yang, W.; Li, Y.; Xue, J. A Colorimetric and Ratiometric Fluorescent Probe for Quantitative Detection of GSH at Physiologically Relevant Levels. *Sensors Actuators, B Chem.* **2011**, *159* (1), 142–147. https://doi.org/10.1016/j.snb.2011.06.062.

(81) Olmos Moya, P. M.; Martínez Alfaro, M.; Kazemi, R.; Alpuche-Avilés, M. A.; Griveau, S.; Bedioui, F.; Gutiérrez Granados, S. Simultaneous Electrochemical Speciation of Oxidized and Reduced Glutathione. Redox Profiling of Oxidative Stress in Biological Fluids with a Modified Carbon Electrode. *Anal. Chem.* **2017**, *89* (20), 10726–10733. https://doi.org/10.1021/acs.analchem.7b01690.

(82) Tomei, M. R.; Cinti, S.; Interino, N.; Manovella, V.; Moscone, D.; Arduini, F. Paper-Based Electroanalytical Strip for User-Friendly Blood Glutathione Detection. *Sensors Actuators B Chem.* **2019**, *294*, 291–297. https://doi.org/10.1016/j.snb.2019.02.082.

(83) Wang, H.; Na, X.; Liu, S.; Liu, H.; Zhang, L.; Xie, M.; Jiang, Z.; Han, F.; Li, Y.; Cheng, S.; Tan, M. A Novel "Turn-on" Fluorometric and Magnetic Bi-Functional Strategy for Ascorbic Acid Sensing and in Vivo Imaging via Carbon Dots-MnO_2 Nanosheet Nanoprobe. *Talanta* **2019**, *201*, 388–396. https://doi.org/10.1016/j.talanta.2019.04.022.

(84) Tehseen, B.; Rehman, A.; Rahmat, M.; Bhatti, H. N.; Wu, A.; Butt, F. K.; Naz, G.; Khan, W. S.; Bajwa, S. Z. Solution Growth of 3D MnO_2 Mesh Comprising 1D Nanofibres as a Novel Sensor for Selective and Sensitive Detection of Biomolecules. *Biosens.*

Bioelectron. **2018**, *117*, 852–859. https://doi.org/10.1016/j.bios.2018.06.061.

(85) Samdani, J.; Samdani, K.; Kim, N. H.; Lee, J. H. A New Protocol for the Distribution of MnO_2 Nanoparticles on RGO Sheets and the Resulting Electrochemical Performance. *Appl. Surf. Sci.* **2017**, *399*, 95–105. https://doi.org/10.1016/j.apsusc.2016.12.086.

(86) Biswas, S.; Pal, A. Visible Light Assisted Fenton Type Degradation of Methylene Blue by Admicelle Anchored Alumina Supported Rod Shaped Manganese Oxide. *J. Water Process Eng.* **2020**, *36*, 101272. https://doi.org/10.1016/j.jwpe.2020.101272.

(87) Li, Q.; Xia, Y.; Wan, X.; Yang, S.; Cai, Z.; Ye, Y.; Li, G. Morphology-Dependent MnO_2/Nitrogen-Doped Graphene Nanocomposites for Simultaneous Detection of Trace Dopamine and Uric Acid. *Mater. Sci. Eng. C* **2020**, *109*, 110615. https://doi.org/10.1016/j.msec.2019.110615.

(88) Çakıroğlu, B.; Demirci, Y. C.; Gökgöz, E.; Özacar, M. A Photoelectrochemical Glucose and Lactose Biosensor Consisting of Gold Nanoparticles, MnO_2 and g-C_3N_4 Decorated TiO_2. *Sensors Actuators B Chem.* **2019**, *282*, 282–289. https://doi.org/10.1016/j.snb.2018.11.064.

(89) Yan, X.; Song, Y.; Zhu, C.; Song, J.; Du, D.; Su, X.; Lin, Y. Graphene Quantum Dot-MnO_2 Nanosheet Based Optical Sensing Platform: A Sensitive Fluorescence "Turn Off-On" Nanosensor for Glutathione Detection and Intracellular Imaging. *ACS Appl. Mater. Interfaces* **2016**, *8* (34), 21990–21996. https://doi.org/10.1021/acsami.6b05465.

(90) Wu, Y.; Deng, P.; Tian, Y.; Magesa, F.; Liu, J.; Li, G.; He, Q. Construction of Effective Electrochemical Sensor for the Determination of Quinoline Yellow Based on Different Morphologies of Manganese Dioxide Functionalized Graphene. *J. Food Compos. Anal.* **2019**, *84*, 103280. https://doi.org/10.1016/j.jfca.2019.103280.

(91) Sinha, L.; Pakhira, S.; Bhojane, P.; Mali, S.; Hong, C. K.; Shirage, P. M. Hybridization of Co_3O_4 and α-MnO_2 Nanostructures for High-Performance Nonenzymatic Glucose Sensing. *ACS Sustain. Chem. Eng.* **2018**, *6* (10), 13248–13261. https://doi.org/10.1021/acssuschemeng.8b02835.

(92) Nemati, F.; Hosseini, M.; Zare-Dorabei, R.; Salehnia, F.; Ganjali, M. R. Fluorescent Turn on Sensing of Caffeine in Food Sample Based on Sulfur-Doped Carbon Quantum Dots and Optimization of Process Parameters through Response Surface Methodology.

Sensors Actuators B Chem. **2018**, *273*, 25–34. https://doi.org/10.1016/j.snb.2018.05.163.

(93) Ma, Z.; Sun, Y.; Xie, J.; Li, P.; Lu, Q.; Liu, M.; Yin, P.; Li, H.; Zhang, Y.; Yao, S. Facile Preparation of MnO_2 Quantum Dots with Enhanced Fluorescence via Microenvironment Engineering with the Assistance of Some Reductive Biomolecules. *ACS Appl. Mater. Interfaces* **2020**, *12* (13), 15919–15927. https://doi.org/10.1021/acsami.0c00917.

CHAPTER-2

Carbon Dot−MnO_2 Nanosphere Composite Sensors for Selective Detection of Glutathione

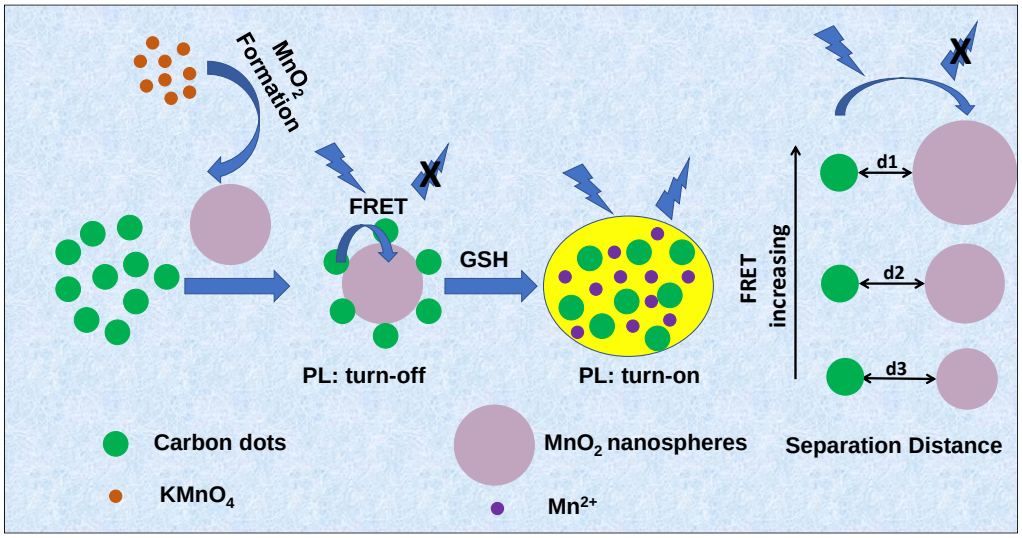

Highlights

- Role of methionine to prepare different sizes of spherical MnO_2 nanoparticles.
- Investigation of binding efficacy between Cdots and different size MnO_2 nanospheres.
- Confirmation of FRET mechanism by quenching of the PL intensity, quantum yields and values of average lifetime.
- Variations of all the photophysical parameters depending upon the size of MnO_2 nanospheres.
- Examination of different Cdots-MnO_2 nanocomposites as turn-off/on sensor to detect GSH.

2.1 Introduction

GSH plays a key part in many biological systems like antioxidants to fight against free radicals and toxins, modulation of cell proliferation, regulate the suitable thiol-disulfide status of proteins, and many others.[1,2] Moreover, due to its significant physiological properties, GSH has many applications in health foods, cosmetics industries, and pharmaceuticals. As a result, currently, selective and sensitive detection of GSH becomes a great field of interest. In recent times, fluorescent nanomaterials have also been broadly used for GSH detection for instance quantum dots,[3] silver nanoparticles,[4] gold nanoparticles,[5] up-conversion nanoparticles,[6] and graphitic C_3N_4.[7] A range of methods have been proposed for preparing Cdots such as arc discharge, calcinations, electrochemical oxidation, laser ablation, hydrothermal approaches, ultrasonic, and microwave pyrolysis approaches, etc.[8] From all the above methods, microwave pyrolysis is an easy, fast, and green approach for the preparation of Cdots.[9]

MnO_2 nanoparticles exhibits a great specific surface area in addition to high capacity to absorb light due to which they are efficient fluorescence quenchers and have great demand for the designing of "turn off−on" fluorescence sensing platforms.[10] Wang et al. designed a FRET-based fluorescent probe which consists of Cdots (energy donor) and MnO_2 nanosheets (energy acceptor) for the selective and sensitive sensing of GSH in human whole blood samples.[11] Among all transition metal oxides, MnO_2 nanostructures are in great demand because of having efficient physical and chemical properties.[12]

Kainth et al., have synthesized four different-size gold nanoparticles (AuNPs) and found that variations of the increment of the particle size led to a bathochromic shift in the SPR peak from 521 to 535 nm. They also observed that the intensity of the existing peak was quenched along with time, and the larger size of AuNPs was extra sensitive for detecting different purines.[13] Zuber et al., synthesized AuNPs of three different sizes, and they performed both absorption and fluorescence techniques. They determined that the limit of quantification of AuNPs was dependent on the size of nanoparticles.[14] From the aforesaid literature observations, it was found that the variation of the particle size affects the sensitivity for the detection of biomolecules. Therefore, there is need to study the role of different sizes of MnO_2 nanospheres with carbon dots for the detection of GSH.

In this present work, the Cdots were synthesized from ascorbic acid (carbon source) and a microwave synthesizer. In addition, MnO_2 nanospheres of different sizes were synthesized at room temperature by changing the ratio of methionine as the stabilizer and

potassium permanganate ($KMnO_4$) as the precursor. The reaction between $KMnO_4$ and methionine is a simple one-step $2e^-$ oxidation−reduction redox reaction leading to the formation of MnO_2 nanospheres.[15] The Cdots-MnO_2 nanocomposites were formed by mixing Cdots and MnO_2 nanospheres. The PL spectrum of Cdots (donor) and absorption spectra of different-size MnO_2 nanospheres (acceptor) were obtained and found an effective overlap region between these two spectra, which suggests that the FRET mechanism took place in Cdots-MnO_2 nanocomposites.[16] Addition of GSH into the Cdot-MnO_2 sensing system would cause a redox reaction among GSH and MnO_2, which turns on/enhances the fluorescence properties of Cdots. In this redox reaction, MnO_2 nanospheres were reduced to Mn^{2+} ions, and GSH was oxidized via the thiol-disulfide exchange reaction to glutathione disulfide.[17] In the present study, the different-size MnO_2 nanospheres were prepared and observed that the efficiency of electron transfer, rate of PL quenching, and PL recovery of Cdots in the presence of GSH gradually enhances as the size of nanospheres rises. The different-size MnO_2 nanospheres also modulate the sensitivity and specificity of the Cdots in the presence of GSH.

2.2 Experimental section

2.2.1 Materials and reagents

L-methionine (99%) and $KMnO_4$ (99%) were utilized for synthesis of water-soluble MnO_2 nanospheres which were bought from Loba Chemie (India). Ascorbic acid (99%, Loba Chemie, India) as a carbon source and kollicoat-IR with molecular weight 45,000 Da as a stabilizer were used in the preparation of Cdots. Ultrapure deionized water was prepared using a double distillation unit, and it was used for cleaning the apparatus and for solution preparations.

2.2.2 Synthesis of Cdots

Initially, 0.1 M ascorbic acid as a precursor and 0.1 M kollicoat as a stabilizing agent were mixed in distilled water (10 mL) with constant stirring (30 min.). After that, the sample was poured into a glass reaction vessel and placed into a Multiwave300 microwave reaction system (Anton Paar, USA) for heating at 130 °C (300 W) for 30 min. The color conversion of sample from colorless to pale yellow indicated the development of Cdots.[18]

2.2.3 Synthesis of different-size MnO_2 nanospheres

The MnO_2 nanospheres were formed through mixing of equivalent stoichiometry of L-methionine (2×10^{-4} mol dm^{-3}) and $KMnO_4$ (2×10^{-4} mol dm^{-3}) in distilled water with

continuous stirring of 20 min at room temperature (RT). The reaction was very fast, and the variation in the color from light pink to brown indicated the formation of MnO_2 nanospheres. The reaction was a one-step, two-electron redox reaction between methionine and Mn(VII).[19] Different-size MnO_2 nanospheres (large (L-Mn NS), medium (M-Mn NS) and small (S-Mn NS)) were synthesized by changing the ratio of concentration of L-methionine and $KMnO_4$ (Table 2.1). Scheme 2.1 shows the synthesis of fluorescent Cdots, different-size MnO_2 nanospheres, and Cdot-MnO_2 composites (by simply mixing Cdots and MnO_2 nanospheres) and the effect of GSH in the synthesized composites.

Table 2.1. MnO_2 nanospheres of different sizes developed by changing the ratio of $KMnO_4$ and methionine and different LOD Values for GSH.

Sr. No.	$KMnO_4$ (mol dm^{-3})	Methionine (mol dm^{-3})	Approx. Size (nm)
L-Mn NS	2×10^{-4}	1×10^{-4}	61±5
M-Mn NS	2×10^{-4}	1×10^{-3}	35±5
S-Mn NS	2×10^{-4}	1×10^{-2}	15±5

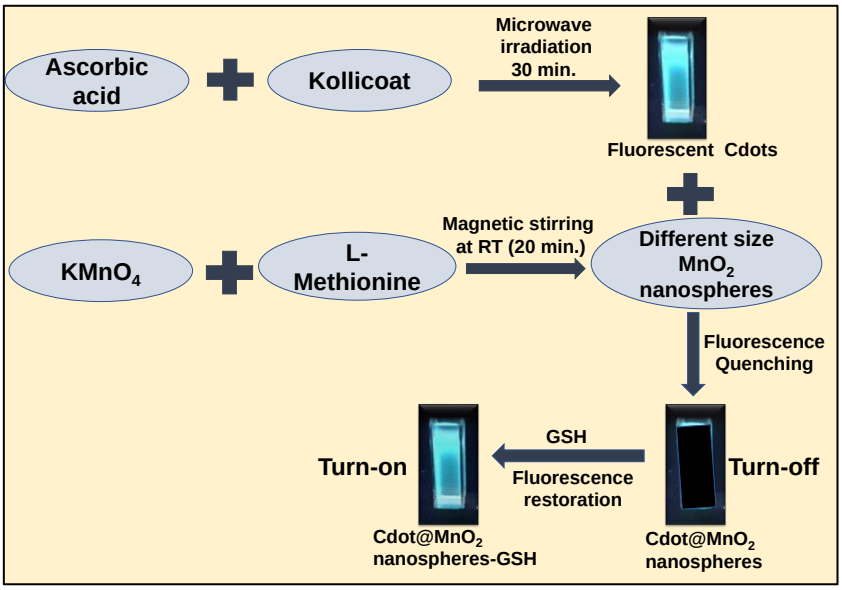

Scheme 2.1. Schematic representation of the synthesized fluorescent Cdots, different size-MnO_2 nanospheres, Cdot-MnO_2 composite, and the effect of GSH in the prepared composite.

2.2.4 Characterization

The absorption spectra of the synthesized materials were noted via a UV−vis spectrophotometer (Analytik Jena, Specord, India), and the fluorescence emission spectra were

also recorded using a spectrofluorometer instrument (PerkinElmer LS-55, USA). The fluorescence lifetime decays were recorded by time-correlated single-photon counting (TCSPC) measurements via a Deltaflex modular fluorescence lifetime system (HORIBA Scientific) through an excitation source at 340 nm (nano-LED pulse diode light). The instrument response function (IRF) of the set-up was 200 ps. The morphology and the size of MnO_2 were examined through a transmission electron microscope (TEM, FEI TecnaiG2 F20). IR spectra were recorded by AT-IR spectroscopy (Agilent Resolution Pro-carry 660).

2.2.5 Preparation of Sample Solutions

Cdots stock solution (100 μL) was pipetted out using a cuvette with the successive addition of 1900 μL of distilled water. Then, the respective amount of solution of MnO_2 nanospheres of different sizes was added in the cuvette for examining the quenching studies of Cdots at pH 6.5. Furthermore, respective amount of GSH was added to determine the fluorescence recovery of Cdots (Scheme 2.1). The fluorescence quantum yield of Cdots with the addition of different-size MnO_2 nanopsheres and GSH was determined w.r.t. quinine sulfate[20] as the reference solution (ϕ_R = 0.546) by using equation 1.1.

2.3 Result and discussion

2.3.1 Characterization

The morphology, shape, and size of the Cdots and MnO_2 nanospheres were analyzed by TEM analysis. The TEM images (Figure 2.1(a-c)) show the sizes of different MnO_2 nanospheres, which were synthesized by using different concentrations of methionine.

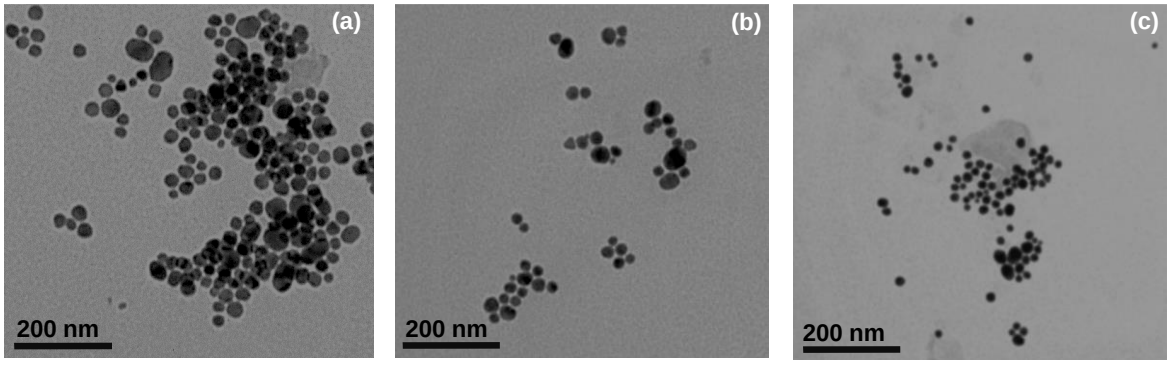

Figure 2.1. TEM image of (a) L-Mn NS, (b) M-Mn NS, and (c) S-Mn NS.

The formation of MnO_2 nanospheres was confirmed by EDS analysis (Figure 2.2). It has been observed that amino acids act as reducing and capping agents for the reduction and stabilization

of metal ions and their nanoparticles, respectively.[21] The concentration of methionine controls the size as well as shape of the nanoparticles.[15] The increase in the concentration of methionine decreases the rate of nucleation due to which the MnO_2 nanosphere size decreases. From the TEM images (Figure 2.1(a-c)), it is confirmed that, the sizes of L-Mn NS, M-Mn NS, and S-Mn NS were 61 ± 5, 35 ± 5, and 15 ± 5 nm, respectively (Table 1).

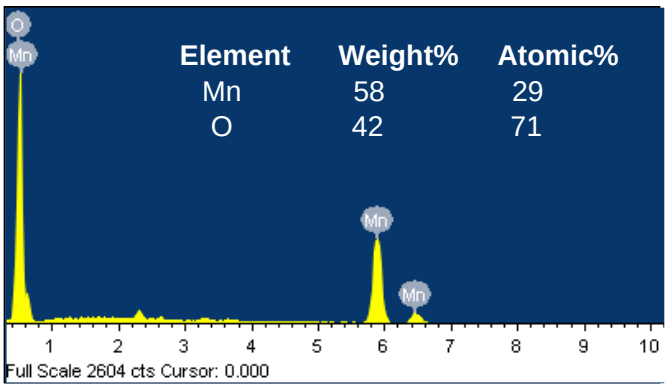

Figure 2.2. The EDS spectra of MnO_2 nanospheres.

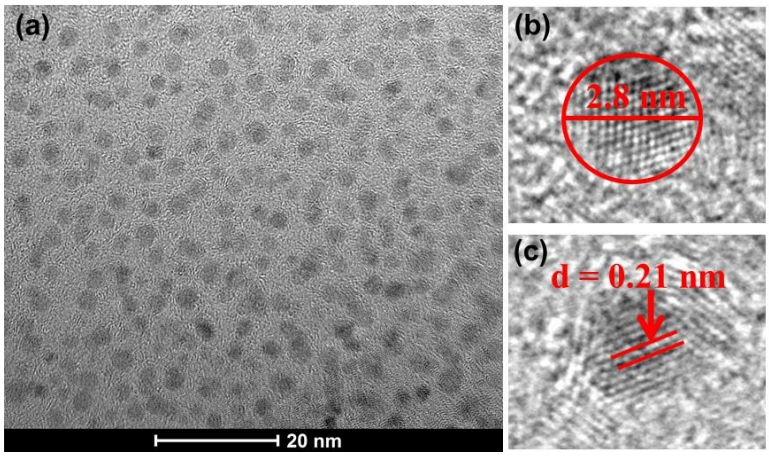

Figure 2.3. (a) TEM image of Cdots, (b) individual particle size of Cdots, and (c) lattice fringes of Cdots.

The morphology and the size distribution of Cdots were characterized by TEM, shown in Figure 2.3(a). The HRTEM result showed that the prepared Cdots have uniform dispersed and spherical features, having an approximate diameter of 2.8 nm (Figure 2.3(b)). In Figure 2.3(c), the HRTEM image shows the lattice fringes having 0.21 nm d-spacing value.

2.3.2 Optical properties

To determine the optical properties of Cdots and MnO_2 nanoparticles, their UV−vis absorption spectra were examined. The absorption spectrum of Cdots displayed a significant

absorption peak at 263 nm, which corresponds to the n−π* transition due to C=O band and the π−π* transition due to conjugated C=C band (Figure 2.4(a)).[22] Upon excitation wavelength of 340 nm (λ_{ex} = 340 nm), the maximum PL emission intensity of Cdots was observed at 420 nm (λ_{em} = 420 nm).

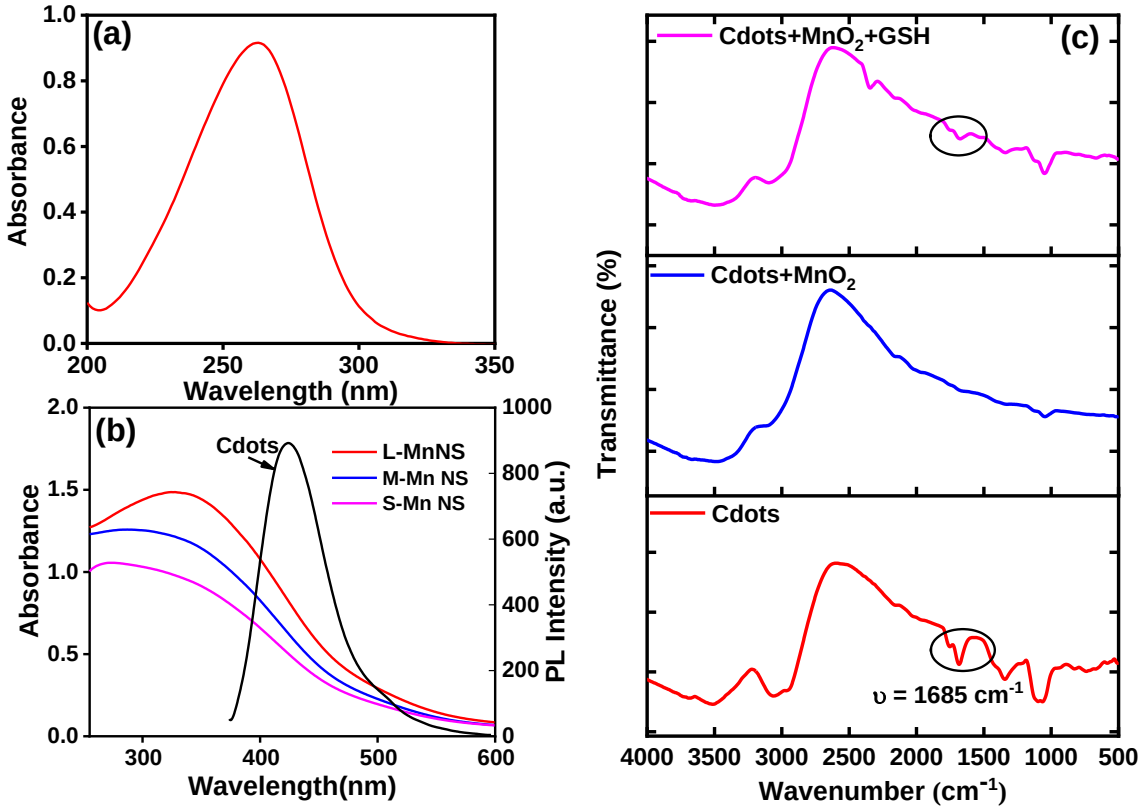

Figure 2.4. (a) UV-Visible spectrum of Cdots, (b) Spectral overlap of the UV−vis absorption spectrum of different size-MnO_2 nanospheres at the equal concentration i.e., 5 μM and the PL emission spectrum of Cdots, and (c) IR spectra of Cdots, Cdots@L-Mn NS system, and addition of GSH in Cdots@L-Mn NS sensing system.

Figure 2.4(b) displays the level of the spectral overlap area among the absorption spectra of different-size MnO_2 nanospheres (L, M, and S-Mn NS) at an identical concentration of 5 μM and the fluorescence emission spectra of Cdots (λ_{ex} = 340 nm). The spectral overlap integral [J(λ)] of Cdots-MnO_2 nanospheres was calculated using the equation 1.8 in which Cdots act as donor and different sizes of MnO_2 nanospheres act as acceptor. From the values of J(λ) and Figure 2.4(b), it was observed that the level of the spectral overlap integral between the emission of Cdots and the extinction enhances with the increase in the size of the MnO_2 nanospheres. It can also be recommended that the FRET takes place from the Cdots (donor) to MnO_2 nanospheres (acceptor), and the extent of FRET enhances upon increasing the size of

the MnO_2 nanospheres. In Figure 2.4(c), the IR spectra of the Cdots show a C=O stretching frequency at 1685 cm^{-1}, which got diminished with the addition of MnO_2 nanospheres due to the interaction between the Cdots and MnO_2 nanospheres. It was also observed that the presence of GSH in the Cdots-MnO_2 sensing system, the diminished peak at 1685 cm^{-1} recovered by the removal of Cdots from the surface of the MnO_2 nanospheres.

2.3.3 Fluorescence quenching of Cdots by MnO_2 nanospheres

The synthesized Cdots exhibited high fluorescence intensity. The different-size MnO_2 nanospheres were added in the Cdots and results in quenching of their fluorescence intensity.

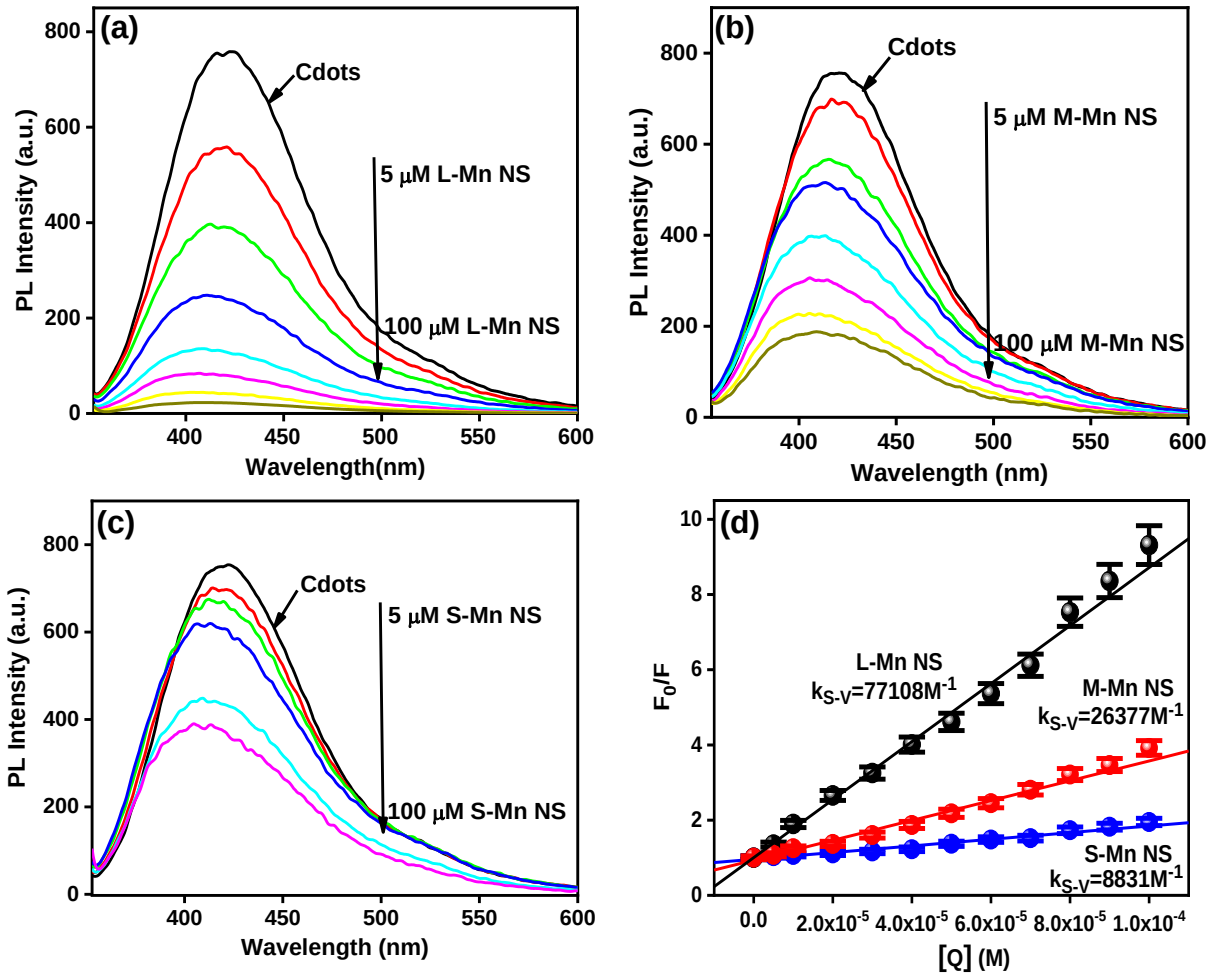

Figure 2.5. Fluorescence quenching spectra of Cdots with different concentrations of (a) L-Mn NS, (b) M-Mn NS, and (c) S-Mn NS and (d) Stern-Volmer quenching plot of S-, M-, and L-Mn NS with Cdots.

The fluorescence quenching mechanism can be attributed to the FRET from the electron-rich Cdots to the electron-deficient MnO_2 nanospheres.[11,17] To understand the fluorescence quenching of Cdots, the concentration of different-sized MnO_2 nanospheres varied in the range of 5 to 100 μM. It was observed that the PL intensity of Cdots was reduced maximum for 100

μM concentration of all three different-size MnO_2 nanospheres (revealed in Figure 2.5 (a-c)). The quenching mechanism can be explained on the basis of holes, and electrons are trapped between of the Cdots and MnO_2 nanospheres, which causes their low availability for the radiative recombination, resulting in fluorescence quenching.[21,23] To comprehend the quenching efficiency level of different-size MnO_2 nanospheres, the graph (Figure 2.5(d)) between F_0/F and different concentration of MnO_2 nanospheres (L, M, and S-Mn NS) were plotted according to the Stern-Volmer equation (1.4). From the slope, the respective K_{SV} values were calculated. The values (K_{SV}) are 77,108, 26,377, and 8831 M^{-1} for large- (L), medium- (M), and small (S)-size MnO_2 nanospheres, respectively.

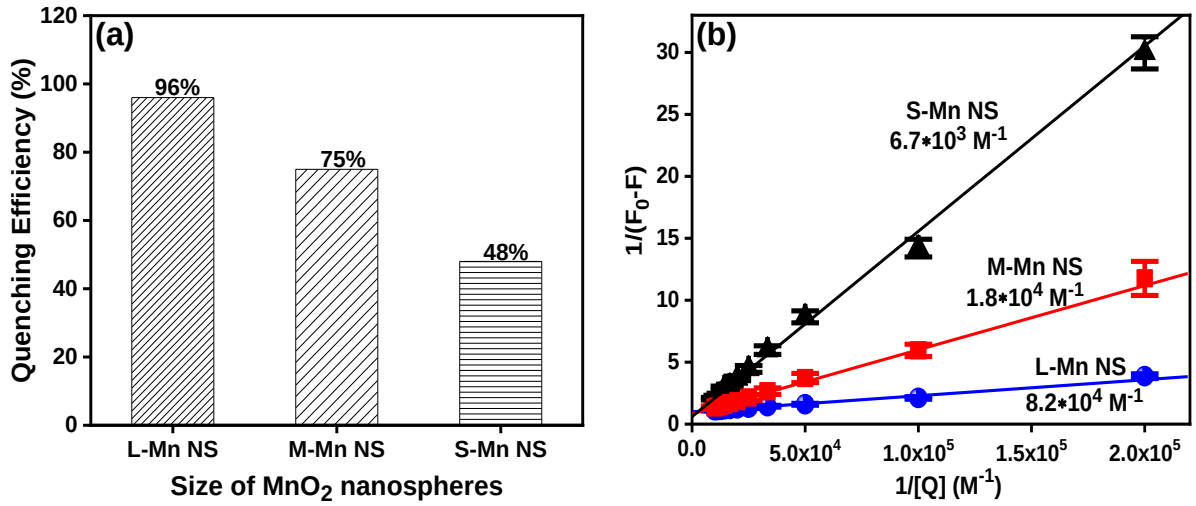

Figure 2.6. (a) Variation of fluorescence quenching efficiency with different sizes of MnO_2 nanospheres and (b) B−H binding plot of S-, M-, and L-Mn NS with Cdots.

Moreover, it was also found from Figure 2.6(a) that the quenching efficiencies of the Cdots in the presence of L, M, and S-Mn NS are 96, 75, and 48%, respectively. From the values of K_{SV} and the quenching efficiency, it can be demonstrated that the extent of PL quenching of Cdots gradually enhances with the increase in the size of the nanospheres. Alternatively, it can also be inferred that the rate of electron transfer from Cdots to MnO_2 nanospheres gradually enhances by the increase in the size of the acceptor. Furthermore, to understand the stoichiometry and the interaction strength between the Cdots with different size MnO_2 nanospheres, the binding constant values were evaluated based on the changes in the fluorescence intensity using the 1:1 linear Benesi−Hildebrand method according to the equation (1.5). The graph of $(1/F-F_0)$ vs 1/[Q] shows a linear plot (Figure 2.6(b)). From the values of slope and intercept, the respective binding constant values (K) of Cdots and different-

size MnO_2 nanospheres were found. It has been observed that the binding efficiency of Cdots gradually enhances upon increasing the size of the MnO_2 nanospheres. The binding constant values of the Cdots in the presence of L, M, and S-Mn NS are 8.2×10^4, 1.8×10^4, and 6.7×10^3 M^{-1}, respectively. The result also demonstrated that upon increasing the size of the nanospheres (S → M → L), there is a greater extent of interaction/electron transfer among the Cdots and MnO_2 nanospheres, which causes variation of the binding constant values of Cdots. The binding constant value of Cdots in the presence of L-Mn-Ns becomes the maximum, which clearly suggests that the electrons are more easily transferred from electron-rich Cdots to electron-deficient large-size particles.

2.3.4 Restoration mechanism of Cdots and detection of GSH

Furthermore, addition of GSH to the different-size Cdots-MnO_2 nanocomposites (L, M, and S-Mn NS) results in restoration of the fluorescence properties (turn on) of Cdots (Figure 2.7(a), (b) and (c)). This kind of fluorescence recovery/ turn on behavior of Cdots is mainly ascribed to the occurrence of redox reaction among MnO_2 and GSH. Upon adding the GSH, there is reduction of MnO_2 to Mn^{2+} ions, while the oxidation of GSH to glutathione disulfide (GSSG),[7,16,24] as shown in the following equation:

$$2GSH + MnO_2 + 2H^+ \rightarrow GSSG + Mn^{2+} + 2H_2O \quad (2.1)$$

As a result, Cdots are removed from the surface of MnO_2 nanospheres, which causes fluorescence recovery of Cdots. In this proposed sensing platform, the Cdots act as the fluorometric reporter, MnO_2 nanospheres as the quencher, and GSH as the detector.[10] Therefore, due to the restoration of the fluorescence properties of Cdots, different-size MnO_2 nanospheres (L, M, and S-Mn NS) were used to form Cdots-MnO_2 nanocomposites, and this system was used for the selective and specific GSH sensing. The fluorescence recovery of Cdots were examined by mixing different amounts of GSH with a fixed amount of (100 μM) different-size Cdots-MnO_2 nanocomposites (L, M, and S-Mn NS). It was investigated that, with enhancing the GSH concentration, the fluorescence intensity of the Cdots-MnO_2 nanocomposites gradually increases (Figure 2.7(a), (b) and (c)). On a very closer look, the binding constant values of Cdots-MnO_2 nanocomposites in the presence of GSH were also evaluated by using the Benesi−Hildebrand method.[25] It was found that the presence of GSH leads to a reduction of the binding constant value of the Cdots-MnO_2 nanocomposites (Figure 2.7(d)).

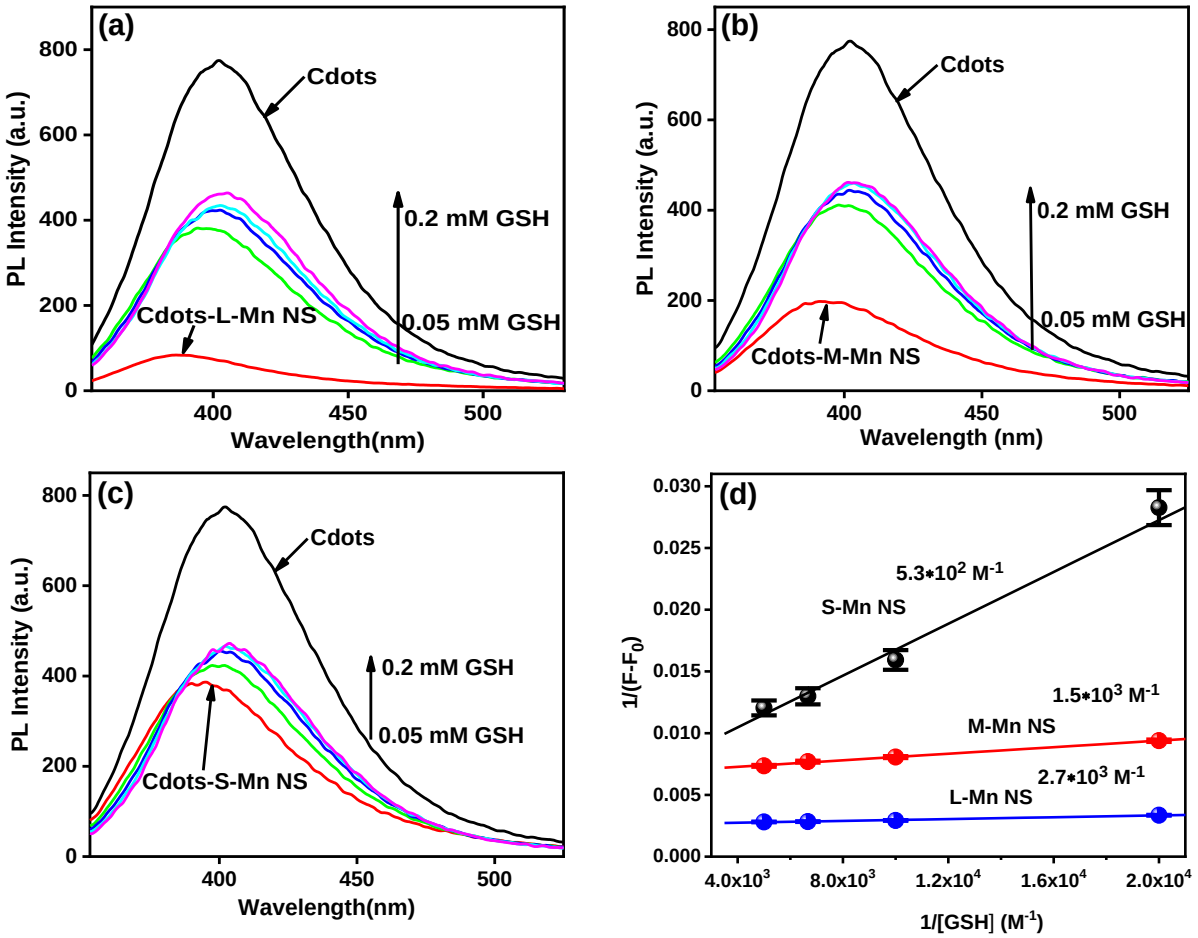

Figure 2.7. Fluorescence restoration of the (a) Cdots-L-Mn NS, (b) Cdots-M-Mn NS, and (c) Cdots-L-Mn NS sensing platform upon addition of 100 µL of GSH (10^{-3} M), respectively and (d) B-H binding plot of S-, M-, and L-Mn NS with GSH.

The binding constant values of the Cdots in the presence of L, M, and S-Mn-NS are 2.7×10^3, 1.5×10^3, and 5.3×10^2 M^{-1}, respectively. This result clearly confirms that the addition of GSH results in elimination of Cdots from the surface of MnO_2 nanosphere. It was also examined that rise in the size of MnO_2 nanospheres leads to steadily enhance the fluorescence intensity (restoration/turn on) of the Cdots and follows the order L-Mn NS > M-Mn NS > S-Mn NS. This result clearly confirms that GSH undergoes a redox reaction with MnO_2 nanospheres and results in removal of Cdots from the surface of MnO_2 nanospheres. Increasing the size of the nanospheres removes the Cdots more efficiently as the strong redox reaction took place between the GSH and large-sized MnO_2 nanospheres. To verify the selectivity of prepared sensing probe for GSH detection, PL emission studies were carried out with the addition of different amino acids, glucose, sucrose, and AA. A specific amount of the Cdots-MnO_2 nanocomposite was mixed with 50 µM concentration of various amino acids like arginine (Arg), histidine (His), aspartic acid (asp), leucine (leu), glycine (gly) and Cys, glucose (glu),

sucrose (suc), AA, and GSH. The significant fluorescence responses were shown only by Cys, AA, and GSH, while the rest of the species showed nominal responses (Figure 2.8(a)). However, GSH showed the maximum fluorescence intensity, which clearly confirms that Cdots-MnO_2 nanocomposites were highly specific and sensitive for the detection of GSH.

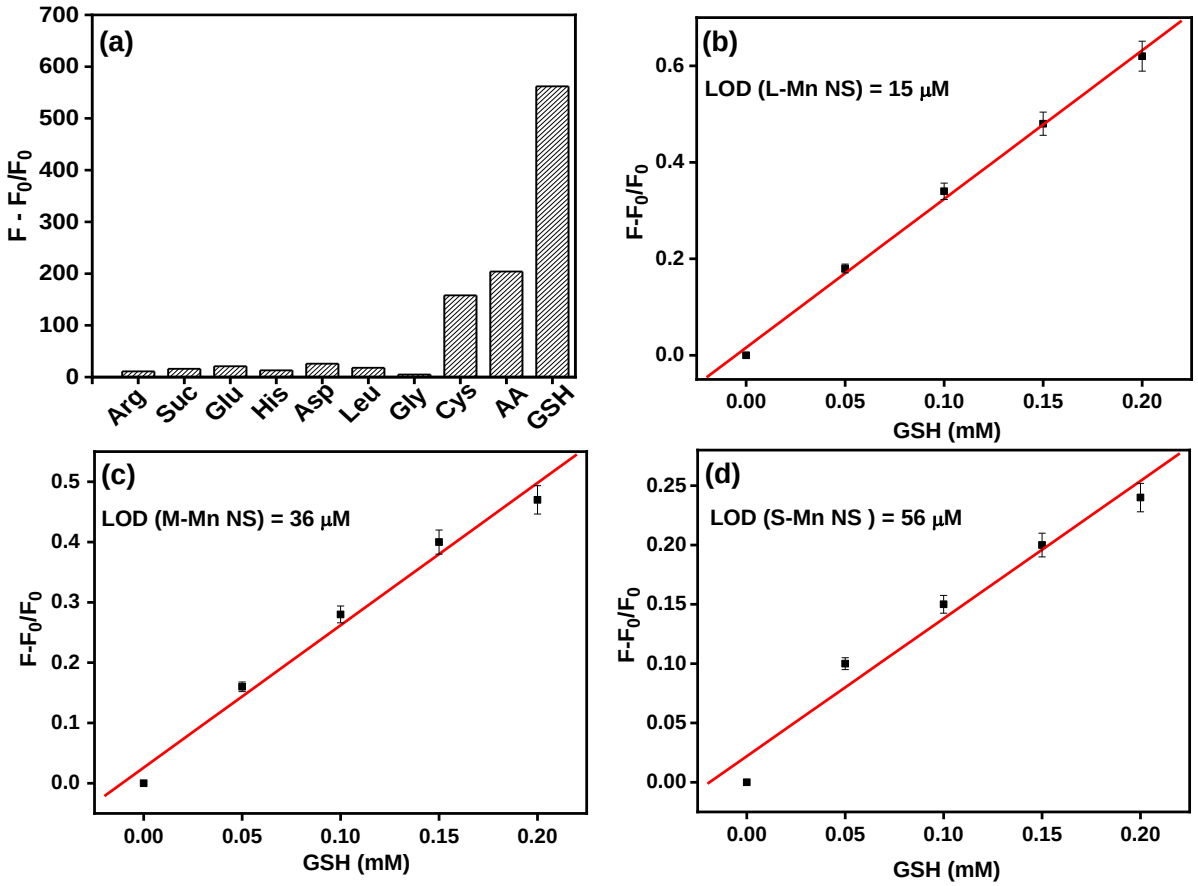

Figure 2.8. (a) Fluorescence response (at 340 nm) of the Cdots-MnO_2 system toward various species, Relationship between fluorescence responses [$(F-F_0)/F_0$] of (b) Cdots-L-Mn NS, (c) Cdots-M-Mn NS, and (d) Cdots-S-Mn NS systems with different concentrations of GSH, respectively.

For all different-size Cdots-MnO_2 nanospheres (L, M, and S-Mn NS), a good linear range was obtained from the plot of $(F-F_0/F_0)$ vs GSH concentration in which, F and F_0 are the PL intensities with and without addition of GSH, respectively.[26] The limit of detection for prepared sensing systems was evaluated by using formula 3 σ /K (σ denotes standard deviation and K denotes the slope of the regression equation). It was observed that L-Mn NS, M-Mn NS, and S-Mn NS showed different limit of detection (LOD) values, and the values are 15, 36, and 56 μM, respectively, as shown in Figure 2.8 (b), (c), and (d), respectively. By comparing the LOD values, it was confirmed that the L-Mn NS showed the best LOD value. Furthermore, the

effectiveness of the prepared sensing probe was justified by comparing with current literature approaches and detecting the probes mentioned in Table 1.1.

2.3.5 Fluorescence quantum yield measurements

The fluorescence quantum yield values of Cdots in different systems were calculated by using equation (1.1) and are tabulated in Table 2.2. From Table 2.2, it has been found that the fluorescence quantum yield (ϕ) values of Cdots are significantly reduced with the addition of different-size MnO_2 nanospheres and follows the order L-Mn NS > M-Mn NS > S-Mn NS. In the presence of L-Mn NS, M-Mn NS, and S-Mn NS, the fluorescence quantum yield values of Cdots are quenched ~17, ~3.4, and ~2 times, respectively. Furthermore, the ϕ values of different Cdots-MnO_2 nanocomposites in the presence of GSH were also calculated, which are tabulated in Table 2.2. It was found that the presence of GSH results in a significant enhancement of the ϕ value for Cdots. In the presence of GSH, the extent of the ϕ value of Cdots is also dependent on the size of the MnO_2 nanospheres. For L, M, and S-Mn-NS, the restoration of the ϕ values of the Cdots in the presence of GSH is ~12, ~2.3, and ~1.3 times, respectively, compared to the respective size of the Cdots-MnO_2 nanocomposites. The restoration of the ϕ value of Cdots follows the order L-Mn NS > M-Mn NS > S-Mn NS.

2.3.6 Time-resolved emission studies

Cdots showed an average lifetime value of 4.40 ns. Addition of different-size MnO_2 nanospheres results in significant quenching of the lifetime values (Figure 2.9).

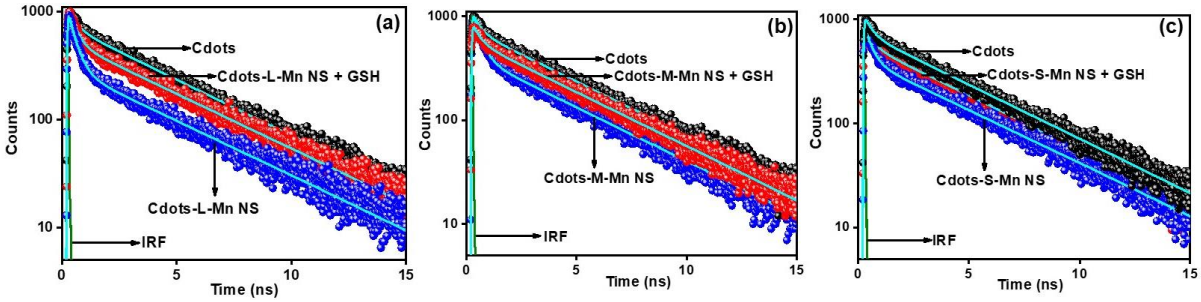

Figure 2.9. Fluorescence lifetime study of Cdots in (a) L-Mn NS, (b) M-Mn NS, and (c) S-Mn NS and with the addition of GSH.

Table 2.2 depicts the average lifetime values of Cdots with the different-size MnO_2 nanospheres. It was observed that the percentage of quenching of Cdots for L-Mn NS, M-Mn NS, and S-Mn NS was 27, 14, and 7%, respectively. The quenching of the average lifetime values of Cdots with MnO_2 nanospheres clearly demonstrated that electron transfer takes place

from the electron-rich surface of the Cdots (donor) to the electron-deficient surface of MnO_2 nanospheres (acceptor). Addition of GSH to the Cdots-MnO_2 nanospheres (L, M, and S-Mn-NS) results in restoration of the fluorescence properties (turn on) of Cdots. The average lifetime values of the Cdots with the addition of GSH significantly are enhanced compared to those of the respective different-size Cdots-MnO_2 nanospheres (Table 2.2).

Table 2.2. Photophysical parameters of Cdots, different size-MnO_2 nanospheres, and GSH.[a]

Systems	ϕ	τ_{av} **(ns)**	k_r **($\times 10^9$ s^{-1})**	k_{nr} **($\times 10^9$ s^{-1})**	k_{ET} **($\times 10^9$ s^{-1})**	ϕ_{EET} **(τ_D)**	ϕ_{EET} **(ϕ_D)**
Cdots	0.68	4.40	0.155	0.07	-	-	-
Cdots+ L-Mn NS	0.04	3.17	0.01	0.30	0.09	0.28	0.94
Cdots+ L-Mn NS +GSH	0.48	4.32	0.11	0.12	4×10^{-3}	0.02	0.29
Cdots+ M-Mn NS	0.20	3.78	0.05	0.21	0.04	0.14	0.71
Cdots+ M-Mn NS +GSH	0.46	4.32	0.11	0.12	4×10^{-3}	0.02	0.32
Cdots+ S-Mn NS	0.34	4.07	0.08	0.16	0.02	0.08	0.50
Cdots+ S-Mn NS +GSH	0.45	4.32	0.10	0.13	4×10^{-3}	0.02	0.34

[a]Experimental error ±5 %

The rate of electron transfer gradually increases by increasing the size of MnO_2 nanospheres (Table 2.2). Moreover, by the addition of GSH, the average lifetime value enhances up to 4.32 ns for all Cdot-MnO_2 nanospheres, and the percentage of turn on values was 26, 12, and 5% for L-Mn NS, M-Mn NS, and S-Mn NS, respectively. This result also clearly depicts that restoration of fluorescence properties also enhances upon increasing the size of MnO_2 nanospheres. From the τ_{av} values and ϕ, the different k_r and k_{nr} values were examined via the equations (1.2 and 1.3). The values of k_r and k_{nr} are listed in Table 2.2. It was found that the k_{nr} values of Cdots increase by a factor of 4.3, 3, and 2.29 times, respectively, while k_r values decrease by a factor of 0.06, 0.32, and 0.52 times, respectively, in the presence of L-Mn NS, M-Mn NS, and S-Mn NS. These results clearly suggested that the quenching phenomenon of Cdots is attributed to the excited-state electron transfer, which is further dependent on the size of the nanospheres. k_{ET} has been estimated using the equation (1.6) in which different-size MnO_2 nanospheres act as quencher. The calculated k_{ET} values are 0.09×10^9, 0.04×10^9, and 0.02×10^9 s^{-1} for L-Mn NS, M-Mn NS, and S-Mn NS, respectively, which demonstrated that the rate of electron transfer of Cdots enhances upon increasing the size of

the nanospheres. ϕ_{EET} is determined using the equation (1.7). The estimated EET from both the quantum yield [$\phi_{EET}(\phi_D)$] and lifetime values [ϕ_{EET} (τ_D)] gradually increases upon increasing the size of the nanospheres (Table 2.2).

Table 2.3. Förster distance, efficiency and separation distance of Cdots and different size MnO_2 nanospheres.[b]

Systems	R_0 (Å)	E (%)	r (nm)
Cdots	-	-	-
Cdots+ L-Mn NS	32.90 Å	22.5	2.53
Cdots+ M-Mn NS	54.50 Å	13	3.88
Cdots+ S-Mn NS	73.70 Å	7.7	5.0

[b]Experimental error ±5 %

The FRET efficiency (E) of the Cdots with the addition of different-size MnO_2 nanospheres was estimated using the equation (1.9). It can be seen from Table 2.3 that the FRET efficiency of Cdots significantly enhances upon increasing the size of the MnO_2 nanospheres. Similarly, from the k_{ET} and ϕ_{EET} values, it has been clearly concluded that the FRET mechanism is more favorable in the case of large-size MnO_2 nanospheres. Moreover, the R_0 values for Cdots and different-size MnO_2 nanospheres were estimated using the following equation (1.10) in which R_0 represents the distance from the centre of the donor (Cdots) to the center of the acceptor (different-size MnO_2 nanospheres). The estimated R_0 values for Cdots and large, medium, and small MnO_2 nanospheres are 32.90, 54.50, and 74.70 Å, respectively, which confirms that the interaction among the Cdots and MnO_2 nanospheres obeys the classical FRET theory (Table 2.3).[27] Moreover, the separation distance among the Cdots and different-size MnO_2 nanospheres from the respective FRET efficiency values by using the equation (1.11). The r values gradually decrease upon increasing the size of the MnO_2 nanospheres (2.53, 3.88, and 5 nm for L, M, and S-M MnO_2 nanospheres, respectively), which confirms that the FRET efficiency is the maximum in the case of large-size MnO_2 nanospheres due to their shorter distance (Table 2.3).

Conclusion

In this Chapter, a rapid fluorometric nanosensor is designed by combining carbon dots (Cdots) and MnO_2 nanoparticles of different sizes for the detection of GSH. The bottom-up approach includes the microwave method for the preparation of the water-soluble and highly fluorescent Cdots by using ascorbic acid as a precursor. MnO_2 nanospheres of different sizes

(large, medium, and small) were prepared by varying the ratio of the concentration of methionine and $KMnO_4$ at room temperature, which was confirmed by HRTEM analysis. The successive addition of MnO_2 nanospheres in Cdots results in fluorescence quenching. From the fluorescence intensity data, Stern−Volmer quenching constant values (K_{SV}) were determined, which depicts that the extent of fluorescence quenching gradually increases with the increase in the size of the MnO_2 nanospheres. Moreover, the fluorescence quantum yield and lifetime studies of Cdots in the presence of different-size MnO_2 nanospheres were also conducted, which clearly demonstrated that the FRET mechanism occurred from the electron-rich surface of Cdots to the electron-deficient MnO_2 nanospheres. From the fluorescence intensity and lifetime analysis, it was found that the degree of fluorescence quenching of Cdots follows the order: large > medium > small. Moreover, fluorescence recovery studies were also performed in the presence of GSH and follows same trend. A redox reaction between GSH and MnO_2 is the strategy of the proposed sensing system, which includes the decomposition of the Cdots@MnO_2 nanocomposite and results in the fluorescence restoration (turn on) of Cdots due to the transformation from MnO_2 to Mn^{2+}. The limits of detection of GSH in the presence of Cdots were also evaluated, and the values were 15, 36, and 56 μM for large, medium, and small MnO_2 nanospheres. Hence, the variation in the size of MnO_2 nanospheres in the developed sensing system put a great impact on the sensing of GSH.

References

(1) Zhang, J.; Hu, Z; Chen, X. Quantification of Glutathione and Glutathione Disulfide in Human Plasma and Tobacco Leaves by Capillary Electrophoresis with Laser-Induced Fluorescence Detection. *Talanta* **2005**, *65* (4), 986–990. https://doi.org/10.1016/j.talanta.2004.08.030.

(2) Krishna Kumar, A. S.; Tseng, W.-B.; Wu, M.-J.; Huang, Y.-Y.; Tseng, W.-L. L-Cystine-Linked BODIPY-Adsorbed Monolayer MoS_2 Quantum Dots for Ratiometric Fluorescent Sensing of Biothiols Based on the Inner Filter Effect. *Anal. Chim. Acta* **2020**, *1113*, 43–51. https://doi.org/10.1016/j.aca.2020.04.006.

(3) Chen, J.; Huang, Z.; Meng, H.; Zhang, L.; Ji, D.; Liu, J.; Yu, F.; Qu, L.; Li, Z. A Facile Fluorescence Lateral Flow Biosensor for Glutathione Detection Based on Quantum Dots-MnO_2 Nanocomposites. *Sensors Actuators B Chem.* **2018**, *260*, 770–777. https://doi.org/10.1016/j.snb.2018.01.101.

(4) Detsri, E.; Seeharaj, P. Colorimetric Detection of Glutathione Based on Phthalic Acid Assisted Synthesis of Silver Nanoparticles. *Colloids Surfaces A Physicochem. Eng. Asp.* **2017**, *533*, 125–132. https://doi.org/10.1016/j.colsurfa.2017.08.037.

(5) Shi, Y.; Pan, Y.; Zhang, H.; Zhang, Z.; Li, M.-J.; Yi, C.; Yang, M. A Dual-Mode Nanosensor Based on Carbon Quantum Dots and Gold Nanoparticles for Discriminative Detection of Glutathione in Human Plasma. *Biosens. Bioelectron.* **2014**, *56*, 39–45. https://doi.org/10.1016/j.bios.2013.12.038.

(6) Deng, R.; Xie, X.; Vendrell, M.; Chang, Y.-T.; Liu, X. Intracellular Glutathione Detection Using MnO_2 -Nanosheet-Modified Upconversion Nanoparticles. *J. Am. Chem. Soc.* **2011**, *133* (50), 20168–20171. https://doi.org/10.1021/ja2100774.

(7) Zhang, X. L.; Zheng, C.; Guo, S. S.; Li, J.; Yang, H. H.; Chen, G. Turn-on Fluorescence Sensor for Intracellular Imaging of Glutathione Using g-C_3N_4 Nanosheet-MnO_2 Sandwich Nanocomposite. *Anal. Chem.* **2014**, *86* (7), 3426–3434. https://doi.org/10.1021/ac500336f.

(8) Wang, T.-Y.; Chen, C.-Y.; Wang, C.-M.; Tan, Y. Z.; Liao, W.-S. Multicolor Functional Carbon Dots via One-Step Refluxing Synthesis. *ACS Sensors* **2017**, *2* (3), 354–363. https://doi.org/10.1021/acssensors.6b00607.

(9) Chamoli, P.; Shukla, R. K.; Bezbaruah, A. N.; Kar, K. K.; Raina, K. K. Microwave-Assisted Rapid Synthesis of Honeycomb Core-ZnO Tetrapods Nanocomposites for Excellent Photocatalytic Activity against Different Organic Dyes. *Appl. Surf. Sci.* **2021**, *555*, 149663. https://doi.org/10.1016/j.apsusc.2021.149663.

(10) Yan, X.; Song, Y.; Zhu, C.; Song, J.; Du, D.; Su, X.; Lin, Y. Graphene Quantum Dot-MnO_2 Nanosheet Based Optical Sensing Platform: A Sensitive Fluorescence "Turn Off-On" Nanosensor for Glutathione Detection and Intracellular Imaging. *ACS Appl. Mater. Interfaces* **2016**, *8* (34), 21990–21996. https://doi.org/10.1021/acsami.6b05465.

(11) Wang, Y.; Jiang, K.; Zhu, J.; Zhang, L.; Lin, H. A FRET-Based Carbon Dot-MnO_2 Nanosheet Architecture for Glutathione Sensing in Human Whole Blood Samples. *Chem. Commun.* **2015**. https://doi.org/10.1039/c5cc04905a.

(12) Mehta, A.; Basu, S. Controlled Photocatalytic Hydrolysis of Nitriles to Amides by Mesoporous MnO_2 Nanoparticles Fabricated by Mixed Surfactant Mediated Approach.

J. Photochem. Photobiol. A Chem. **2017**, *343*, 1–6. https://doi.org/10.1016/j.jphotochem.2017.04.013.

(13) Kainth, S.; Mehta, A.; Mishra, A.; Basu, S. Implementation of a Logic Gate by Chemically Induced Nitrogen and Oxygen Rich C-Dots for the Selective Detection of Fluoride Ions. *New J. Chem.* **2018**, *42* (14), 12162–12171. https://doi.org/10.1039/C8NJ02041H.

(14) Zuber, A.; Purdey, M.; Schartner, E.; Forbes, C.; van der Hoek, B.; Giles, D.; Abell, A.; Monro, T.; Ebendorff-Heidepriem, H. Detection of Gold Nanoparticles with Different Sizes Using Absorption and Fluorescence Based Method. *Sensors Actuators B Chem.* **2016**, *227*, 117–127. https://doi.org/10.1016/j.snb.2015.12.044.

(15) Khan, Z.; Ahmed Al- Thabaiti, S.; Yousif Obaid, A.; Khan, Z. A. MnO_2 Nanostructures of Different Morphologies from Amino Acids–MnO^{4-} Reactions in Aqueous Solutions. *Colloids Surfaces B Biointerfaces* **2010**, *81* (1), 381–384. https://doi.org/10.1016/j.colsurfb.2010.07.004.

(16) Wang, Q.; Zhang, Y.; Wang, X.; Wu, Y.; Dong, C.; Shuang, S. Dual Role of BSA for Synthesis of MnO_2 Nanoparticles and Their Mediated Fluorescent Turn-on Probe for Glutathione Determination and Cancer Cell Recognition. *Analyst* **2019**, *144* (6), 1988–1994. https://doi.org/10.1039/c8an02501k.

(17) He, D.; Yang, X.; He, X.; Wang, K.; Yang, X.; He, X.; Zou, Z. A Sensitive Turn-on Fluorescent Probe for Intracellular Imaging of Glutathione Using Single-Layer MnO_2 Nanosheet-Quenched Fluorescent Carbon Quantum Dots. *Chem. Commun.* **2015**, *51* (79), 14764–14767. https://doi.org/10.1039/c5cc05416h.

(18) Garg, D.; Mehta, A.; Mishra, A.; Basu, S. A Sensitive Turn on Fluorescent Probe for Detection of Biothiols Using MnO_2@carbon Dots Nanocomposites. *Spectrochim. Acta Part A Mol. Biomol. Spectrosc.* **2018**, *192*, 411–419. https://doi.org/10.1016/j.saa.2017.11.041.

(19) Zaheer, Z.; Rafiuddin. Formation, Characterisation and Redox Behaviour of Water-Soluble Colloidal Manganese Dioxide. *J. Exp. Nanosci.* **2012**, *7* (1), 74–84. https://doi.org/10.1080/17458080.2010.501965.

(20) Crosby, G. A.; Demas, J. N. Measurement of Photoluminescence Quantum Yields.

Review. *J. Phys. Chem.* **1971**, *75* (8), 991–1024. https://doi.org/10.1021/j100678a001.

(21) Zaheer, Z.; Rafiuddin. Preparation, Characterisation and Kinetics of Corn-Shaped Ag Nanoparticles. *J. Exp. Nanosci.* **2012**, *7* (4), 366–377. https://doi.org/10.1080/17458080.2010.520417.

(22) Jia, X.; Li, J.; Wang, E. One-Pot Green Synthesis of Optically PH-Sensitive Carbon Dots with Upconversion Luminescence. *Nanoscale* **2012**, *4* (18), 5572. https://doi.org/10.1039/c2nr31319g.

(23) Mehta, A.; Mishra, A.; Kainth, S.; Basu, S. Carbon Quantum Dots/TiO_2 Nanocomposite for Sensing of Toxic Metals and Photodetoxification of Dyes with Kill Waste by Waste Concept. *Mater. Des.* **2018**, *155*, 485–493. https://doi.org/10.1016/j.matdes.2018.06.015.

(24) Zhao, L.; Ge, X.; Zhao, H.; Shi, L.; Capobianco, J. A.; Jin, D.; Sun, L. Double-Sensitive Drug Release System Based on MnO_2 Assembled Upconversion Nanoconstruct for Double-Model Guided Chemotherapy. *ACS Appl. Nano Mater.* **2018**, *1* (4), 1648–1656. https://doi.org/10.1021/acsanm.8b00134.

(25) Hildebrand, J. H.; Benesi H. A. Interaction of Iodine with Aromatic Hydrocarbons. *Nature* **1949**, *164* (4179), 963–963. https://doi.org/10.1038/164963b0.

(26) Li, H.; Jin, L.; Kan, Y.; Yin, B. A Visual and "Turn-on" Fluorescent Probe for Rapid Detection of Cysteine over Homocysteine and Glutathione. *Sensors Actuators B Chem.* **2014**, *196*, 546–554. https://doi.org/10.1016/j.snb.2014.02.052.

(27) Lakowicz, J. R. *Principles of Fluorescence Spectroscopy*; Lakowicz, J. R., Ed.; Springer US: Boston, MA, 2006. https://doi.org/10.1007/978-0-387-46312-4.

CHAPTER-3

Morphology-Dependent Performance of MnO_2 Nanostructure Carbon Dots-Based Biosensors for the Detection of Glutathione

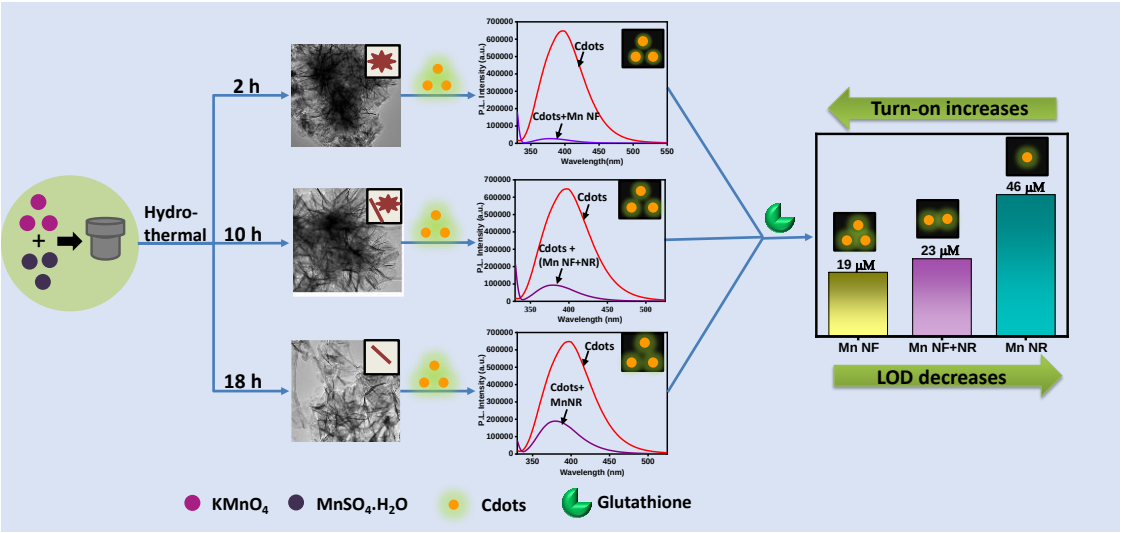

Highlights

- Synthesis of different morphologies of MnO_2 nanostructure by hydrothermal method.
- Study of comparative photophysical parameters of Cdots@different morphologies of MnO_2.
- Variations in the energy transfer rate among Cdots and different morphologies of MnO_2 nanosensor.
- Different specific surface area of MnO_2 nanostructure effect the sensing efficacy of GSH.
- Comparative analysis of fluorescence recovery rate among different nanosensors in presence of GSH.

3.1 Introduction

The properties of nanomaterials can be tuned by controlling their size, shape, crystallographic orientation, and morphology.[1,2] Shape control becomes the most important technique for improving the activity of nanomaterials.[3] An interdependent relationship has been observed between the structure, property, and performance of nanomaterials.[4] MnO_2 has become an active material in the field of biosensing among different transition-metal oxides due to its attractive properties.[5] Currently, a variety of approaches (e.g., solid-state, refluxing, hydrothermal treatment, and sol−gel) have been reported for the preparation of different-shaped MnO_2 nanostructures along with their changed crystal structures from either the reduction of MnO^{4-} or oxidation of Mn^{2+}.[6] Different kinds of reaction conditions like pH, concentrations of the substrate, temperature, reactants, counter cations, and anions are also responsible for the variation of different morphologies of nanostructures and their crystalline phases.[7] Wu et al.[3] synthesized MnO_2 nanoparticles of different morphologies such as NW, NR, and NT. They found that the sensing activity was dependent on the different shapes or morphologies of MnO_2 nanoparticles. Li et al.[8] synthesized nanohybrids of nitrogen-doped graphene (NG) and four MnO_2 nanostructures of different morphologies which include NW, NR, NT, and NF. The electrochemical measurements showed that MnO_2NFs@NG system act as best for detection of DA and UA as compared to other morphologies owing great surface area, extraordinary porous structure, many active sites, etc. Therefore, there is need to study the impact of different morphologies of MnO_2 with Cdots as a fluorescent sensing probe for the GSH detection.

In this study, ascorbic acid (carbon precursor) was used for the preparation of Cdots through a one-pot microwave-assisted method. Also, different shapes of MnO_2 nanostructures were prepared via an optimized hydrothermal method.[8] Three different shapes of MnO_2 nanostructures, that is, NF, NF + NR, and NR, were synthesized and characterized by TEM analysis. The nanocomposites of Cdots with MnO_2 nanostructures were prepared by mixing the two solutions with sonication. The synthesized different-shape Cdot-MnO_2 nanostructures act as turn-off sensors with PL quenching. Furthermore, the GSH sensing was studied in the presence of synthesized various shapes of Cdot-MnO_2 nanostructures which were rationalized as a turn-on sensor with an enhancement of the fluorescence. A redox reaction would occur among MnO_2 and GSH in the presence of GSH in the Cdot-MnO_2 sensing solution. This redox reaction increases the fluorescence of Cdots by the conversion of MnO_2 to Mn^{2+} ions, and GSH

gets oxidized to GSH disulfide through a thiol-disulfide exchange reaction.[9] The different shapes of the MnO_2 nanostructure had a great impact on their interaction with Cdots and GSH. Also, it was found that the variation in the shape of the MnO_2 nanostructure modulates the sensitivity of GSH.

3.2 Experimental section

3.2.1 Materials and reagents

Hydrated manganese sulfate ($MnSO_4 \cdot H_2O$) (99%) and $KMnO_4$ (99%) were bought from Loba Chemie (India) and these were utilized to prepare different morphologies of MnO_2 nanostructures. GSH was purchased from Hi-media and was further used for sensing. Ultrapure deionized (DI) water was prepared by the double-distillation unit and further used for preparing all stock solutions.

3.2.2 Synthesis of Cdots

The Cdots were synthesized by same method as reported in Chapter 2 (section 2.2.2).

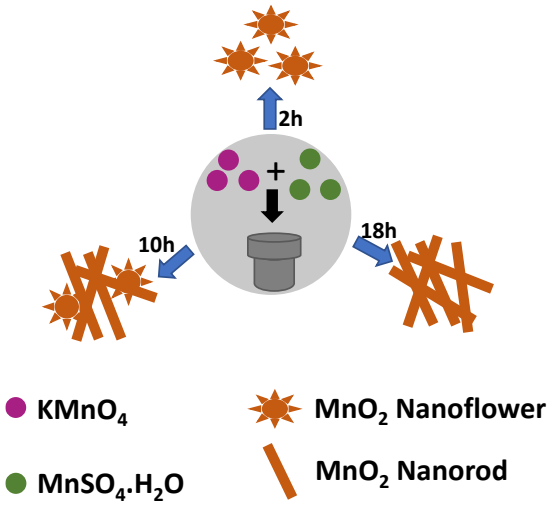

Scheme 3.1. Schematic diagram of the synthesis of MnO_2 nanostructures with different morphologies.

3.2.3 Method for preparation of different morphologies of MnO_2 nanostructure

Different morphologies of MnO_2 nanostructure were synthesized from $MnSO_4 \cdot H_2O$ and $KMnO_4$ solutions through the hydrothermal method. Further, 0.2 and 0.5 g of $MnSO_4 \cdot H_2O$ and $KMnO_4$, respectively, were well dissolved in 100 mL of DI water. The dissolved solution of $KMnO_4$ and $MnSO_4$ was poured into a Teflon-lined pressure vial and then placed in furnace

at 140 °C for three different reaction times, that is, 2, 10, and 18 h (Scheme 3.1). The pressure vial was cooled down to normal temperature with the completion of the reaction. The precipitates of MnO_2 formed were further washed with DI water so that the pH of the supernatant becomes neutral, and at last, MnO_2 precipitates were dried at 100 °C.[10] According to their morphology, the MnO_2 nanostructures were named Mn NF, Mn NF + NR, and Mn NR for the dwell times of 2, 10, and 18 h, respectively.

3.2.4 Characterization

Absorption and emission spectra of Cdot-MnO_2 nanostructures were recorded via a UV−visible spectrophotometer (Analytik Jena, Specord, India) and fluorescence spectrofluorometer (Shimadzu, RF-6000). The different morphologies or shapes of the MnO_2 nanostructure were examined through TEM (FEI TecnaiG2 F20). The phase identification of the prepared MnO_2 nanostructure was studied by XRD (PANalytical X'Pert PRO) in which Cu Kα (λ = 1.540 Å) used as the radiation source ($0 \leq 2\theta \leq 90°$). The surface areas of the different morphologies of MnO_2 nanostructures were recorded via the Brunauer−Emmett−Teller (BET) surface area analyzer of BEL-miniII, Microtrac Corp. Pvt. Ltd., Japan. The fluorescence lifetime decays were recorded by TCSPC measurements using the Deltaflex modular fluorescence lifetime system (manufacturing unit HORIBA Scientific) with an excitation source at 340 nm (nano-LED pulse diode light).

3.2.5 Preparation of Sample Solutions

The stock solutions of MnO_2 nanostructure (different morphologies) of specific concentrations were prepared. The sensing solutions (Cdot-MnO_2 nanostructures) were formed by the addition of the respective shape of the MnO_2 nanostructure to the solution of Cdots in 2 mL of distilled water. The detection of GSH was evaluated by mixing different concentrations of GSH (0−150 μM) with Cdot-MnO_2 nanocomposites. The sample was further placed for the incubation time of 10 min. Finally, the solution was transferred to a 3 mL glass cuvette. The emission spectra of the above prepared samples were recorded at the λ_{ex} = 340 nm.

3.3 Result and discussion

3.3.1 Characterization

The morphology of the MnO_2 nanostructure prepared at 2, 10, and 18 h was observed as NF (Figure 3.1(a)), a mixture of NFs and NRs (Figure 3.1(b)), and only NRs (Figure 3.1(c)) by TEM analysis. It was found that the ratio of NFs to NRs and the crystalline nature of the

MnO_2 nanostructure enhanced with an increment of the time duration of the reaction. Therefore, the final morphology formed of the MnO_2 nanostructures was strongly correlated with the dwell time. An average d-spacing, that is, 0.35 nm, was determined in the lattice-resolved high-resolution TEM (HR-TEM) images of MnO_2 NF (Figure 3.1(d)), MnO_2 NF + NR (Figure 3.1(e)), and MnO_2 NF (Figure 3.1(f)), which was indexed to the separation between (220) lattice planes.[8] It shows that all three different shapes of the MnO_2 nanostructure have the same d-spacing value and correspond to (220) lattice planes. The morphology and the size of Cdots were characterized by TEM, shown in Chapter 2 (Figure 2.3).

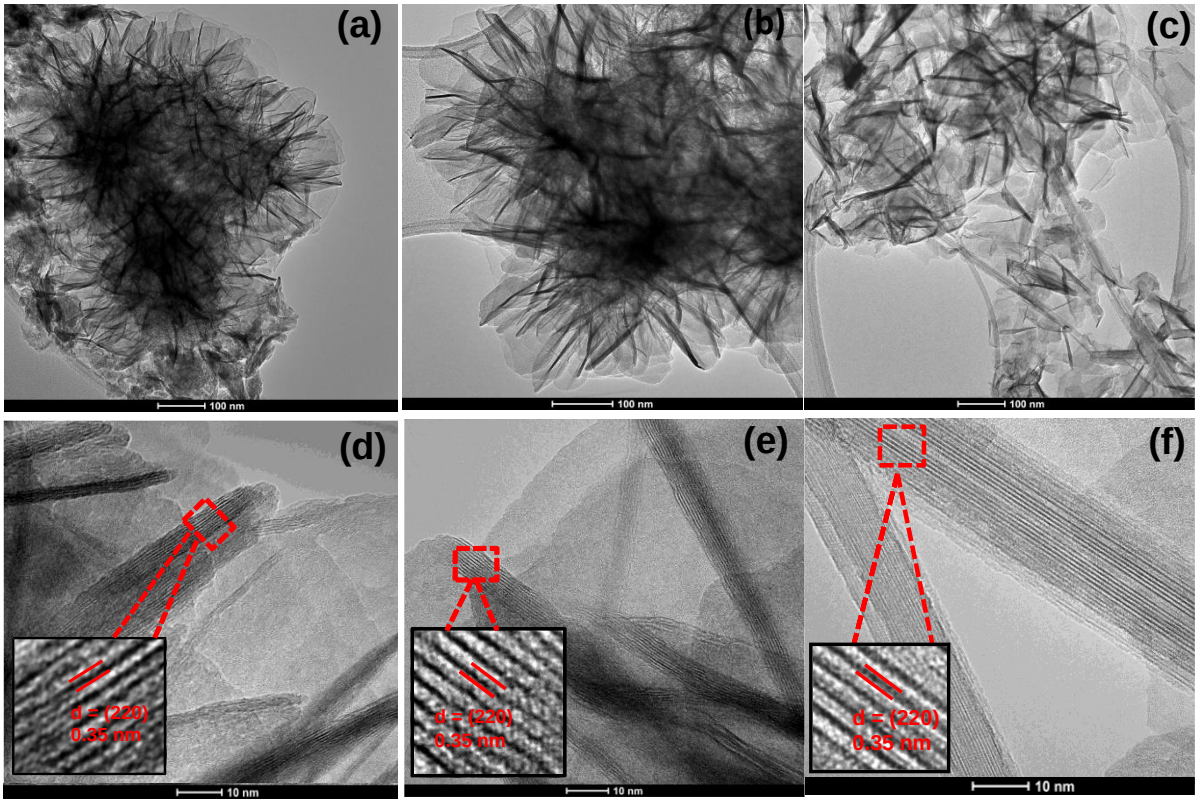

Figure 3.1. TEM and HR-TEM images with an inset image of a specific d-spacing value of (a, d) Mn NF, (b, e) Mn NF + NR, and (c, f) Mn NR.

The crystal phase identification of MnO_2 nanostructures prepared at various reaction times was characterized by XRD analysis. The existence of a broad peak showed that the synthesized nanomaterials contain both amorphous as well as crystalline phases. Figure 3.2(a) displays that the crystallinity of the MnO_2 nanostructure increased with the increment in the reaction time from 2 to 18 h, that is, from NF to NR. The MnO_2 nanostructure prepared at 2 h (Mn NF), 10 h (Mn NF + NR), and 18 h (Mn NR) showed diffraction peaks at 2θ ~13°, ~26°, ~38°, and ~65° related to the (110), (220), (211), and (002) lattice planes, respectively. It

showed similarity to those of α-MnO_2 (ICDD-JCPDS no. 04−0141) with a tetragonal unit cell having lattice parameters of a = b = 9.78 Å and c = 2.86 Å.[11] It was observed that upon increasing the reaction time, the crystalline nature of the nanostructure enhances from Mn NF to Mn NR with the appearance of sharper and narrower peaks. The energy-dispersive X-ray spectroscopy (EDX) study also confirms the formation of the pure MnO_2 nanostructure without any impurities as revealed in Figure 3.2(b).

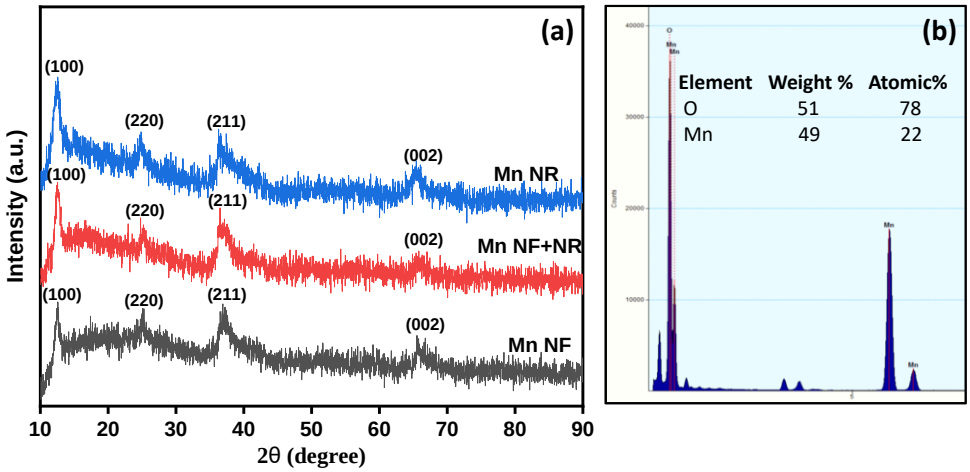

Figure 3.2. (a) XRD pattern of different MnO_2 nanostructures and (b) EDX spectra of MnO_2 NFs.

Table 3.1: Specific surface area, total pore volume, and mean pore diameter of different shapes of MnO_2 nanostructures.

Sample	Specific surface area (m^2g^{-1})	Total pore volume (cm^3g^{-1})	Mean pore diameter (nm)
Mn NF	69	0.374	20.05
Mn NF+NR	53	0.340	28.17
Mn NR	23	0.139	24.00

Figure 3.3(a) shows BET N_2 adsorption-desorption curves for the different shapes of the MnO_2 nanostructure (Mn NF, Mn NF + NR, and Mn NR), and these curves showed the Type IV adsorption isotherm that indicates the mesoporous nature. The specific surface areas of each shape of the MnO_2 nanostructure, that is, Mn NF, Mn NF + NR, and Mn NR, were observed as 69, 53, and 23 m^2g^{-1}, respectively. The specific surface areas, total pore volumes, and mean pore diameters of different shapes of MnO_2 nanostructures are mentioned in Table 3.1. Mn NF showed the maximum specific surface area consist of many active sites present on its surface and provides a high charge-transfer rate.

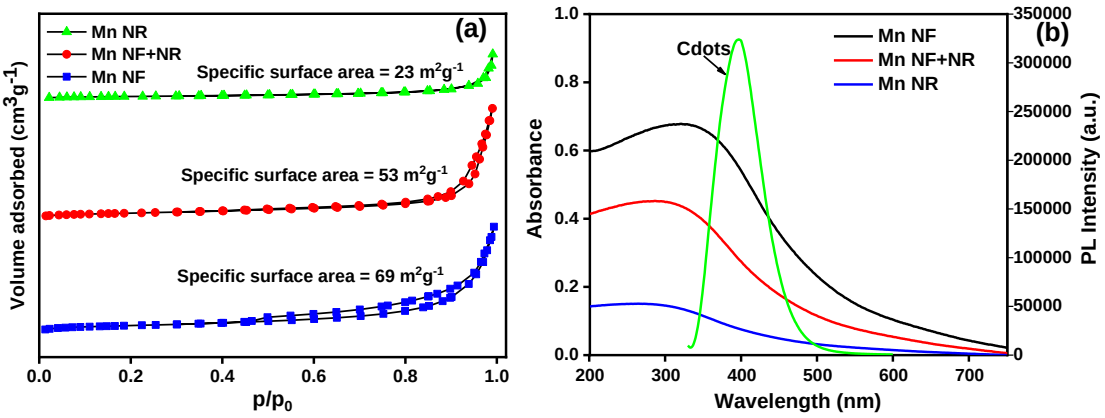

Figure 3.3. (a) BET N_2 adsorption−desorption isotherms of different MnO_2 nanostructures and (b) Spectral overlap between the UV−vis absorption spectra of different MnO_2 nanostructures and the emission spectra of Cdots.

3.3.2 Optical properties

The optical properties of Cdots and MnO_2 nanostructures were investigated by their UV−vis absorption spectra. It was already reported that Cdots show a sharp peak of absorption at 263 nm, which corresponds to n−π* and π−π* transitions due to C=O and the conjugated C=C band, respectively in Chapter 2. Figure 3.3(b) reveals the UV−vis absorption spectra of Mn NF, Mn NF + NR, and Mn NR in which a broad peak ranging from 250 to 500 nm overlaps with the emission spectrum of Cdots. This result confirms that the FRET mechanism occurs between electron-donor Cdots and different morphologies of the electron-acceptor MnO_2 nanostructure. It was also found that the overlap region of the Cdot-MnO_2 nanostructure becomes maximum in the Mn-NF shape and minimum in the Mn-NR shape. From this result, it can be concluded that different shapes of the MnO_2 nanostructure have a different role in the FRET mechanism between Cdots and the MnO_2 nanostructure. The spectral overlap integral [J(λ)] values among Cdots and MnO_2 nanostructures were evaluated by using equation (1.8). It was observed from the values of J(λ) and also from Figure 3.3(b) that the variation in the shape of the MnO_2 nanostructure from Mn NF to Mn NR leads to a decrease in the spectral overlap integral.

3.3.3 Fluorescence quenching of Cdots by different MnO_2 nanostructures

The FRET mechanism of the Cdot-MnO_2 nanostructure was also confirmed by the fluorescence quenching study.[12,13] The prepared Cdots showed high fluorescence intensity, which was effectively quenched in the presence of different morphologies of the MnO_2 nanostructure. The level of quenching of the Cdots was different in the presence of different

morphologies of the MnO_2 nanostructure. The mechanism of fluorescence quenching of Cdots is based on holes and electrons which get trapped in Cdots and the MnO_2 nanostructure and result in low availability used for radiative recombination.[14] The different concentrations of the MnO_2 nanostructure were varied from 0.912 to 6.384 mM for investigating the fluorescence quenching of Cdots. It was observed that the PL intensity of Cdots was reduced by different MnO_2 nanostructures up to a 6.384 mM concentration, as revealed in Figures 3.4(a), (b), and (c). To figure out the level of quenching efficiency by different shapes of quenchers [Q], the graph of F_0/F against the [Q] was plotted based on the resulting Stern-Volmer equation (1.4). The plot of F_0/F against the [Q], that is, Mn NF, Mn NF + NR, and Mn NR, is shown in Figures 3.4(d), (e), and (f), respectively. From the slope values of these plots, the K_{SV} value have been evaluated of the respective shape of the MnO_2 nanostructure. Cdots show two different K_{SV} values, which are 423 and 5829 M^{-1}, respectively, at lower- and higher-concentration regions of Mn NF as a quencher. In the case of Mn NF + NR and Mn NR, the K_{SV} values were estimated as 656 and 264 M^{-1}, respectively. Therefore, the extent of quenching efficiency of Cdots follows the order of Mn NF > Mn NF + NR > Mn NR.

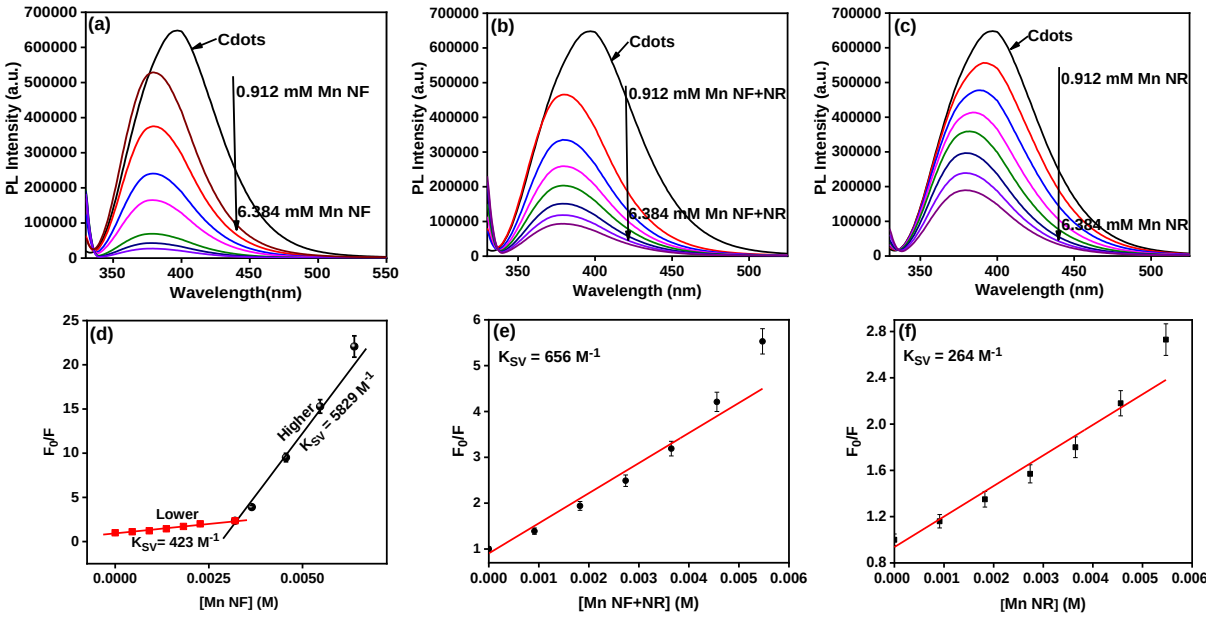

Figure 3.4. Fluorescence quenching spectra of Cdots with different concentrations of (a) Mn NF, (b) Mn NF+NR, and (c) Mn NR, and Stern−Volmer quenching plot of different MnO_2 nanostructures i.e., (d) Mn NF, (e) Mn NF+NR, and (f) Mn NR with Cdots.

It can be seen in Figure 3.5(a) that Mn NF showed a significant increment in F_0/F value as the concentration of Q increases as compared to the other shapes, that is, Mn NF + NR and Mn NR. Mn NF has a larger specific surface area (69 m^2g^{-1}) as well as a high pore volume (0.374

cm^3g^{-1}) compared to other shapes of the MnO_2 nanostructure (23 and 53 m^2g^{-1}) represented in Figure 3.3(a) and Table 3.1. The normal open structure of Mn NF reduces the transport distance between electrons and cations, and they showed the maximum quenching because of having a huge surface area and a reduced amount of charge-transfer resistance.[7] Therefore, it can be said that the variation in the specific surface area and pore structure of MnO_2 shows a vital role and significantly alters the variation of electron transfer rate in the ES of Cdots. On the other hand, it can also demonstrate that the electron transfer rate from Cdots (electron donor) to the MnO_2 nanostructure (electron acceptor) gradually decreases as the shape changes from Mn NF to Mn NR.

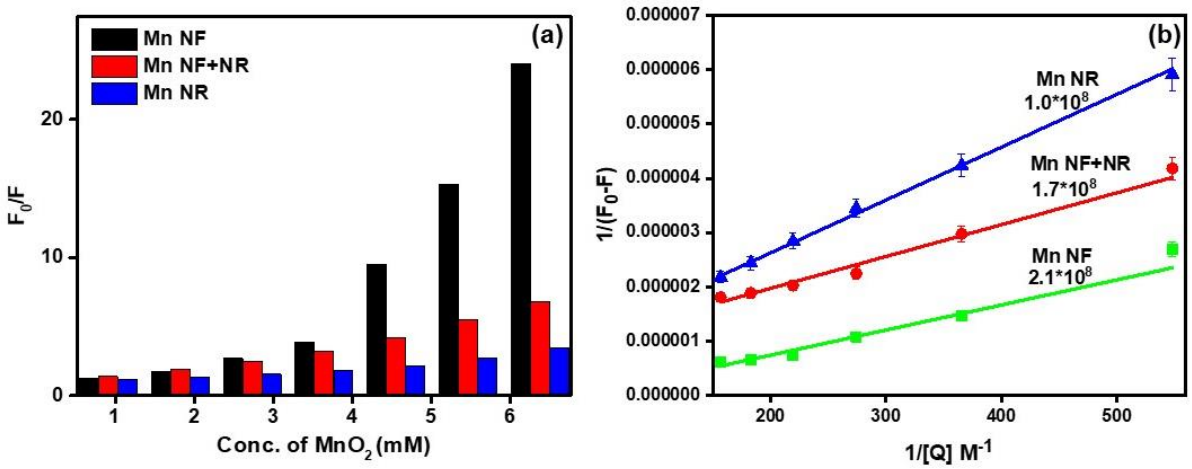

Figure 3.5. (a) Bar graph of fluorescence quenching efficiency of different shapes of the MnO_2 nanostructure at various concentrations, and (b) B−H binding plot of different MnO_2 nanostructures with Cdots.

Further, to comprehend the nature of stoichiometry and interaction among Cdots and various shapes of MnO_2 nanostructures, the excited-state binding constant values have been estimated by using their respective fluorescence intensity data using the 1:1 linear Benesi−Hildebrand equation (1.5). The plot between ($1/F_0 - F$) and 1/[Q] gives a straight line for all shapes of the MnO_2 nanostructure (Figure 3.5(b)). From this plot, the binding constant values (K) of Cdots have been estimated, which are 2.1×10^8, 1.7×10^8, and 1×10^8 M^{-1} in the presence of Mn NF, Mn NF + NR, and Mn NR, respectively. From these data, the binding constant values were observed to be gradually decrease as the shape of the MnO_2 nanostructure changes from Mn NF to Mn NR. Therefore, it can be demonstrated that the variation in the shape of the MnO_2 nanostructure had an impact on their interaction or electron transfer with Cdots, which results in deviation in the value of the binding constant of Cdots. Mn NF showed the maximum value of binding constant for Cdots due to large quantity of active sites on its

surface (due to a high surface area) as compared to other shapes of MnO_2 nanostructures. It can be demonstrated that electrons get transferred easily from Cdots (donor) to Mn NF (acceptor) as compared to the other two shapes.

3.3.4 Restoration mechanism of Cdots and detection of GSH

The addition of GSH in MnO_2 nanostructures with different morphologies, that is, Mn NF, Mn NF + NR, and Mn NR, leads to recovery of fluorescence (turn-on) of Cdots which was observed in Figures 3.6(a), (b) and (c), respectively. The restoration of fluorescence of Cdots depends upon the redox reaction among the MnO_2 nanostructure and GSH as discussed in Chapter 2 (equation (2.1)). In the above reaction, MnO_2 gets converted to Mn^{2+} in the presence of GSH and itself gets oxidized to GSH disulfide (GSSG).[15]

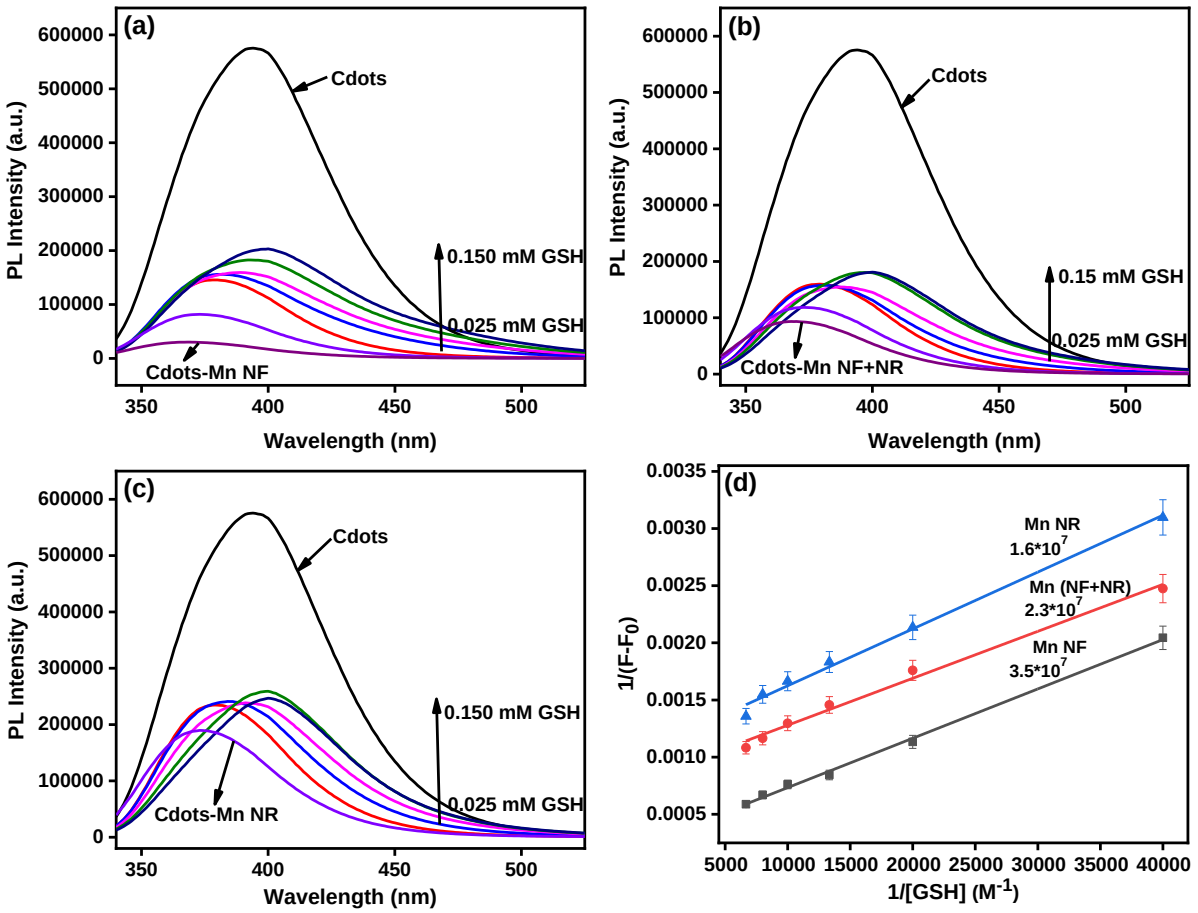

Figure 3.6. Fluorescence recovery of the Cdots with the successive addition of 50 µL of GSH (1 mM) in (a) Cdots-Mn NF, (b) Cdots-Mn NF+NR, and (c) Cdots-Mn NR sensing probes, and (d) B−H binding plot of Mn NF, Mn NF + NR, and Mn NR with GSH.

This results in the exclusion of Cdots from the huge surface of the MnO_2 nanostructure and leads to the recovery of fluorescence of Cdots. Cdots, MnO_2 nanostructures, and GSH play

a significant role as a fluorometric reporter, quencher, and detector in this prepared sensing probe. The prepared Cdot-MnO_2 nanocomposites were used as sensing nanoprobes for GSH detection in which different concentrations of GSH were mixed with specific concentrations (6.384 mM) of different shapes of the MnO_2 nanostructure (Mn NF, Mn NF + NR, and Mn NR). It was determined that the fluorescence intensity of the Cdot-MnO_2 nanostructure enhances with the increase in the concentration of GSH. The binding constant values of the Cdot-MnO_2 nanostructure with the addition of GSH were evaluated through the Benesi−Hildebrand method (1.5). It has been observed that the addition of GSH considerably changes the values of binding constant for Cdots, which are 3.5×10^7, 2.3×10^7, and 1.6×10^7 M^{-1} in the case of Mn NF, Mn NF + NR, and Mn NR, respectively (Figure 3.6(d)). The decrease in the values of binding constants of Cdots in the presence of GSH confirmed the elimination of Cdots from the surface of MnO_2 nanostructures in the order of Mn NF > Mn NF + NR > Mn NR. The fluorescence intensity of Cdots gets more recovered with the addition of GSH in the case of Mn NF as compared to other shapes of the MnO_2 nanostructure, probably because of the larger specific surface area and mesoporous nature of Mn NF. The variation in the shape of the MnO_2 nanostructure in the developed sensing nanoprobe affects the restoration (turn-on) of fluorescence of Cdots.

The fluorescence studies were performed with different amino acids to interpret that the developed sensing platform is selective for GSH. A particular concentration of different amino acids such as Asp, Arg, AA, glutamine (Gln), Gly, Cys, glutamic acid (Glu), His, Leu, Met, GSH, and other biomolecules like glucose and sucrose was mixed with Cdot-MnO_2 systems. It found that GSH showed a significant response as compared to other species (Figure 3.7(a)). It showed that different shapes of Cdot-MnO_2 nanostructures showed extreme selectivity and sensitivity for the GSH sensing. A fine linear range of the plot between $(F-F_0/F_0)$ and [GSH] was found for all three different shapes of the MnO_2 nanostructure in which F_0 and F are represented as the PL intensities without and with the presence of GSH, respectively. It was found that Mn NF, Mn NF + NR, and Mn NR corresponded to distinct values of the limit of detection (LOD), that is, 19, 23, and 42 μM, respectively (Figures 3.7(b), (c) and (d)). It was observed the best LOD value for Mn NF in comparison with Mn NF + NR and Mn NR. Table 1.1 lists the LOD values for the detection of GSH by using different sensing platforms and techniques reported in the literature. These studies showed that the prepared sensing platform and technique are simple, cheap, and green as compared to other expensive sensing platforms and different techniques.

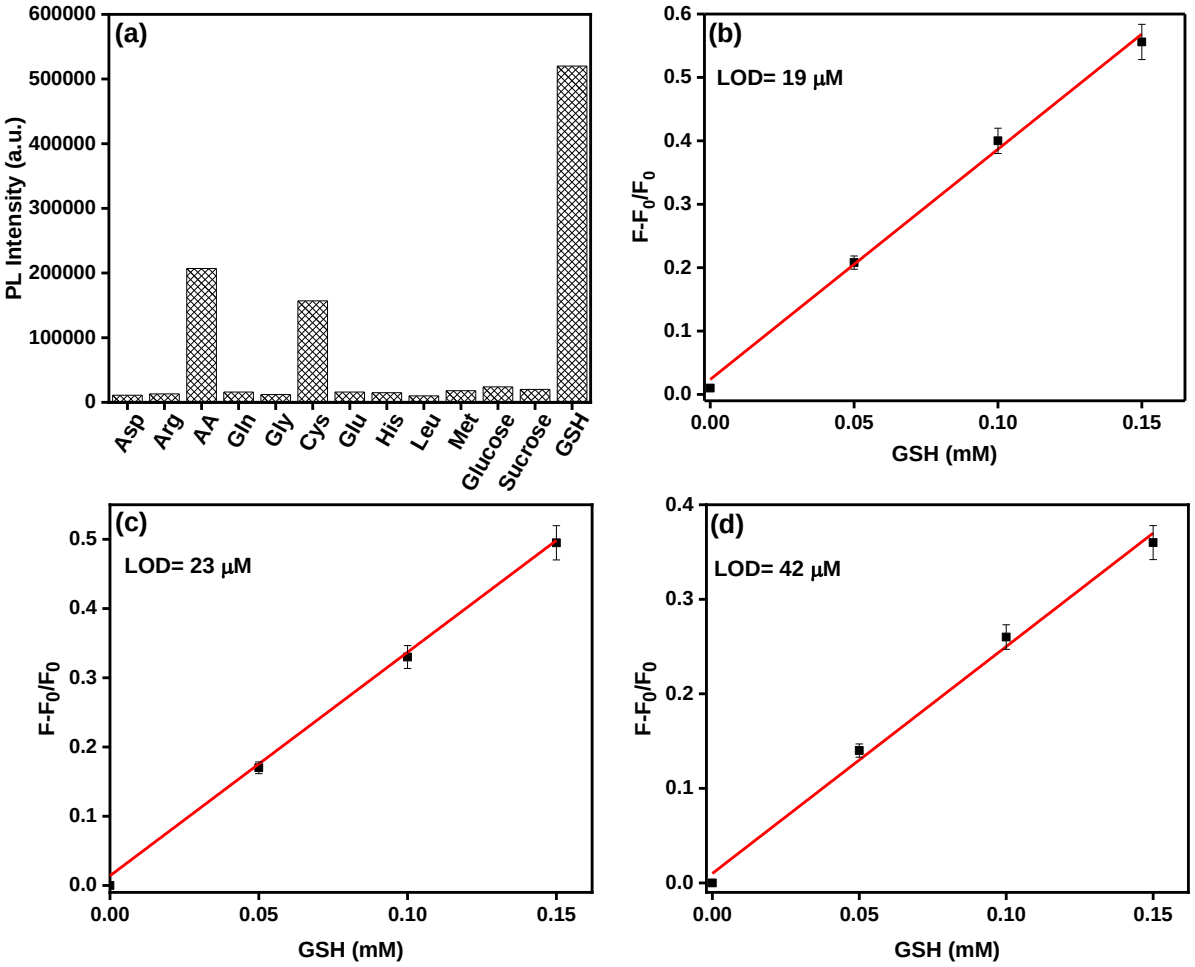

Figure 3.7. (a) Fluorescence response of the Cdot-MnO_2 nanostructure as a sensing system toward different species and Fluorescence responses of the $[(F - F_0)/F_0]$ vs GSH concentration for (b) Cdot-Mn NF, (c) Cdot-Mn NF+NR, and (d) Cdot-Mn NR systems.

3.3.5 Fluorescence quantum yield measurements

The values of ϕ of Cdots with various systems were evaluated by using equation 1.2 and are tabulated in Table 3.2. It was found that the values of ϕ for Cdots are considerably quenched with the addition of specific concentrations of different shapes of the MnO_2 nanostructure. The fluorescence quantum yields of Cdots are quenched ~9.7, ~6.8, and ~2.7 times in the presence of Mn NF, Mn NF + NR, and Mn NR, respectively. As a result, the extent of ϕ value of Cdots follows the trend of Mn NF > Mn NF + NR > Mn NR. The values of ϕ of different shapes of the Cdot-MnO_2 nanostructure with the addition of GSH was evaluated (Table 3.2). For different shapes of the MnO_2 nanostructure, the ϕ restorations of Cdots with the specific amount of GSH are ~5 (Mn− NF), ~3 (Mn−NF + NR), and ~1.3 (Mn-NR) times. The recovery of fluorescence of Cdots follows the trend of Mn NF > Mn NF + NR > Mn NR. This result clarified that the change in the shapes of the MnO_2 nanostructure from Mn NF to Mn NR in the Cdot-MnO_2 nanoprobe results in less efficient elimination of Cdots from the

surface of MnO_2. Hence, a strong redox reaction takes place among Mn NF and GSH as compared to other shapes.

Table 3.2. Photophysical parameters of Cdots with different shapes of MnO_2 nanostructures and GSH.[c]

Systems	$\boldsymbol{\Phi}$	$\boldsymbol{\tau_{av}}$ **(ns)**	$\boldsymbol{k_r}$ **(10^9 s^{-1})**	$\mathbf{k_{nr}}$ **(10^9 s^{-1})**	$\boldsymbol{k_{ET}}$ **(10^9 s^{-1})**	$\boldsymbol{\Phi_{EET}}$ $\boldsymbol{(\tau_D)}$	$\boldsymbol{\Phi_{EET}}$ $\boldsymbol{(\Phi_D)}$
Cdots	0.68	4.40	0.15	0.07	-	-	-
Cdots+ Mn NF	0.07	1.26	0.04	0.74	0.57	0.71	0.89
Cdots+ Mn NF+GSH	0.35	3.85	0.09	0.16	0.03	0.12	0.49
Cdots+ Mn (NF+NR)	0.10	2.33	0.05	0.38	0.20	0.47	0.85
Cdots+ Mn (NF+NR) + GSH	0.30	3.76	0.08	0.19	0.04	0.14	0.56
Cdots+ Mn NR	0.25	3.55	0.07	0.21	0.06	0.19	0.63
Cdots+ Mn NR+GSH	0.33	3.86	0.09	0.17	0.03	0.12	0.52

[c]Experimental error ±5 %

3.3.6 Time-resolved emission studies

To get more insight into the interaction of different shapes of the Cdot-MnO_2 nanostructure and their impact on the detection of GSH, the fluorescence time-resolved emission studies were performed for the respective samples at λ_{ex} = 340 nm with their respective emission wavelengths. An average lifetime (τ_{av}) value of prepared Cdots is 4.40 ns, and the addition of a specific concentration of different shapes of the MnO_2 nanostructure leads to significant variation in quenching of the values of lifetime decay of Cdots (Figure 3.8). From Table 3.2, it was found that the average lifetime values of Cdots were quenched 71, 47, and 19% in the presence of Mn NF, Mn NF + NR, and Mn NR, respectively. From this analysis, it is confirmed that Cdots show maximum quenching in the presence of Mn NF while minimum in Mn NR. Astonishingly, in the presence of GSH as a sensing agent, the average lifetime values of different shapes of the Cdot-MnO_2 nanostructure showed an increment of their respective lifetime values. This result confirms that Cdots exhibited recovery of PL with the particular amount of GSH. The increment of the lifetime of Cdots in the presence of GSH is solely depends upon the different morphologies of MnO_2 nanostructure. The fluorescence restorations of Cdots in the presence of GSH were found to be 67, 38, and 8% for Mn NF, Mn NF + NR, and Mn NR, respectively.

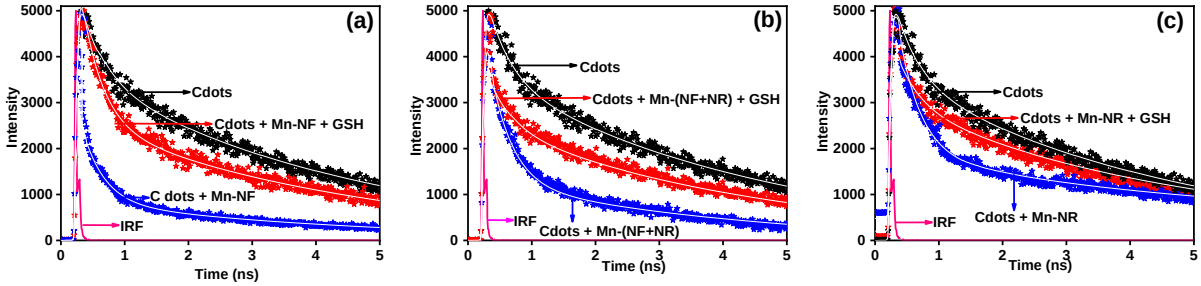

Figure 3.8. Fluorescence lifetime decays of Cdots in (a) Mn NF, (b) Mn (NF + NR), and (c) Mn NR and in the presence of GSH.

The k_r and k_{nr} rate constant values were further estimated via equations 1.2 and 1.3. The k_r and k_{nr} values are tabulated in Table 3.2. It was found that the k_{nr} values of Cdots get increased by 10.5, 5.4, and 3 times, whereas the values of k_r decreased by 0.26, 0.33, and 0.46 times, respectively, in the existence of Mn NF, Mn NF + NR, and Mn NR. The decrease of k_r values and the increase of k_{nr} values of Cdots confirm that Cdots get less fluorescence in the presence of different shapes of the MnO_2 nanostructure (maximum for Mn-NF and minimum for Mn-NR). Further, it was found that the presence of GSH to the Cdot-MnO_2 system considerably increases k_r values and decreases k_{nr} values, which confirms that GSH has the propensity to drive out Cdots from different shapes of the MnO_2 nanostructure. Finally, it was observed fluorescence restoration (turn-on), which implies that Cdots get more fluorescence in GSH. To rationalize the clear idea on excited-state dynamics of Cdots, the k_{ET} in the presence of MnO_2 nanostructures with different morphologies and also in the presence of GSH were calculated by using equation (1.6). The electron-transfer rate considerably changes with the variation in shapes of the MnO_2 nanostructure. From Table 3.2, it was found that the electron-transfer rate from electron-donor Cdots to different shapes of the electron-acceptor MnO_2 nanostructure followed the order of Mn NF > Mn NF + NR > Mn NR. This result confirms that the electron-transfer process of Cdots solely depends on the shape of the MnO_2 nanostructure. Moreover, the existence of GSH results as interruption of the electron-transfer process of Cdots as GSH shows redox reaction with the MnO_2 nanostructure. This results as release of Cdots from the surface of the MnO_2 nanostructure. The values of ϕ_{EET} are estimated by the equation 1.7. The calculated values of EET (Table 3.2) by using both the values of quantum yield [ϕ_{EET} (ϕ_D)] and lifetime [ϕ_{EET} (τ_D)] also signify that the electron-transfer efficiency for Cdots considerably changes and depends on the shapes of the MnO_2 nanostructure, which follows the order of Mn NF > Mn NF + NR > Mn NR. Moreover, the presence of GSH diminishes [ϕ_{EET} (ϕ_D)] and [ϕ_{EET} (τ_D)] values of Cdots, which approves that the presence of GSH results as

exclusion of Cdots from the MnO_2 nanostructure's surface. The FRET efficiency (E) of Cdots with the addition of MnO_2 nanostructures were estimated by using the equation 1.9. It was found from Table 3.3 that "E" of Cdots exclusively depends on the variant shapes of the MnO_2 nanostructure, which follows the order of Mn NF > Mn NF + NR > Mn NR. This result confirms that the FRET mechanism of Cdots is more pronounced in Mn NF as compared to other shapes. Furthermore, the R_0 between Cdots and different shapes of MnO_2 nanostructures were determined through the equation (1.10). The relative orientation factor is denoted by κ^2 for the transition dipoles of the electron donor and the electron acceptor in isotropic solution. The other parameters "η", "ϕ", and "J(λ)" are represented as the viscosity of the medium, the fluorescence quantum yield of the donor (Cdots), and the spectral overlap integral, respectively.

Table 3.3. Förster distance, efficiency percentage, and separation distance of different Cdots-MnO_2 systems.[d]

Systems	R_0 (Å)	E (%)	r (nm)
Cdots			-
Cdots + Mn NF	4.97	42	1.53
Cdots + Mn NF+NR	8.50	32	2.95
Cdots + Mn NR	12.52	18	6.14

[d]Experimental error ±5 %

The calculated R_0 values are tabulated in Table 3.3, which approves that the interaction among Cdots and different morphologies of the nanostructure fulfills the classical FRET theory.[16] Further, the separation distance (r) between the MnO_2 nanostructures and Cdots were also calculated by using the equation (1.11). The "r" between the different shapes of the MnO_2 nanostructure and Cdots steadily increases with the variation in the shape of the MnO_2 nanostructure from Mn NF to Mn NR (1.53, 2.95, and 6.14 nm for Mn NF, Mn NF + NR, and Mn NR, respectively). Mn NF has the shortest separation distance with Cdots as compared to other shapes, which confirms that the Mn NF has the maximum FRET efficiency.

Conclusion

In this Chapter, the role of different morphology (shape) of MnO_2 nanostructure in the fluorescent sensing system based on Cdots-MnO_2 nanostructure for GSH sensing was studied in detail. The specific surface area of different MnO_2 structures is determined by BET and follows the order Mn NF> Mn NF+NR> Mn NR. Mn NF showed maximum fluorescence

quenching of Cdots and a higher value of K_{SV} owing high specific surface area and high k_{ET} values. There was a decrease in the values of Φ and τ_{av} (ns) which confirms the occurrence of FRET mechanism from Cdots (electron-donor) to Mn NF (electron-acceptor). The decrease in k_r and increase in k_{nr} rate constants showed that the Cdots get less fluorescence in presence of different shapes of MnO_2 nanostructure (maximum for Mn NF and minimum for Mn NR). The prepared sensing systems showed fluorescence recovery of Cdots due to the occurrence of redox reaction between GSH and MnO_2 which results in the conversion of MnO_2 to Mn^{2+}. The highest limit of detection (19 μM) for GSH was observed in the case of Cdot-Mn NF sensing systems. Hence, the variation in the morphology of MnO_2 nanostructure in the developed sensing system put a great impact on the sensing of GSH.

References

(1) Shetti, N. P.; Mishra, A.; Basu, S.; Mascarenhas, R. J.; Kakarla, R. R.; Aminabhavi, T. M. Skin-Patchable Electrodes for Biosensor Applications: A Review. *ACS Biomater. Sci. Eng.* **2020**, *6* (4), 1823–1835. https://doi.org/10.1021/acsbiomaterials.9b01659.

(2) Dakshayini, B. S.; Reddy, K. R.; Mishra, A.; Shetti, N. P.; Malode, S. J.; Basu, S.; Naveen, S.; Raghu, A. V. Role of Conducting Polymer and Metal Oxide-Based Hybrids for Applications in Ampereometric Sensors and Biosensors. *Microchem. J.* **2019**, *147*, 7–24. https://doi.org/10.1016/j.microc.2019.02.061.

(3) Bukkitgar, S. D.; Shetti, N. P.; Kulkarni, R. M.; Nandibewoor, S. T. Electro-Sensing Base for Mefenamic Acid on a 5% Barium-Doped Zinc Oxide Nanoparticle Modified Electrode and Its Analytical Application. *RSC Adv.* **2015**, *5* (127), 104891–104899. https://doi.org/10.1039/C5RA22581G.

(4) Bukkitgar, S. D.; Kumar, S.; Pratibha; Singh, S.; Singh, V.; Raghava Reddy, K.; Sadhu, V.; Bagihalli, G. B.; Shetti, N. P.; Venkata Reddy, C.; Ravindranadh, K.; Naveen, S. Functional Nanostructured Metal Oxides and Its Hybrid Electrodes–Recent Advancements in Electrochemical Biosensing Applications. *Microchem. J.* **2020**, *159*, 105522. https://doi.org/10.1016/j.microc.2020.105522.

(5) Rathi, A.; Basu, S.; Barman, S. Adsorptive Removal of Fipronil from Its Aqueous Solution by Modified Zeolite HZSM-5: Equilibrium, Kinetic and Thermodynamic Study. *J. Mol. Liq.* **2019**, *283*, 867–878. https://doi.org/10.1016/j.molliq.2019.02.140.

(6) Wang, Y.; Yin, H.; Li, X.; Waterhouse, G. I. N.; Ai, S. Photoelectrochemical

Immunosensor for N6-Methyladenine Detection Based on Ru@UiO-66, Bi_2O_3 and Black TiO_2. *Biosens. Bioelectron.* **2019**, *131*, 163–170. https://doi.org/10.1016/j.bios.2019.01.064.

(7) Sohal, N.; Maity, B.; Shetti, N. P.; Basu, S. Biosensors Based on MnO_2 Nanostructures: A Review. *ACS Appl. Nano Mater.* **2021**, *4* (3), 2285–2302. https://doi.org/10.1021/acsanm.0c03380.

(8) Li, Q.; Xia, Y.; Wan, X.; Yang, S.; Cai, Z.; Ye, Y.; Li, G. Morphology-Dependent MnO_2/Nitrogen-Doped Graphene Nanocomposites for Simultaneous Detection of Trace Dopamine and Uric Acid. *Mater. Sci. Eng. C* **2020**, *109*, 110615. https://doi.org/10.1016/j.msec.2019.110615.

(9) Çakıroğlu, B.; Demirci, Y. C.; Gökgöz, E.; Özacar, M. A Photoelectrochemical Glucose and Lactose Biosensor Consisting of Gold Nanoparticles, MnO_2 and g-C_3N_4 Decorated TiO_2. *Sensors Actuators B Chem.* **2019**, *282*, 282–289. https://doi.org/10.1016/j.snb.2018.11.064.

(10) Yuan, H.; Deng, L.; Qi, Y.; Kobayashi, N.; Hasatani, M. Morphology-Dependent Performance of Nanostructured MnO_2 as an Oxygen Reduction Catalyst in Microbial Fuel Cells. *Int. J. Electrochem. Sci.* **2014**, *10* (5), 3693–3706.

(11) Su, D.; Ahn, H.-J.; Wang, G. Hydrothermal Synthesis of α-MnO_2 and β-MnO_2 Nanorods as High Capacity Cathode Materials for Sodium Ion Batteries. *J. Mater. Chem. A* **2013**, *1* (15), 4845. https://doi.org/10.1039/c3ta00031a.

(12) Wang, Y.; Jiang, K.; Zhu, J.; Zhang, L.; Lin, H. A FRET-Based Carbon Dot-MnO_2 Nanosheet Architecture for Glutathione Sensing in Human Whole Blood Samples. *Chem. Commun.* **2015**. https://doi.org/10.1039/c5cc04905a.

(13) He, D.; Yang, X.; He, X.; Wang, K.; Yang, X.; He, X.; Zou, Z. A Sensitive Turn-on Fluorescent Probe for Intracellular Imaging of Glutathione Using Single-Layer MnO_2 Nanosheet-Quenched Fluorescent Carbon Quantum Dots. *Chem. Commun.* **2015**, *51* (79), 14764–14767. https://doi.org/10.1039/c5cc05416h.

(14) Mehta, A.; Mishra, A.; Kainth, S.; Basu, S. Carbon Quantum Dots/TiO_2 Nanocomposite for Sensing of Toxic Metals and Photodetoxification of Dyes with Kill Waste by Waste Concept. *Mater. Des.* **2018**, *155*, 485–493.

https://doi.org/10.1016/j.matdes.2018.06.015.

(15) Gao, W.; Liu, Z.; Qi, L.; Lai, J.; Kitte, S. A.; Xu, G. Ultrasensitive Glutathione Detection Based on Lucigenin Cathodic Electrochemiluminescence in the Presence of MnO_2 Nanosheets. *Anal. Chem.* **2016**, *88* (15), 7654–7659. https://doi.org/https://doi.org/10.1016/j.saa.2019.117626.

(16) Lakowicz, J. R. *Principles of Fluorescence Spectroscopy*; Lakowicz, J. R., Ed.; Springer US: Boston, MA, 2006. https://doi.org/10.1007/978-0-387-46312-4.

CHAPTER-4

Deciphering the Mechanism of Inner Filter Effect on Heteroatom Doped Carbon dots-MnO_2 Nanoprobe for Selective Detection of Glutathione

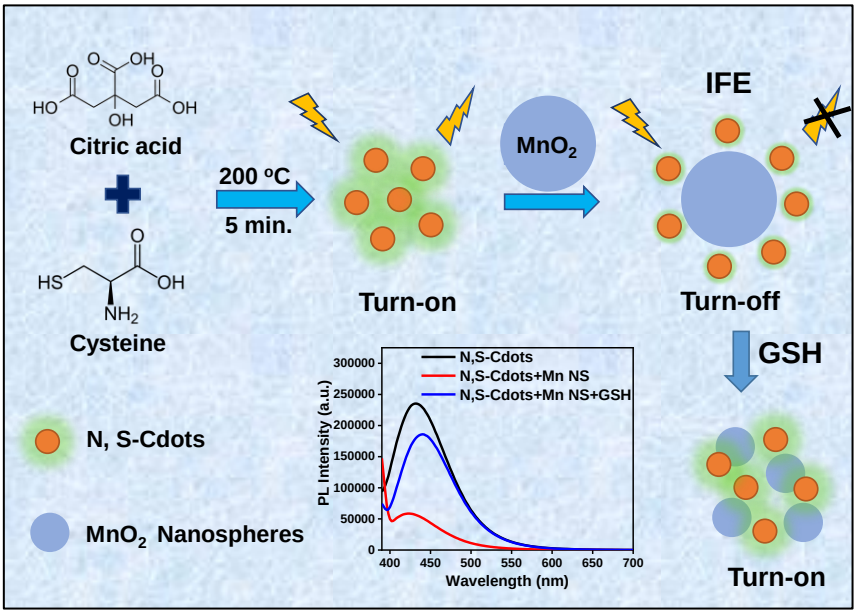

Highlights

- Improvement of the electronic and optical properties of Cdots by doping with different heteroatoms.
- To investigate the role of heteroatom doping in Cdots@MnO_2 nanosensors.
- N, S-Cdots-MnO_2 nanospheres showed best nanosensor in terms of different photophysical investigations.
- Confirmation of fluorescence quenching between Cdots@MnO_2 nanosensor by inner filter effect mechanism.
- Study the fluorescence restoration of N, S-Cdots-MnO_2 nanospheres for GSH with best detection limit of 80 nM.

4.1 Introduction

Cdots are highly attractive fluorescent nanomaterials in recent years as compared to other conventional fluorescent materials due to having exclusive optical properties.[1–3] The post-surface functionalization and intrinsic heteroatom doping are mainly two effective approaches to improving the properties of Cdots by tuning their band gap.[4,5] Nowadays, heteroatom doping has become a highly efficient method to obtain coupling between optical and electronic features of Cdots.[6] The nitrogen and carbon atoms have a nearly similar size which results in effective nitrogen doping along with high quantum yield.[7] Doping of nitrogen into the structure of Cdots makes them electron-donor by modifying their electronic structure.[8] While doping of sulfur offers emissive traps to the photoexcited electrons which lead to modification of the fluorescence towards a higher wavelength.[9] According to the diagonal rule, sulfur shows some similar properties to the nitrogen atoms which is further considered a feasible doping atom with nitrogen atoms.[10] Doping or co-doping provides large active sites and the synergistic effect between individual elements which leads to radiative recombination of trapped electron-holes pairs.[11] Recently, many researchers are focused on N, S- doping due to its attractive properties. Cdots are mostly employed as fluorescence sensors for detecting specific molecules. These applications are dependent on the interactions between analytes and Cdots.[12] Therefore, the functional groups or heteroatoms located on the surface of Cdots significantly affect the aforesaid interactions and also enhance its applications as a sensor.

Nowadays, sensing platforms based on the combination of fluorescent probes and nanomaterials are highly used for the ultrasensitive detection of GSH. Li et al.[13] prepared a sensing platform consisting of N, S-doped Cdots, and gold nanoparticles (AuNPs) for GSH sensing. They found that the N, S-doped Cdots increase the sensitivity of the prepared sensor 10 times as compared to N-doped Cdots. In comparison with N-doped Cdots, the N, S-doped Cdots showed high energy transfer efficiency due to their easy accumulation on the surface of AuNPs which further resulted in compact N, S- doped Cdots shell. Among various transition metal oxides, MnO_2 is considered an active material in sensors for detecting multiple biomolecules due to its extraordinary physical and chemical properties.[14] The broad absorption spectra for MnO_2 nanoparticles depicts the huge spectral overlapping in excitation/emission spectra of different fluorescence materials for occurrence of IFE.[15] The fluorescence quenching mechanism of carbon dots in the presence of MnO_2 could be due to the IFE.[16] The precise

quenching mechanism of carbon dots caused by transfer of electrons in the ES is confirmed by investigating the lifetime studies.[17]

In this study, the heteroatom doping of Cdots with different elements like nitrogen and sulfur has been carried out. The synthesis of N, S-Cdots by using CA (as carbon source), and Cys (as nitrogen and sulfur source) was done at high-temperature treatment i.e., 200^{o} C for 5 min. N, S-Cdots-MnO_2 nanospheres (NS) act as a sensor for sensing selective GSH. The introduction of nitrogen and sulfur atoms in the structure of Cdots was confirmed from IR spectrum, XPS spectra, and elemental mapping. The shape and size of Cdots and MnO_2 NS were examined by TEM. The maximum quenching efficiency of N, S-Cdots was evaluated by the introduction of MnO_2 NS. Further, the recovery of N, S-Cdots-MnO_2 NS was investigated by adding GSH. The PL quenching of N, S-Cdots accompanied by MnO_2 NS occurs due to IFE. The restoration of fluorescence of Cdots was based on a redox reaction among the MnO_2 and GSH. Similarly, other three different types of Cdots i.e., undoped Cdots (U-Cdots), N-doped Cdots (N-Cdots), and S-doped Cdots (S-Cdots) by using CA only, CA with glycine, CA with thioacetic acid, and CA with cysteine, respectively were synthesized by the same method.

4.2 Experimental section

4.2.1 Materials and reagents

L-methionine (99%), as well as potassium permanganate ($KMnO_4$) (99%) were bought from Loba Chemie, India, and a fixed ratio of both was used to prepare MnO_2 NS soluble in the aqueous medium. Citric acid, cysteine, thioacetic acid, and glycine with 99% purity were bought from Loba Chemie, India, and were further used for the synthesis of different types of Cdots. Ultrapure distilled water was prepared through a double distillation unit and which was further used for preparing the solutions.

4.2.2 Synthesis of heteroatom doped Cdots

Four different types of Cdots were prepared by using CA (as carbon precursor) and glycine, thioacetic acid, and cysteine (as dopants). CA (2g) only, CA (2g) with glycine (200 mg), CA (2g) with thioacetic acid (200 mg), and CA (2g) with cysteine (200 mg) without any solvent were heated at 200^{o} C for 5 min. for preparing U-Cdots, N-Cdots, S-Cdots, and N, S-Cdots. The mixture gets liquified and the solution becomes yellow from colorless and further turns into orange color, which results in the development of Cdots.[18] The highly soluble orange color solution of Cdots is dispersed in an aqueous medium after the solution gets cool down.

4.2.3 Synthesis of MnO_2 nanospheres

The MnO_2 NS were prepared by mixing an equal ratio of L-methionine and $KMnO_4$ in ultrapure distilled water at room temperature by constant stirring (20 minutes). The color of the reaction mixture turns brown from light pink in a few minutes, which confirms the development of MnO_2 NS. The $2e^-$-redox reaction occurred between Mn (+7) and L-methionine.[19]

4.2.4 Characterization

The absorption spectra of developed nanomaterials were recorded with the use of a UV−vis spectrophotometer (Shimadzu, UV-2600). The PL emission spectra were carried out via spectrofluorometer (Shimadzu, RF-6000). The morphology, shape, and size of MnO_2 NS and Cdots were observed by using a (TEM, TALOS F200S G2). IR spectra were examined by FT-IR spectroscopy (Shimadzu, IRTracer-100). The elemental composition of prepared Cdots was determined by XPS (PHI 5000 VersaProbe III). The fluorescence lifetime decays were recorded by TCSPC measurements using a Deltaflex modular fluorescence lifetime system (HORIBA Scientific) with an excitation source at 340 nm (nano-LED pulse diode light).

4.2.5 Preparation of Sample Solutions

Stock solution (20 μL) of each Cdots was transferred into a cuvette and further diluted with 1980 μL of distilled water. Further, there was the addition of a specific amount of MnO_2 NS solution in the cuvette for determining the fluorescence quenching studies of each Cdots. Moreover, the fluorescence restoration of each Cdots was examined by the addition of a particular quantity of GSH.

4.3 Result and Discussion

4.3.1 Characterization

TEM images of prepared MnO_2 NS show the spherical morphology of nanoparticles with an approximate diameter of 65 nm (Figure 4.1). It has been found in the literature that N and S doping in the framework of Cdots has a high impact on their PL properties.[20] Cysteine as a precursor used for N, S-doping onto the Cdots. The carboxyl and hydroxyl groups significantly enhance the quantum yield of Cdots.[21] CA has both carboxyl and hydroxyl groups and therefore, it was used as the main precursor for the preparation of Cdots. The synthesis

process of N, S-Cdots was based on the condensation of CA and cysteine and further carbonization.

The morphology and lattice spacing of the N, S-Cdots were determined by a HRTEM image. Figure 4.2(a, b) shows TEM images of the N, S-Cdots in which particles are spherical and uniformly dispersed. The inset image of Figure 4.2(b) showed an HRTEM image of N, S-Cdots that have lattice space value of 0.224 nm indicating (100) graphitic lattice. Figure 4.2(c) displays the histogram distribution of N, S-Cdots with a fine range of particle size from 4 to 8 nm (average dia. 6 nm). The EDS elemental mapping of N, S-Cdots shows the uniform distribution of C, N, O, and S (Figure 4.3).

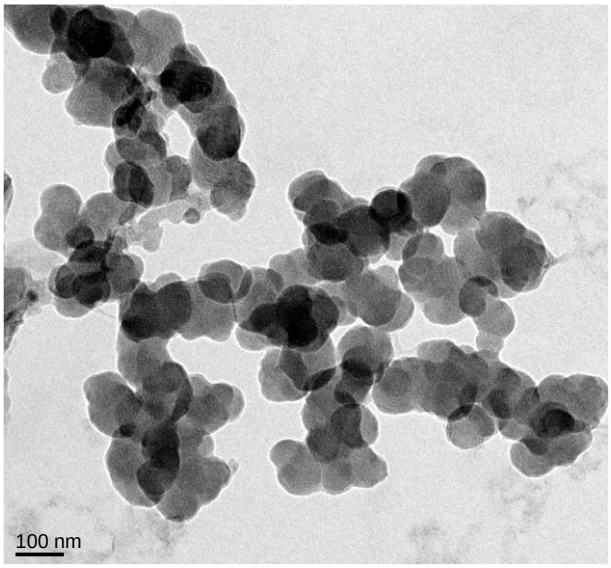

Figure 4.1. TEM image of MnO_2 NS.

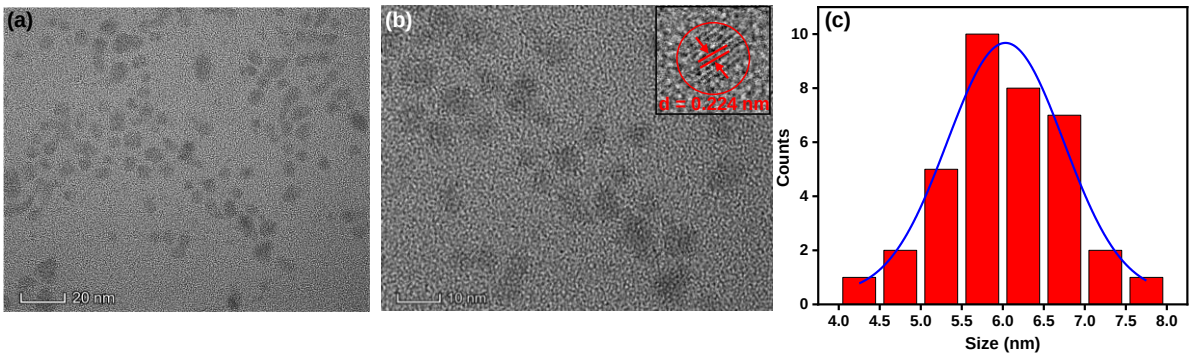

Figure 4.2. TEM images (a, b) of N, S-Cdots at different measuring scale of 20 nm and 10 nm, respectively. Inset image of (b) represent the HRTEM image, and (c) particle size histogram of N, S-Cdots.

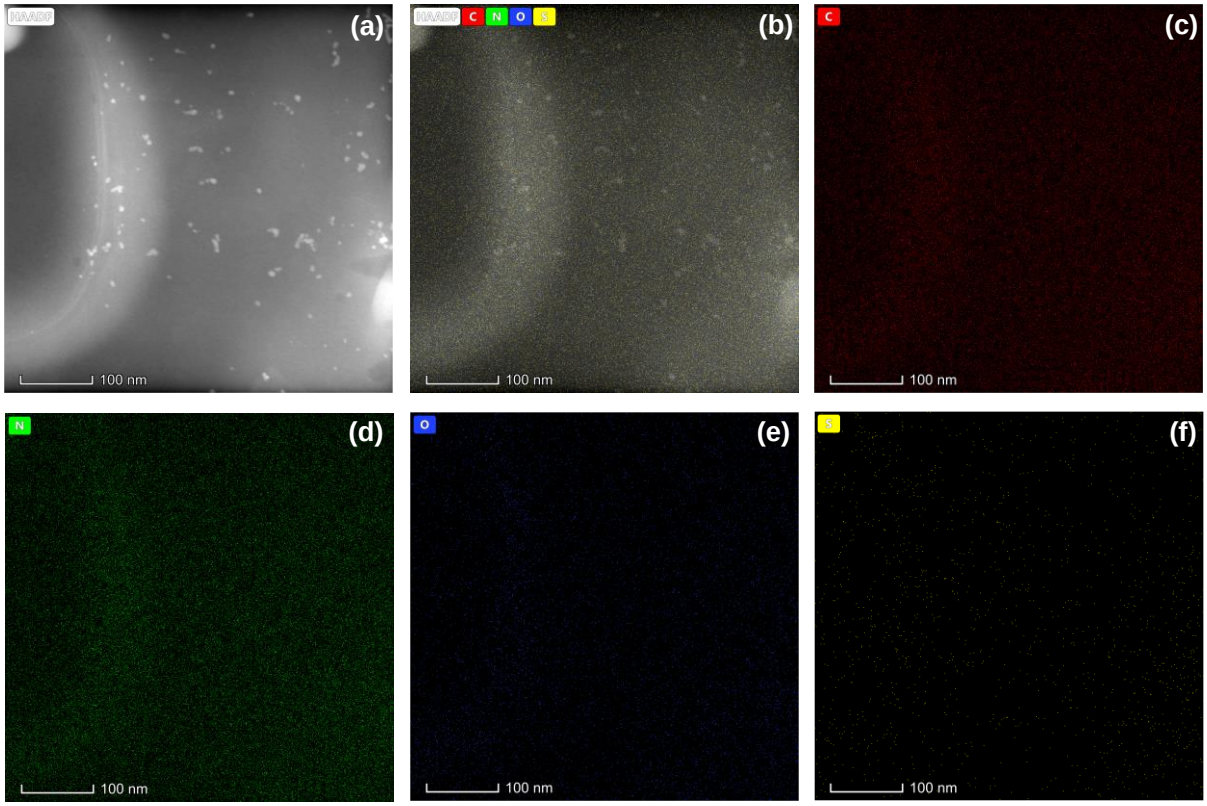

Figure 4.3. (a) HAADF and EDS elemental mapping of N, S-Cdots representing (b) overlap, (c) carbon, (d) nitrogen, (e) oxygen, and (f) sulfur.

The analysis of various functional groups was done by IR spectroscopy. Figure 4.4(a) shows the FTIR spectrum of U-Cdots, N-Cdots, S-Cdots, and N, S-Cdots. A broad absorption band at 3400 cm^{-1} designates the existence of O-H bond in FTIR spectrum. The peak at about 1720, 1630, 1400, and 1210 cm^{-1} reflect C=O stretching vibrations, C=C bonds, C-N bonds, and O-C-O stretching vibrations, respectively.[22] The medium peak at 2550 cm^{-1} refers to S-H stretching vibrations.[21] The peaks from 980 to 1200 cm^{-1} related to the presence of C-O-C and C-S-C bonds.[23]

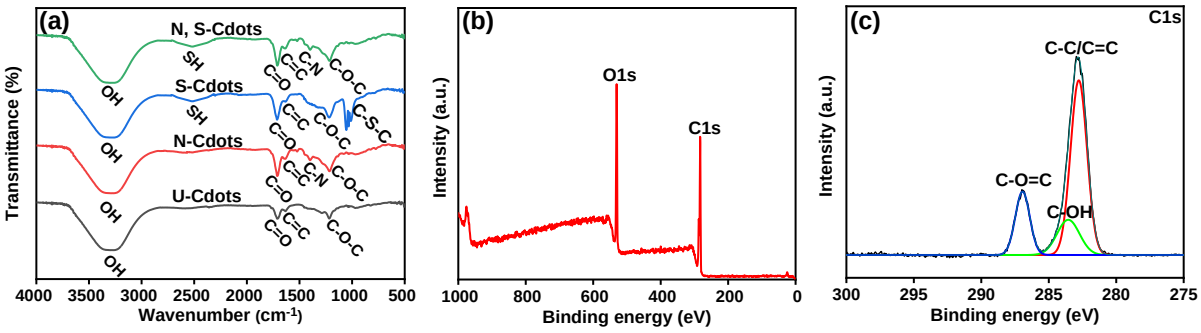

Figure 4.4. (a) FTIR spectrum of U-Cdots, N-Cdots, S-Cdots, and N, S-Cdots, (b) Survey spectrum of U-Cdots, and (c) High-resolution spectrum of C1s.

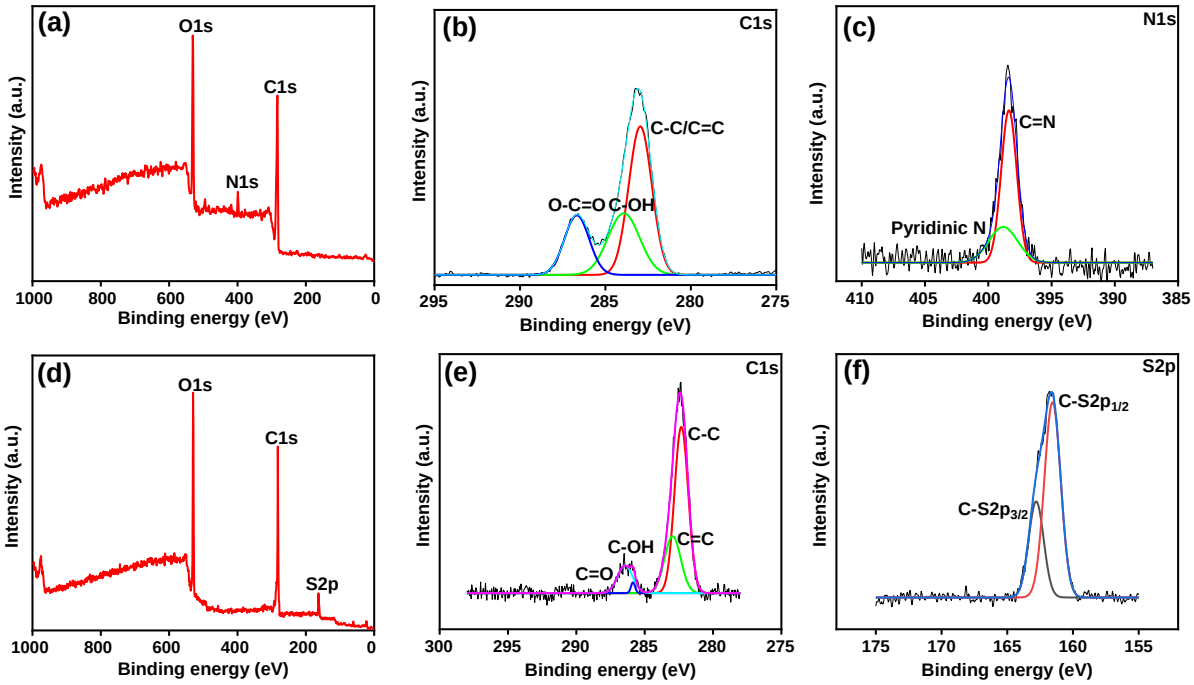

Figure 4.5. Survey spectrum of (a) N-Cdots and (d) S-Cdots, High-resolution spectrum of C1s of (b) N-Cdots and (e) S-Cdots, (c) High-resolution spectrum of N1s of N-Cdots, and (f) High-resolution spectrum of S2p of S-Cdots.

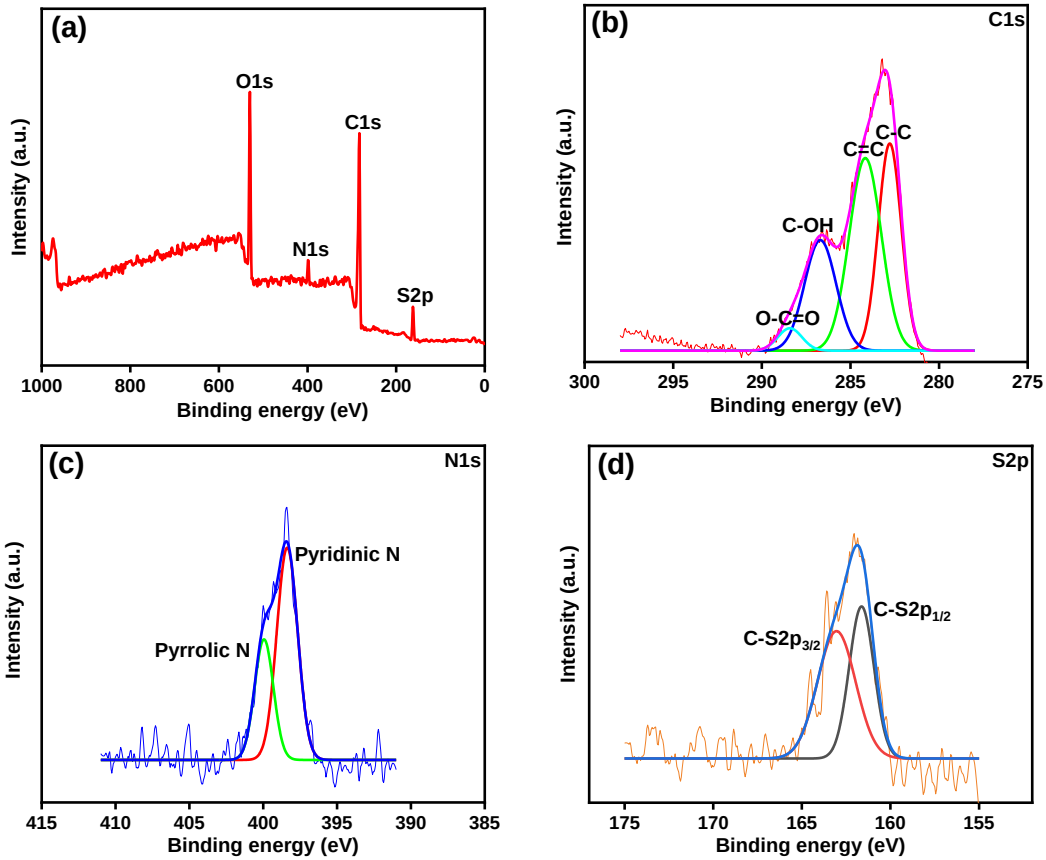

Figure 4.6. (a) XPS survey spectrum of N, S-Cdots and High-resolution spectrum of (b) C1s, (c) N1s, and (d) S2p of N, S-Cdots.

Further, the composition and oxidation state of four different Cdots i.e., U-Cdots, N-Cdots, S-Cdots, and N, S-Cdots were analyzed by XPS spectra. The hydroxyl, carboxyl, and amine groups present on the surface of prepared Cdots enhance their water solubility. The XPS survey spectrum of four different Cdots exhibited major peaks at approximately 531.2, 400.5, 284.6, and 164.7 eV refer to O1s, N1s, C1s, and S2p, respectively (Figure 4.4(b), 4.5(a), 4.5(d), and 4.6(a)).[24,25] The high-resolution C1s spectrum consists of prominent peaks at about 288.4, 286.7, 284.3, 282.7 eV ascribed to the O-C=O, C-OH, C=C, and C-C, respectively (Figure 4.4(c), 4.5(b), 4.5(e), and 4.6 (b)).[20,26,27] The N1s spectrum displays major peaks at 400.2, 398.7, and 398.3 eV suggesting the existence of pyrrolic N, pyridinic N, and C=N (Figure 4.5(c), 4.6(c)).[25] The high-resolution spectrum of S2p exhibited two peaks at 163.0 and 161.6 eV related to the C-S2$p_{3/2}$ and C-S2$p_{1/2}$ (Figure 4.5(f), 4.6(d)).[28]

4.3.2 Optical properties

Figure 4.7(a) displays the UV-visible absorption spectra of prepared N, S-Cdots. The UV-visible spectra represent two predominant peaks, the first peak at about 245 nm correlated to the π-π* transition because of sp^2 aromatic domains and the second peak at 340 nm refers to n-π* transition due to the C=O group.

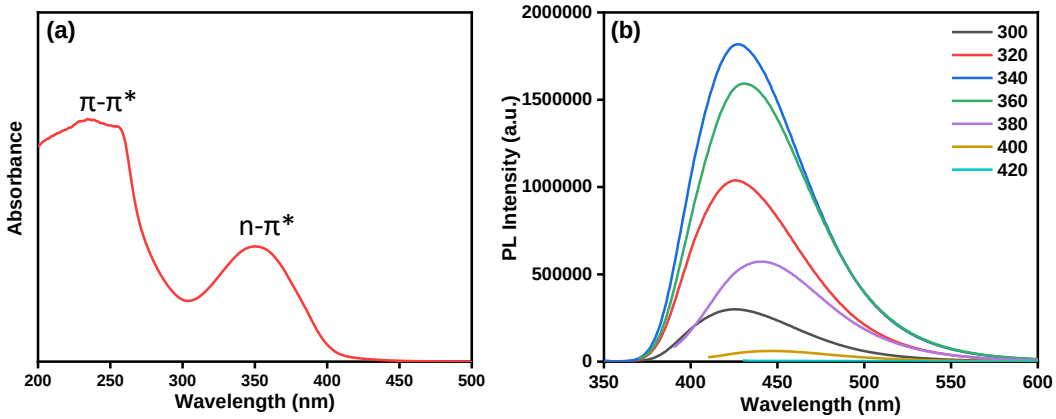

Figure 4.7. (a) UV-Visible absorption spectra of N, S-Cdots and (b) PL spectra of N, S-Cdots when excited at different wavelengths.

Figure 4.7(b) depicts the fluorescent spectra of N, S-Cdots for variable excitation wavelengths, ranges 300 nm to 420 nm. The maximum PL intensity of N, S-Cdots has been observed at 427 nm corresponds to 340 nm (λ_{ex}). The shift in maximum emission peak of N, S-Cdots from 423 nm to 450 nm with varying λ_{ex} of 300 nm to 420 nm. PL spectra of N, S-Cdots show excitation-

dependent PL behavior, which is further dependent upon its surface. The presence of distinct functional groups on the N, S-Cdots results in the number of emissive traps among π-π* transition due to C-C of functionalities existing on its surface.[24] There have been different PL mechanisms of C-dots reported in the literature, for example, excitons of carbon core, quantum confinement effect, emissive traps, surface defects, etc.[29] In the case of heteroatom-doped C-dots, the presence of many functional groups leads to introduce novel excitation energy traps, and the passivation of surface defects can change the PL properties of Cdots.[30] From the above investigation, it can be concluded that the synergistic effects of these mechanisms led to tunable PL emission of N, S-Cdots.

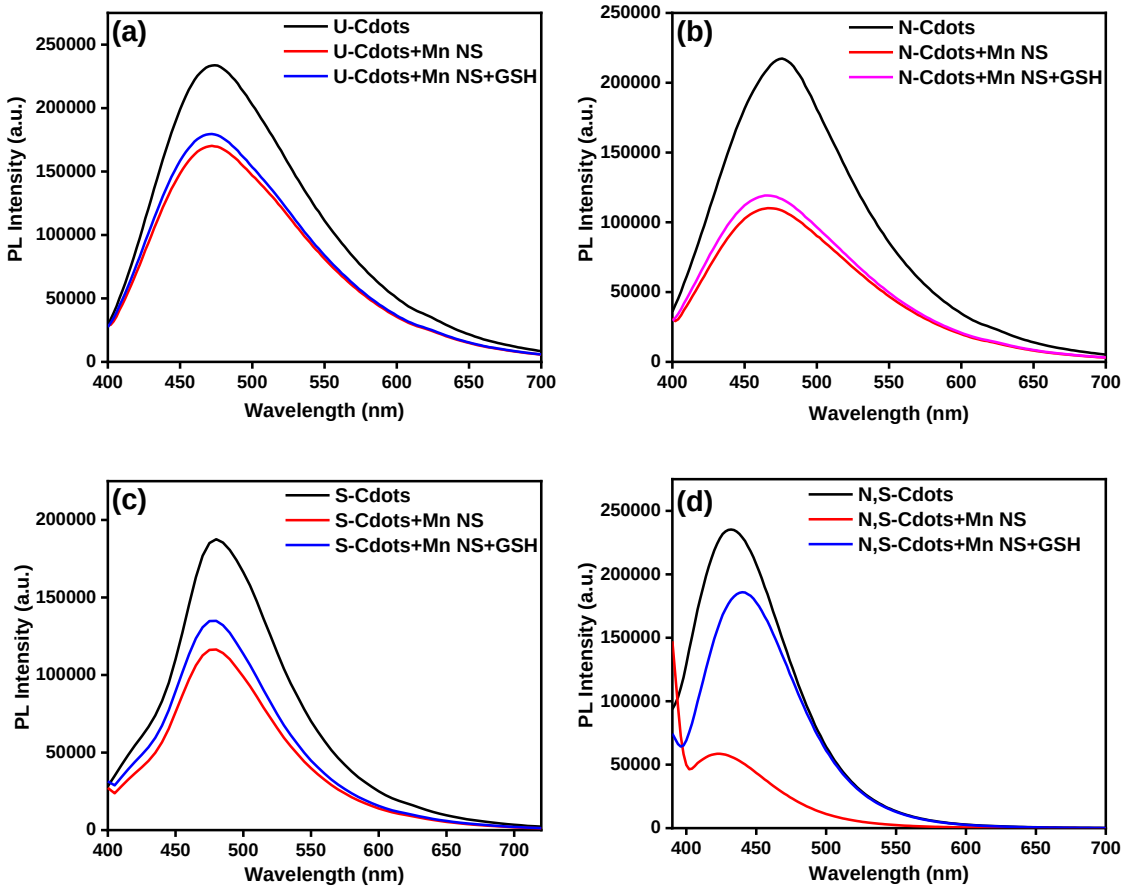

Figure 4.8. PL quenching with MnO_2 nanospheres (Mn NS) and further PL restoration with GSH of different Cdots i.e., (a) U-Cdots, (b) N-Cdots, (c) S-Cdots, and (d) N, S-Cdots.

4.3.3 Interaction of different Cdots with MnO_2 nanospheres and detection of GSH

The four different types of heteroatoms doped Cdots i.e., U-Cdots, N-Cdots, S-Cdots, and N, S-Cdots were used to study their interaction with MnO_2 NS and further the prepared

systems of four Cdots with MnO_2 NS used for the detection of GSH. Figure 4.8 displays the PL spectra of all four different types of Cdots in which the fluorescence of Cdots was quenched differently for a particular amount of MnO_2 NS. Also, the PL intensity of all Cdots gets restored differently by adding a specific amount of GSH in each Cdots-MnO_2 system (Figure 4.8). Further, the percentage of "turn off" (i.e., quenching) and "turn on" (i.e., restoration) of PL intensity for all Cdots by addition of MnO_2 NS and GSH are represented as bar graph in Figure 4.9(a) & 4.9(b), respectively. It was found that the N, S-Cdots show maximum turn off (%) i.e., 77 % and maximum turn on (%) i.e., 68 % of PL intensity.

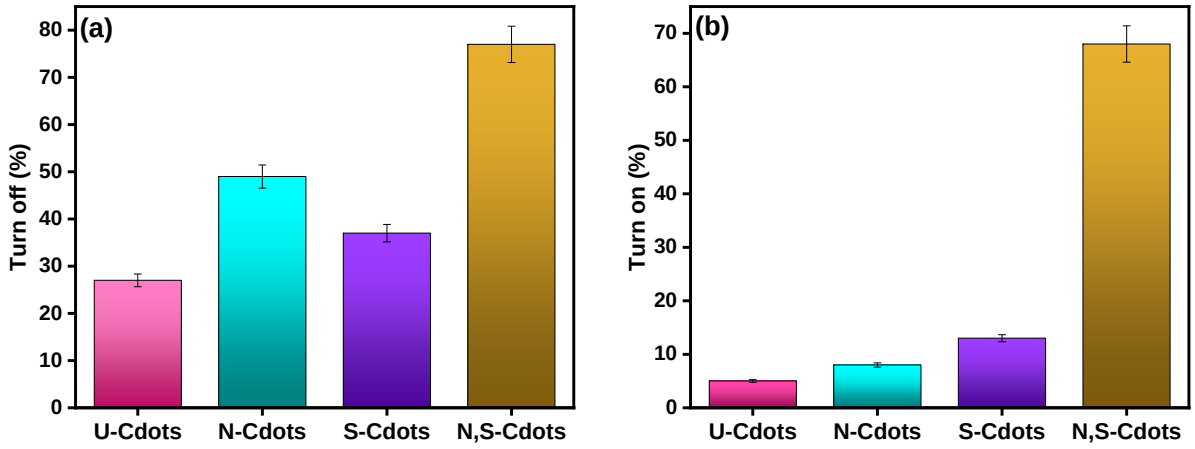

Figure 4.9. (a) Bar graph representing "turn off" (%) of PL intensity of different heteroatom doped Cdots with the addition of specific concentration of MnO_2 NS and (b) Bar graph showing "turn on" (%) of PL intensity of different Cdots-MnO_2 system with the addition of GSH.

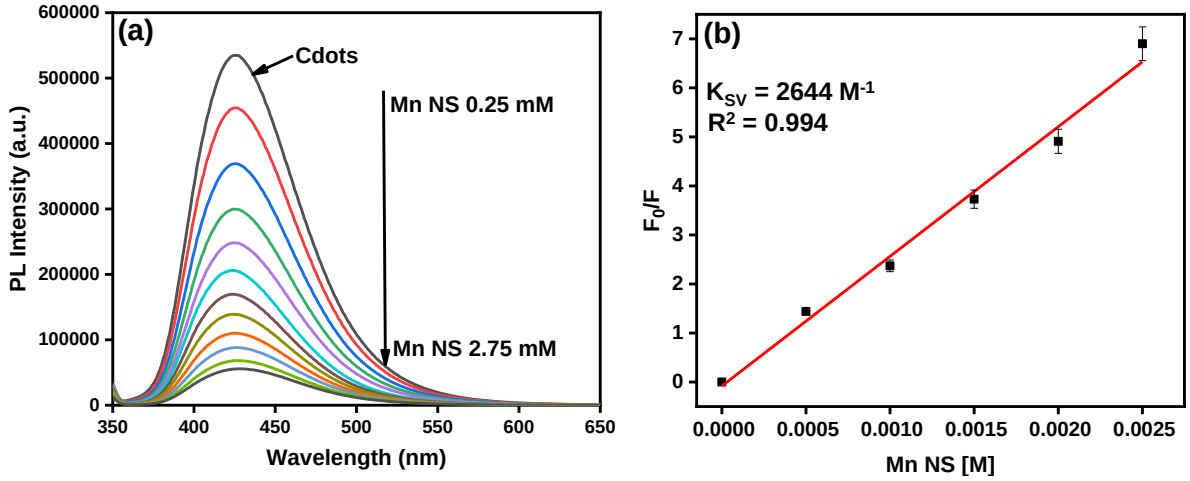

Figure 4.10. (a) PL quenching spectra of N, S-Cdots with varying MnO_2 NS and (b) Stern-Volmer quenching plot of MnO_2 NS with N, S-Cdots.

4.3.4 Fluorescence quenching of N, S-Cdots by MnO_2 nanospheres

The prepared N, S-Cdots exhibited high PL intensity when excited at 340 nm. The MnO_2 nanosphere ranging from 0.25 mM to 2.75 mM decreased the fluorescence value of N, S-Cdots (Figure 4.10(a)). The maximum quenching efficiency i.e., 90% was evaluated in the presence of 2.75 mM MnO_2 NS. The range of quenching efficiency of MnO_2 NS has been evaluated via Stern-Volmer equation (1.4). Figure 4.10(b) represents the Stern-Volmer plot between PL responses (F_0/F) and different concentrations of MnO_2 NS. The above Stern-Volmer plot shows a linear equation with slope i.e., K_{SV} equal to 2644 M^{-1} and value of R^2 equal to 0.994.

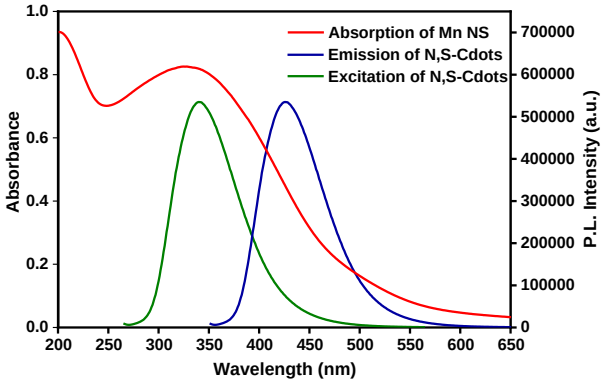

Figure 4.11. Spectral overlap between UV-Visible absorption spectrum of MnO_2 NS and PL emission spectra of N, S-Cdots.

The quenching mechanism followed by N, S-Cdots-MnO_2 NS system was also investigated. There is mostly fluorescence quenching of Carbon dots depending upon different mechanisms i.e., static quenching, dynamic quenching, FRET, and IFE.[15,31] To demonstrate the exact fluorescence quenching mechanism of N, S-Cdots with MnO_2 NS further studies have been done. The significant spectral overlap between the broad absorption spectrum of MnO_2 NS and the excitation/emission spectrum of N, S-Cdots (Figure 4.11). This shows that the IFE could occur between the MnO_2 NS and N, S-Cdots. FRET also occurs when there is a spectral overlap between the PL emission spectrum of Cdots and the UV-vis absorption spectrum of the quencher.[32] FRET arises due to long series dipole-dipole interaction in quencher with Cdots lacking the generation of a photon.[15] The zeta potential of N, S-Cdots and MnO_2 NS was measured to be -1.23 mV and -0.22 mV, respectively (Table 4.1). This result showed that the complex formation among the N, S-Cdots and MnO_2 NS was not possible and this also indicated that the FRET mechanism is not the quenching mechanism for them.

Table 4.1. The zeta potential values of different carbon dots and MnO_2 NS.

System	Zeta Potential (mV)
U-Cdots	+2.90
N-Cdots	+0.40
S-Cdots	-0.80
N, S-Cdots	-1.23
MnO_2	-0.22

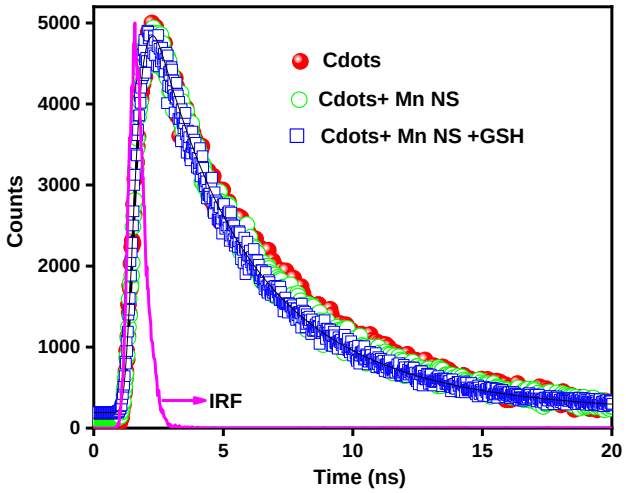

Figure 4.12. The fluorescence lifetime studies of N, S-Cdots in the presence of MnO_2 NS and GSH.

Table 4.2. The different parameters for the evaluation of IFE on the fluorescence quenching of N, S-Cdots.

MnO_2 (mM)	A_{ex}	A_{em}	CF	F_{obsd}	F_{cor}	E_{obsd}	E_{cor}	$F_{cor}/F_{cor,0}$
0	0.023	0.001	1.025	535314	549223	0.000	0.000	1.00
0.25	0.092	0.067	1.187	454668	539875	0.150	0.017	0.98
0.50	0.208	0.105	1.400	369609	517512	0.309	0.057	0.94
0.75	0.357	0.189	1.780	297283	529214	0.444	0.036	0.96
1.00	0.444	0.252	2.069	248726	514623	0.535	0.063	0.93
1.25	0.572	0.305	2.462	207300	510398	0.612	0.070	0.92

[e]Experimental error ±5 %

For further confirmation of quenching mechanism, the fluorescence lifetime studies of N, S-Cdots in the vicinity of Mn NS have been investigated (Figure 4.12). There was no variation

across lifetime of N, S-Cdots in the presence of Mn NS, which confirmed the IFE quenching mechanism.[16] Further, the following Parker equation (1.12) was examined to verify the IFE process.[15] The investigation of different parameters based on equation (1.12) for the confirmation of IFE was evaluated and summarized in Table 4.2. The ratio of F_{cor}/F_{obsd} is expressed as the correction factor (CF). The values of CF were calculated at different concentrations of MnO_2 NS.

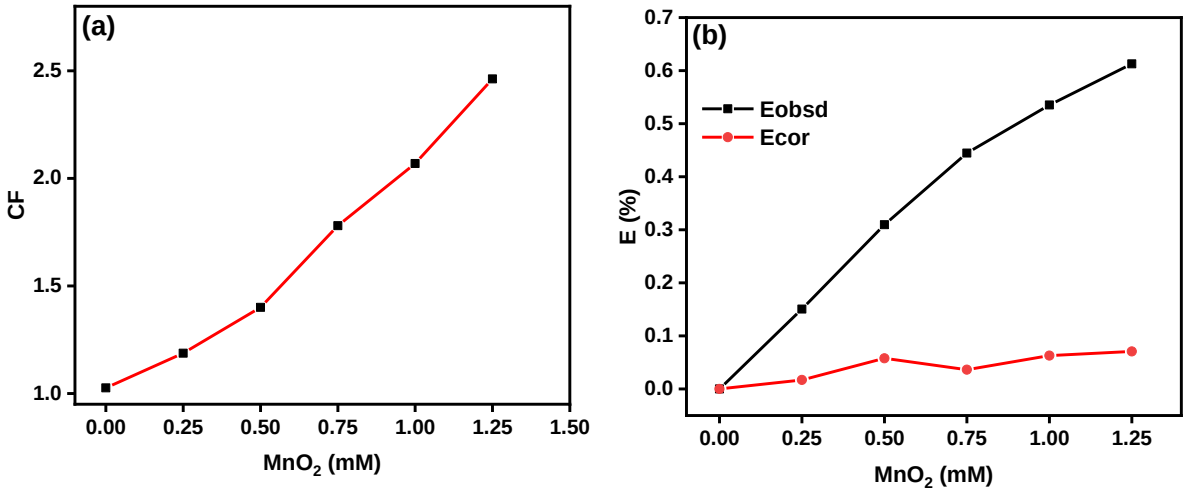

Figure 4.13. (a) The plot between the CF and different concentrations of MnO_2 NS and (b) Observed suppressed efficiency (E_{obsd}) and corrected suppressed efficiency by removing IFE (E_{cor}) in the presence of various concentrations of MnO_2 NS.

The increase in CF value has been obtained with MnO_2 NS (Figure 4.13(a)) and this result fit in the Parker equation (1.12). This confirmed that the quenching mechanism followed by the N, S-Cdots with MnO_2 NS is IFE. The suppressed efficiency for the fluorescence of N, S-Cdots in the vicinity of MnO_2 NS evaluated by the PL spectrophotometer and their respective corrected ones was also investigated (Figure 4.13(b)). The value of E was determined by using $E = 1-F/F_0$, where F_0 and F are the fluorescence emission by N, S-Cdots without and with the addition of MnO_2 NS, respectively. It showed that the IFE has a significant impact in suppressing the fluorescence intensity of N, S-Cdots.

4.3.5 Restoration mechanism of Cdots and detection of GSH

The quenched fluorescence of N, S-Cdots gets restored by GSH addition. The restoration effect by the addition of GSH in N, S-Cdots-MnO_2 sensing system ranging from 10 µM to 90 µM is shown in Figure 4.14(a). The restoration of PL intensity of N, S-Cdots was governed by increasing GSH concentration in the prepared sensing system. This is due to the

redox reaction among the MnO_2 NS and GSH in which reduction of MnO_2 to Mn^{2+} occurs and GSH gets oxidized to GSH di-sulfide (GS-GS) as shown in the equation (2.1).[33] This shows that there was the removal of N, S-Cdots from large surface of MnO_2 NS which leads to recovery of PL intensity of N, S-Cdots. Figure 4.14(b) displays a good linear plot of the F-F_0/F_0 i.e., PL responses of N, S-Cdots-MnO_2 sensing system against different concentration of 0.1 µM to 0.5 µM with F-F_0/F_0 = 2.04[GSH]-0.118 linear equation and R^2 = 0.995. The LOD was found to be 80 nM. The prepared N, S-Cdots-MnO_2 system showed high selectivity for detecting GSH. The obtained sensor is superior compared to other sensing probes based on the fluorimetry technique (Table 1.1).

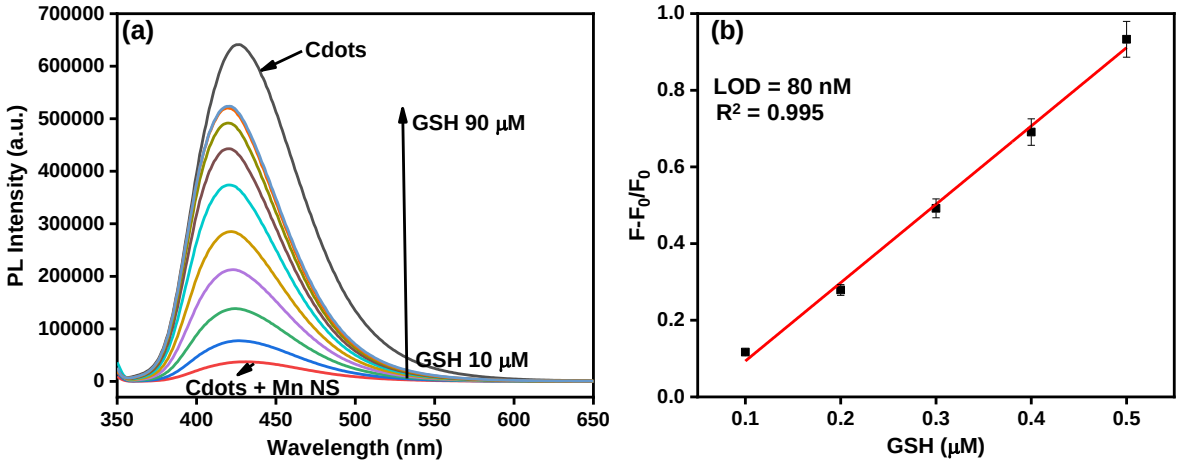

Figure 4.14. (a) PL recovery of N, S-Cdots-MnO_2 sensing system in the addition of varying GSH (10 µM-90 µM) and (b) Relation among PL responses (F-F_0/F_0) of N, S-Cdots-MnO_2 sensing system and different concentrations of GSH.

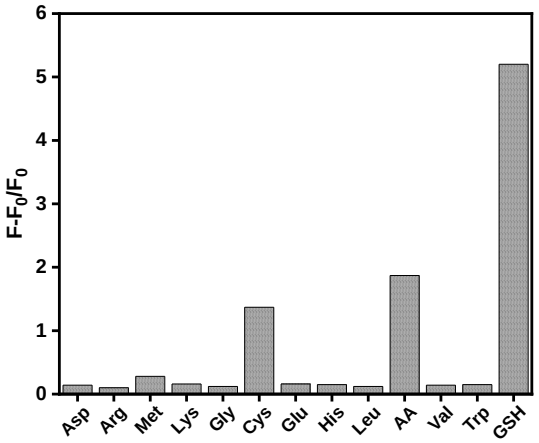

Figure 4.15. Selectivity bar graph illustrating the interference studies of N, S-Cdots-MnO_2 sensing system in presence of various amino acids at the fixed concentration (50 µM).

To study the selectivity of N, S-Cdots-MnO_2 sensing system, the different amino acids such as Asp, Arg, Met, Lys, Gly, Cys, glutamic acid (Glu), His, Leu, AA, Val, Trp, and GSH was used. The specific concentration i.e., 50 µM of all amino acids, was added to the prepared sensor. It was found that the prepared sensing probe had high selectivity for GSH as compared to other amino acids (Figure 4.15).

Table 4.3. The values of quantum yield for the different types of Cdots in the presence of MnO_2 NS and GSH.[f]

Systems	Quantum Yield (%)
U-Cdots	9.65
U-Cdots+MnO_2	2.09
U-Cdots+MnO_2+GSH	4.78
S-Cdots	22.31
S-Cdots+MnO_2	6.75
S-Cdots+MnO_2+GSH	12.73
N-Cdots	28.49
N-Cdots+MnO_2	4.17
N-Cdots+MnO_2+GSH	15.60
N, S-Cdots	73.42
N, S-Cdots+MnO_2	9.19
N, S-Cdots+MnO_2+GSH	52.57

[f]Experimental error ±5 %

4.3.6 Fluorescence quantum yield measurements

Co-doped Cdots exhibit high quantum yield, different coordination sites, and additional surface defects in their structure compared to single heteroatom doped Cdots.[34] Therefore, co-doped Cdots (N, S-Cdots) consider as best Cdots as compared to the other three single heteroatom doped Cdots for further detection of GSH by using MnO_2 NS. Further, the quantum yield of each carbon dots was evaluated in the lack and inclusion of MnO_2 NS and GSH (Table 4.3). It was found that the N, S-Cdots showed the highest quantum yield i.e., 73.42 %. The value of quantum yield is highly quenched (~ 87%) in the presence of MnO_2 NS and highly recovered (~ 82 %) for N, S-Cdots as compared to other carbon dots. It demonstrated that the N, S-Cdots showed the best results in comparison with other carbon dots.

Conclusion

In summary of this chapter, four different heteroatom doped carbon dots (Cdots) have been synthesized, including undoped Cdots (U-Cdots), nitrogen-doped Cdots (N-Cdots), and sulfur-doped Cdots (S-Cdots) by high-temperature treatment for 5 min. N, S-Cdots showed a high value of the quantum yield and attractive properties as compared to others due to synergistic effect of nitrogen and sulfur. The prepared all heteroatom doped Cdots with MnO_2 NS were used as nanosensors for the sensing of GSH. N, S-Cdots-MnO_2 NS demonstrated the best performance for the detection of glutathione (GSH). The negative values of zeta potential for N, S-Cdots and MnO_2 NS displayed repulsion between them. The significant spectral overlap among the absorption spectra of MnO_2 NS with excitation/emission spectra of N, S-Cdots showed the inner filter effect between them. N, S-Cdots shows no change in the average lifetime values after the addition of MnO_2 NS, which confirms the IFE. The addition of GSH in the N, S-Cdots-MnO_2 NS cause the redox reaction between MnO_2 and GSH, result in conversion of MnO_2 to Mn^{2+} ions and restoration of PL intensity of N, S-Cdots. N, S-Cdots-Mn NS acted as a good sensor for GSH and showed high selectivity.

References

(1) Lim, S. Y.; Shen, W.; Gao, Z. Carbon Quantum Dots and Their Applications. *Chem. Soc. Rev.* **2015**, *44* (1), 362–381. https://doi.org/10.1039/C4CS00269E.

(2) Xu, Q.; Pu, P.; Zhao, J.; Dong, C.; Gao, C.; Chen, Y.; Chen, J.; Liu, Y.; Zhou, H. Preparation of Highly Photoluminescent Sulfur-Doped Carbon Dots for Fe(iii) Detection. *J. Mater. Chem. A* **2015**, *3* (2), 542–546. https://doi.org/10.1039/C4TA05483K.

(3) Murru, C.; Badía-Laíño, R.; Díaz-García, M. E. Synthesis and Characterization of Green Carbon Dots for Scavenging Radical Oxygen Species in Aqueous and Oil Samples. *Antioxidants* **2020**, *9* (11), 1147. https://doi.org/10.3390/antiox9111147.

(4) Rong, M.-C.; Zhang, K.-X.; Wang, Y.-R.; Chen, X. The Synthesis of B, N-Carbon Dots by a Combustion Method and the Application of Fluorescence Detection for Cu^{2+}. *Chinese Chem. Lett.* **2017**, *28* (5), 1119–1124. https://doi.org/10.1016/j.cclet.2016.12.009.

(5) Nayak, S.; Das, P.; Singh, M. K. Carbon Dot with Aggregation Induced Emission and PH Triggered Disintegration. *Colloid Interface Sci. Commun.* **2021**, *45*, 100537.

https://doi.org/10.1016/j.colcom.2021.100537.

(6) Qian, Z.; Shan, X.; Chai, L.; Ma, J.; Chen, J.; Feng, H. Si-Doped Carbon Quantum Dots: A Facile and General Preparation Strategy, Bioimaging Application, and Multifunctional Sensor. *ACS Appl. Mater. Interfaces* **2014**, *6* (9), 6797–6805. https://doi.org/10.1021/am500403n.

(7) Song, Y.; Zhu, C.; Song, J.; Li, H.; Du, D.; Lin, Y. Drug-Derived Bright and Color-Tunable N-Doped Carbon Dots for Cell Imaging and Sensitive Detection of Fe^{3+} in Living Cells. *ACS Appl. Mater. Interfaces* **2017**, *9* (8), 7399–7405. https://doi.org/10.1021/acsami.6b13954.

(8) Shin, J.; Guo, J.; Zhao, T.; Guo, Z. Functionalized Carbon Dots on Graphene as Outstanding Non-Metal Bifunctional Oxygen Electrocatalyst. *Small* **2019**, *15* (16), 1900296. https://doi.org/10.1002/smll.201900296.

(9) Sharma, V.; Kaur, N.; Tiwari, P.; Saini, A. K.; Mobin, S. M. Multifunctional Fluorescent "Off-On-Off" Nanosensor for Au^{3+} and S^{2-} Employing N-S Co-Doped Carbon–Dots. *Carbon N. Y.* **2018**, *139*, 393–403. https://doi.org/10.1016/j.carbon.2018.07.004.

(10) Tang, M.; Zhu, B.; Wang, Y.; Wu, H.; Chai, F.; Qu, F.; Su, Z. Nitrogen- and Sulfur-Doped Carbon Dots as Peroxidase Mimetics: Colorimetric Determination of Hydrogen Peroxide and Glutathione, and Fluorimetric Determination of Lead(II). *Microchim. Acta* **2019**, *186* (9), 604. https://doi.org/10.1007/s00604-019-3710-4.

(11) Ngeontae, W.; Chaiendoo, K.; Ngamdee, K.; Ruangchai, S.; Saiyasombat, C.; Busayaporn, W.; Ittisanronnachai, S.; Promarak, V. A Highly Selective Fluorescent Sensor for Manganese(II) Ion Detection Based on N,S-Doped Carbon Dots Triggered by Manganese Oxide. *Dye. Pigment.* **2022**, *203*, 110325. https://doi.org/10.1016/j.dyepig.2022.110325.

(12) Chatzimitakos, T.; Kasouni, A.; Sygellou, L.; Leonardos, I.; Troganis, A.; Stalikas, C. Human Fingernails as an Intriguing Precursor for the Synthesis of Nitrogen and Sulfur-Doped Carbon Dots with Strong Fluorescent Properties: Analytical and Bioimaging Applications. *Sensors Actuators B Chem.* **2018**, *267*, 494–501. https://doi.org/10.1016/j.snb.2018.04.059.

(13) Li, J.; Rao, X.; Xiang, F.; Wei, J.; Yuan, M.; Liu, Z. A Photoluminescence "Switch-on"

Nanosensor Composed of Nitrogen and Sulphur Co-Doped Carbon Dots and Gold Nanoparticles for Discriminative Detection of Glutathione. *Analyst* **2018**, *143* (9), 2083–2089. https://doi.org/10.1039/C8AN00168E.

(14) Sohal, N.; Maity, B.; Shetti, N. P.; Basu, S. Biosensors Based on MnO_2 Nanostructures: A Review. *ACS Appl. Nano Mater.* **2021**, *4* (3), 2285–2302. https://doi.org/10.1021/acsanm.0c03380.

(15) Zu, F.; Yan, F.; Bai, Z.; Xu, J.; Wang, Y.; Huang, Y.; Zhou, X. The Quenching of the Fluorescence of Carbon Dots: A Review on Mechanisms and Applications. *Microchim. Acta* **2017**, *184* (7), 1899–1914. https://doi.org/10.1007/s00604-017-2318-9.

(16) Wang, H.; Na, X.; Liu, S.; Liu, H.; Zhang, L.; Xie, M.; Jiang, Z.; Han, F.; Li, Y.; Cheng, S.; Tan, M. A Novel "Turn-on" Fluorometric and Magnetic Bi-Functional Strategy for Ascorbic Acid Sensing and in Vivo Imaging via Carbon Dots-MnO_2 Nanosheet Nanoprobe. *Talanta* **2019**, *201*, 388–396. https://doi.org/10.1016/j.talanta.2019.04.022.

(17) Gupta, A.; Nandi, C. K. PC12 Live Cell Ultrasensitive Neurotransmitter Signaling Using High Quantum Yield Sulphur Doped Carbon Dots and Its Extracellular Ca^{2+} Ion Dependence. *Sensors Actuators B Chem.* **2017**, *245*, 137–145. https://doi.org/10.1016/j.snb.2017.01.145.

(18) Dong, Y.; Wang, R.; Li, H.; Shao, J.; Chi, Y.; Lin, X.; Chen, G. Polyamine-Functionalized Carbon Quantum Dots for Chemical Sensing. *Carbon N. Y.* **2012**, *50* (8), 2810–2815. https://doi.org/10.1016/j.carbon.2012.02.046.

(19) Sohal, N.; Maity, B.; Basu, S. Carbon Dot-MnO_2 Nanosphere Composite Sensors for Selective Detection of Glutathione. *ACS Appl. Nano Mater.* **2020**, *3* (6), 5955–5964. https://doi.org/10.1021/acsanm.0c01088.

(20) Chen, C.; Zhao, D.; Hu, T.; Sun, J.; Yang, X. Highly Fluorescent Nitrogen and Sulfur Co-Doped Graphene Quantum Dots for an Inner Filter Effect-Based Cyanide Sensor. *Sensors Actuators B Chem.* **2017**, *241*, 779–788. https://doi.org/10.1016/j.snb.2016.11.010.

(21) Zhang, Y.; He, J. Facile Synthesis of S, N Co-Doped Carbon Dots and Investigation of Their Photoluminescence Properties. *Phys. Chem. Chem. Phys.* **2015**, *17* (31), 20154–20159. https://doi.org/10.1039/C5CP03498A.

(22) Mondal, J.; Revuri, V.; Choochana, P.; Ganesan, P.; Kang, W. J.; Lee, Y. Sulfur and Nitrogen Doped Carbon Quantum Dots for Detection of Glutathione and Reduction of Cellular Nitric Oxide in Microglial Cells. *J. Pharm. Investig.* **2020**, *50* (2), 209–218. https://doi.org/10.1007/s40005-019-00466-8.

(23) Dai, B.; Wu, C.; Lu, Y.; Deng, D.; Xu, S. Synthesis and Formation Mechanism of S-Doped Carbon Dots from Low-Molecule-Weight Organics. *J. Lumin.* **2017**, *190*, 108–114. https://doi.org/10.1016/j.jlumin.2017.04.054.

(24) Das, P.; Ganguly, S.; Mondal, S.; Bose, M.; Das, A. K.; Banerjee, S.; Das, N. C. Heteroatom Doped Photoluminescent Carbon Dots for Sensitive Detection of Acetone in Human Fluids. *Sensors Actuators B Chem.* **2018**, *266*, 583–593. https://doi.org/10.1016/j.snb.2018.03.183.

(25) Liu, Y.; Zhu, C.; Gao, Y.; Yang, L.; Xu, J.; Zhang, X.; Lu, C.; Wang, Y.; Zhu, Y. Biomass-Derived Nitrogen Self-Doped Carbon Dots via a Simple One-Pot Method: Physicochemical, Structural, and Luminescence Properties. *Appl. Surf. Sci.* **2020**, *510*, 145437. https://doi.org/10.1016/j.apsusc.2020.145437.

(26) Wang, Z.; Liao, H.; Wu, H.; Wang, B.; Zhao, H.; Tan, M. Fluorescent Carbon Dots from Beer for Breast Cancer Cell Imaging and Drug Delivery. *Anal. Methods* **2015**, *7* (20), 8911–8917. https://doi.org/10.1039/C5AY01978H.

(27) Chen, X.; Wang, X.; Fang, D. A Review on C1s XPS-Spectra for Some Kinds of Carbon Materials. *Fullerenes, Nanotub. Carbon Nanostructures* **2020**, *28* (12), 1048–1058. https://doi.org/10.1080/1536383X.2020.1794851.

(28) Fu, Z.; He, J.; Jia, F.; Wang, M.; Cui, F. Utilizing the Interfacial Reaction of Naphthalenyl Thiosemicarbazide-Modified Carbon Dots for the Ultrasensitive Determination of Fe (III) Ions. *Spectrochim. Acta Part A Mol. Biomol. Spectrosc.* **2020**, *225*, 117485. https://doi.org/10.1016/j.saa.2019.117485.

(29) Xu, Q.; Kuang, T.; Liu, Y.; Cai, L.; Peng, X.; Sreenivasan Sreeprasad, T.; Zhao, P.; Yu, Z.; Li, N. Heteroatom-Doped Carbon Dots: Synthesis, Characterization, Properties, Photoluminescence Mechanism and Biological Applications. *J. Mater. Chem. B* **2016**, *4* (45), 7204–7219. https://doi.org/10.1039/C6TB02131J.

(30) Cui, X.; Wang, Y.; Liu, J.; Yang, Q.; Zhang, B.; Gao, Y.; Wang, Y.; Lu, G. Dual

Functional N- and S-Co-Doped Carbon Dots as the Sensor for Temperature and Fe^{3+} Ions. *Sensors Actuators B Chem.* **2017**, *242*, 1272–1280. https://doi.org/10.1016/j.snb.2016.09.032.

(31) Wang, L.; Jana, J.; Chung, J. S.; Choi, W. M.; Hur, S. H. Designing an Intriguingly Fluorescent N, B-Doped Carbon Dots Based Fluorescent Probe for Selective Detection of NO_2^- Ions. *Spectrochim. Acta Part A Mol. Biomol. Spectrosc.* **2022**, *268*, 120657. https://doi.org/10.1016/j.saa.2021.120657.

(32) Dong, W.; Wang, R.; Gong, X.; Dong, C. An Efficient Turn-on Fluorescence Biosensor for the Detection of Glutathione Based on FRET between N,S Dual-Doped Carbon Dots and Gold Nanoparticles. *Anal. Bioanal. Chem.* **2019**, *411* (25), 6687–6695. https://doi.org/10.1007/s00216-019-02042-3.

(33) Sohal, N.; Maity, B.; Basu, S. Morphology-Dependent Performance of MnO_2 Nanostructure–Carbon Dot-Based Biosensors for the Detection of Glutathione. *ACS Appl. Bio Mater.* **2021**, *4* (6), 5158–5168. https://doi.org/10.1021/acsabm.1c00353.

(34) Xu, Y.; Wang, S.; Hou, X.; Sun, Z.; Jiang, Y.; Dong, Z.; Tao, Q.; Man, J.; Cao, Y. Coal-Derived Nitrogen, Phosphorus and Sulfur Co-Doped Graphene Quantum Dots: A Promising Ion Fluorescent Probe. *Appl. Surf. Sci.* **2018**, *445*, 519–526. https://doi.org/10.1016/j.apsusc.2018.03.156.

CHAPTER-5

Morphology Effect of 1-D MnO_2 Nanostructure on Heteroatom Doped Carbon Dots Based Biosensor for Selective Detection of Glutathione

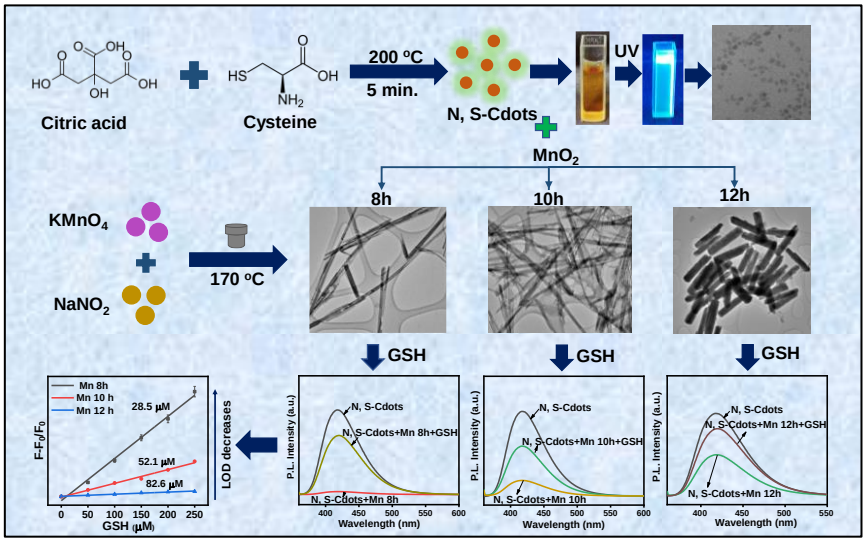

Highlights

- Different morphologies of 1-D MnO_2 nanostructures were prepared via the hydrothermal method.
- N, S-Cdots with different 1-D MnO_2 nanostructures were used as sensor for GSH detection.
- Study of all the photophysical parameters based on the morphology of 1-D MnO_2 nanostructure.
- Developed sensors were based on inner filter effect, confirmed via the Parker equation.
- Specific surface area and aspect ratio of 1-D MnO_2 nanostructures effect sensing activity.

5.1 Introduction

Heteroatom doped Cdots showed high fluorescence efficiency and good sensing activity.[1] The nitrogen-doped Cdots contain terminal amine groups due to which they have high fluorescence quantum yield and can be used in several sensing applications.[2] Recently, it has been discovered that the co-doping of Cdots with different heteroatoms leads to the introduction of more active sites, and the synergistic effect between individual elements showed exclusive sensing selectivity.[3] The fluorescent sensors based on heteroatom doped Cdots depend upon various quenching mechanisms, viz., FRET, static or dynamic quenching, IFE, PET, etc.[4] MnO_2 has extraordinary light absorption ability, a large surface area, and a fast electron transfer rate, which makes it an efficient fluorescence quencher in the preparation of a "turn-off-on" detection probe.[5,6]

The modification in the properties of nanomaterials can be achieved by monitoring their shape, size, morphology, and orientation.[7,8] The morphology and the surface-active sites of MnO_2 play a great role in the sensing activity of materials.[9] 1-D nanostructures such as nanotubes, nanowires, and nanorods have been employed in varied applications ascribed to outstanding optical, mechanical, magnetic, and electronic properties because of their size.[10,11]

In this report, N, S-Cdots have been synthesized through high-temperature treatment without using an acid or a solvent. The different morphologies of 1-D MnO_2 nanostructures were prepared through the hydrothermal treatment by changing the reaction duration at a particular temperature. The morphology of prepared 1-D MnO_2 nanostructures was examined by TEM analysis. The role of different morphologies of 1-D MnO_2 nanostructures was studied for the fluorescence quenching of N, S-Cdots and then fluorescence restoration in the presence of GSH.

5.2 Experimental Section

5.2.1 Materials and reagents

Potassium permanganate ($KMnO_4$) with a 99% purity, sodium nitrite ($NaNO_2$) (99%), Citric acid (99%), L-cysteine (99 %) and sulfuric acid (H_2SO_4) (98%) were purchased from Loba Chemie (India) for the development of MnO_2 nanostructures. L-glutathione (GSH) was bought from Hi-media. The stock solutions were prepared by the use of ultrapure deionized (DI) water which was collected from a double distillation unit.

5.2.2 Synthesis of N, S-Cdots

The synthesis of N, S-Cdots was already explained in Chapter 4.

5.2.3 Synthesis of MnO_2 nanostructures

1-D MnO_2 nanostructures were prepared by using $KMnO_4$ (5 mM) and $NaNO_2$ (7.5 mM) mixed in 40 mL DI water, and further, the gradual addition of 2 mL of H_2SO_4 (0.5 M) was done with constant stirring.[12] The prepared solution was shifted to an autoclave with a Teflon line, and further, it was treated at 170^o C by using the hydrothermal method. After the treatment, the solution was cool down to room temperature and centrifuged for obtaining precipitate after washed with water and ethanol followed by dried at 60^o C. MnO_2 nanostructures with different morphologies were prepared by the same method by varying the hydrothermal reaction time.

5.2.4 Characterization

The absorption spectra of prepared Cdots and MnO_2 nanostructure were recorded through a UV−visible spectrophotometer (Analytik Jena, Specord, India). The photoluminescence (PL) emission spectra were obtained via a fluorescence spectrofluorometer (Shimadzu, RF-6000). The morphology, approximate aspect ratio, size, and shape of Cdots and MnO_2 nanostructures were examined via TEM analysis (TALOS F200S G2). The functional groups of the synthesized Cdots were also recorded by FT-IR spectroscopy (Shimadzu, IRTracer-100). The crystal structure of the developed MnO_2 nanostructures was investigated through XRD (PANALYTICAL X'Pert PRO) using Cu K_α (λ = 1.540 Å) as a source of radiation ($0^\circ \leq 2\theta \leq 90^\circ$). The surface areas of 1-D MnO_2 nanostructures were obtained through a BET surface area analyzer (BEL-miniII, Microtrac Corp. Pvt. Ltd., Japan). The zeta potential was examined through the dynamic light scattering method (DLS, Zetasizer, Malvern).

5.2.5 Preparation of the sample solutions

A 20 μL stock solution of N, S-Cdots was pipetted inside fluorescence cuvette followed by 2 mL DI water. The gradual addition of a particular volume of each 1-D MnO_2 nanostructure solution was done to the cuvette for the measurement of fluorescence quenching efficiency of N, S-Cdots. Moreover, PL recovery for N, S-Cdots was restored by successive addition of GSH.

5.3 Result and Discussion

5.3.1 Characterization

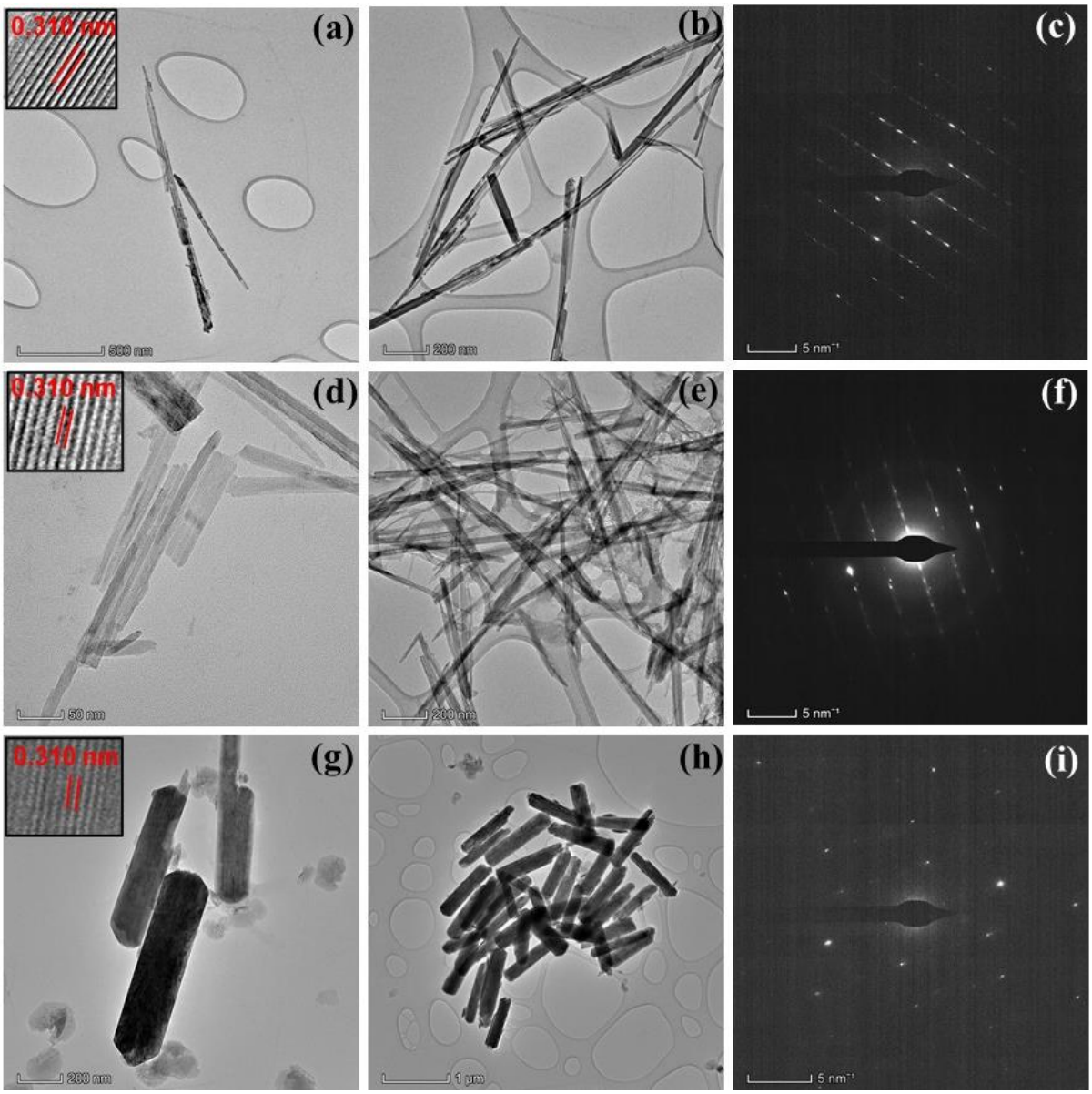

Figure 5.1. (a) TEM images (a, b), (d, e), and (g, h)) of MnO_2 and inset images of (a, d, and g) prepared at 8 h, 10 h, 12 h and SAED pattern (c, f, and i) of Mn 8h, Mn 10h, and Mn 12h, respectively.

The preparation of 1-D MnO_2 nanostructures involved the redox reaction between nitrite and permanganate ions, which was described as follows:

$$2MnO_4^- + 3NO_2^- + 2H^+ \longrightarrow 2MnO_2 + 3NO_3^- + H_2O \qquad (5.1)$$

In the above reaction, permanganate ions are used both as an oxidant as well as a precursor for the Mn element, and on the other hand, nitrite ions act as reducing agents.[12] The stoichiometric

molar ratio involved in this reaction between permanganate and nitrite ions is 2:3. Based on Le Chatelier's principle, the participation of the proton is present in the above reaction. Moreover, the variation in the reaction time (8, 10, 12 h) was done for obtaining 1-D MnO_2 nanostructures with different morphologies. The morphology and shape of 1-D MnO_2 nanostructure synthesized through the hydrothermal method at different reaction times, i.e., 8, 10, and 12 h, was analyzed by TEM images. TEM images (Figure 5.1(a, b) and 5.1(d, e) of MnO_2 nanostructures prepared at 8, and 10 h confirm the formation of MnO_2 nanowires of different aspect ratios. TEM images (Figure 5.1(g, h)) of MnO_2 nanostructures prepared at 12 h confirmed the formation of MnO_2 nanorods. The detailed structural data of the MnO_2 nanostructures were determined by the HRTEM study and SAED patterns. The inset images of Figure 5.1(a), (d), and (g) present a lattice space of 0.310 nm referring to the (310) plane of α-MnO_2.[13] The SAED images (Figure 5.1(c), (f), (i)) of all three samples Mn 8 h, Mn 10 h, and Mn 12 h manifest the single-crystal structure of α-MnO_2.[14] After 10 h of the reaction, the nanorods growth start progressing, and at a reaction time of 12 h, uniform nanorods with a length of >1μm and a diameter of 100-300 nm were formed.

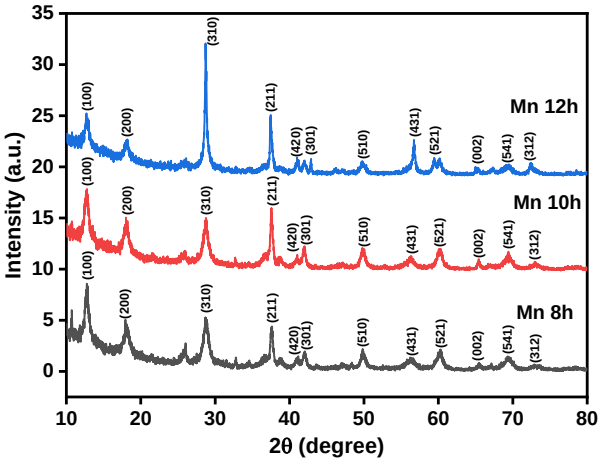

Figure 5.2. XRD pattern of different 1-D MnO_2 nanostructures.

The crystal phase of 1-D MnO_2 nanostructures synthesized at different reaction times was investigated by their XRD patterns as depicted in Figure 5.2. It reveals the crystallinity increases in different MnO_2 nanostructures with reaction time from 8 to 12 h. The 1-D MnO_2 nanostructure developed at 8 (Mn 8 h), 10 (Mn 10 h), and 12 (Mn 12 h) exhibited different diffraction peaks at 2θ ~12.78, 18.10, 28.80, 37.52, 41.22, 41.96, 47.37, 56.92, 60.27, 65.10, 69.71, and 72.71° corresponding to the (110), (200), (310), (211), (420), (301), (510), (431), (521), (002), (541), and (312) lattice planes, respectively. It matched with α-MnO_2 (ICDD-

JCPDS No. 04-0141) having a tetragonal unit cell with a=b=9.78 *Å* and c=2.86 *Å*.[15] It was found that the reaction time from 8 to 12 h causes the narrower as well as sharper peaks. The XRD peak of the (310) lattice plane steadily converts to a stronger and narrower one by increasing the reaction period from 8 to 12 h. This demonstrated the formation of the α-MnO_2 along with the growth of the (310) plane direction. It was demonstrated that the ratio of the length to the diameter, i.e., the aspect ratio of MnO_2 nanostructures, increases with the reaction time. The specific surface area for prepared materials was assessed through BET analysis and observed 34, 16, and 3 m^2/g for Mn 8 h, Mn 10 h, and Mn 12 h, respectively (Figure 5.3(a)) (Table 5.1).

Table 5.1: Specific surface area, total pore volume, and mean pore diameter of different aspect ratios of 1-D MnO_2 nanostructures.

Sample	**Specific surface area (m^2g^{-1})**	**Total pore volume (cm^3g^{-1})**	**Mean pore diameter (nm)**
Mn 8 h	34	0.670	70.52
Mn 10 h	16	0.210	42.92
Mn 12 h	3	0.038	24.00

The MnO_2 nanowires formed at 8h showed the highest surface area as they had the highest aspect ratio. Therefore, the morphology and the specific surface area of 1-D MnO_2 nanostructures were dependent upon the reaction time and might have an impact on the sensing of GSH. TEM images depicted the shape and size of the N, S-Cdots, and their lattice spacing was examined through HRTEM image. TEM images (Figure 5.3(b, c)) of N, S-Cdots demonstrated the particles uniform distribution as well its quasi-spherical shape. Lattice spacing for N, S-Cdots was found to be 0.224 nm, which refers to (100) lattice spacing of graphitic carbon (inset image of Figure 5.3(b)).[16] The particle size histogram distribution for N, S-Cdots is displayed in the inset of Figure 5.3(c), which shows a particle size of the order of 2.5 to 6.5 nm (avg. dia. 4.5 nm).

The functional groups present on the surface of N, S-Cdots were analysed by FTIR spectra as shown in Chapter 4 (Figure 4.4(a). It depicts the presence of hydroxyl, carboxyl, thiol, and amine groups present on the surface of prepared Cdots. The N, S-Cdots were synthesized by using CA as a carbon source and cysteine as a nitrogen and sulfur source through high-temperature treatment. The preparation method of N, S-Cdots includes the condensation of CA + cysteine and further carbonization. The chemical state of N, S-Cdots and

their surface composition were investigated by XPS spectra reported in Chapter 4 (Figure 4.6) showing the presence of O1s, N1s, C1s, and S2p, respectively.

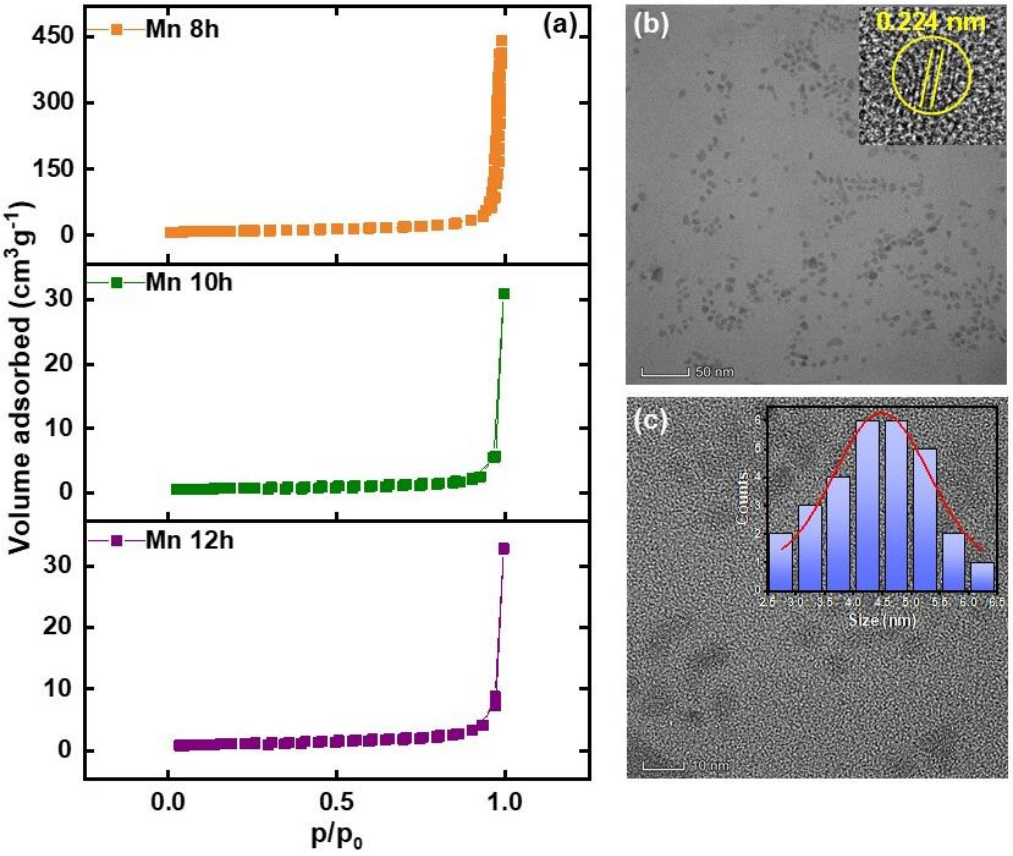

Figure 5.3. (a) BET N_2 adsorption–desorption isotherms of different MnO_2 nanostructures, (b) and (c) represent the TEM image of N, S-Cdots, inset image of (b) shows the lattice spacing of N, S-Cdots, inset image of (c) shows histogram distribution of different particle sizes of N, S-Cdots.

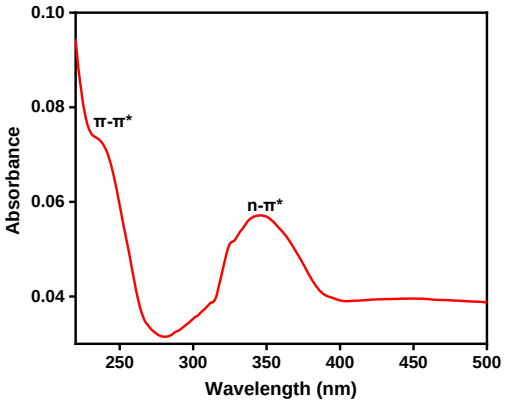

Figure 5.4. UV-vis absorption spectrum of prepared N, S-Cdots.

5.3.2 Optical properties

Figure 5.4 displays the UV-visible absorption spectrum of synthesized N, S-Cdots. The UV-visible spectrum showed a dual peak; one peak at 245 nm representing the π-π* transition corresponds to sp^2 aromatic domains, and the other one at 340 nm representing the n-π* transition corresponds to the C=O functional group. The introduction of different emissive traps and the surface passivation defects because of various functional groups present in the heteroatom-doped Cdots resulted in the modification of the PL properties.[23] N, S-Cdots showed a maximum fluorescence intensity at 427 nm with an excitation wavelength (λ_{ex}) of 340 nm. The synthesized N, S-Cdots showed a high quantum yield value of 73.42 % by using equation (1.1).

5.3.3 Fluorescence quenching of N, S-Cdots by different 1-D MnO_2 nanostructures

The fluorescent behavior of N, S-Cdots was observed to be reduced with the gradual addition of different nanostructures of 1-D MnO_2, i.e., Mn 8 h, Mn 10 h, and Mn 12 h (Figure 5.5(a), (b), (c)). The maximum PL quenching of N, S-Cdots was observed for Mn 8 h with concentrations ranging from 2 to 20 µM (Figure 5.5(a)).

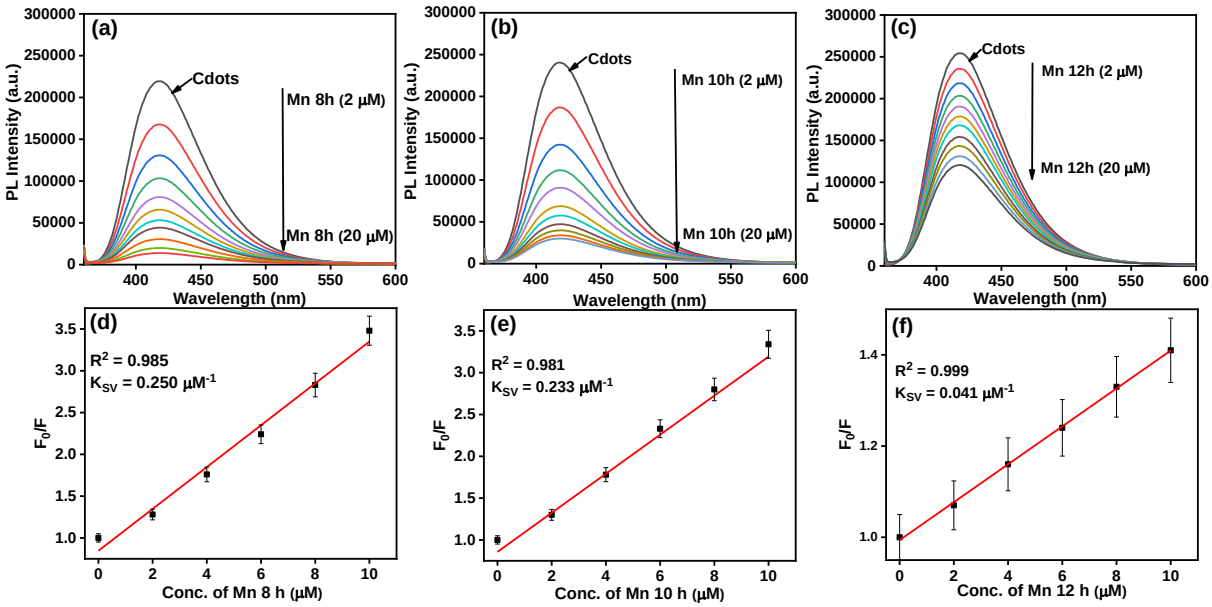

Figure 5.5. Fluorescence quenching spectra of N, S-Cdots in the presence of the successive amount of (a) Mn 8h, (b) Mn 10h, and (c) Mn 12h, and Stern-Volmer quenching plot of (d) Mn 8h, (e) Mn 10h, and (f) Mn 12h with N, S-Cdots.

The quenching efficiency of the Cdots with the addition of different 1-D MnO_2 nanostructures was investigated by using the Stern-Volmer equation (1.4). Figure 5.5(d) shows

the Stern-Volmer plot between PL intensity (F_0/F) and various concentrations of Mn 8 h, and from their values of slopes, the K_{SV} value were estimated for Mn 8 h, i.e., 0.250 μM^{-1}. Similarly, the plots between PL intensity (F_0/F) and concentrations of different Q, i.e., Mn 10 h, and Mn 12 h are displayed in Figure 5.5(e) and 5.5(f), respectively. The K_{SV} values were evaluated to be 0.233 μM^{-1} and 0.041 μM^{-1} for Mn 10 h and Mn 12 h, respectively. So, the rate of the quenching efficiency of N, S-Cdots follows the trend, i.e., Mn 8 h > Mn 10 h > Mn 12 h. Mn 8 h with a nanowire morphology has a high aspect ratio and a great specific surface area along with a large pore volume in comparison with other morphologies of 1-D MnO_2 nanostructures (Table 5.1). Therefore, it can be demonstrated that the change in the specific surface areas, aspect ratio, and the morphologies of MnO_2 nanostructures shows a great part in the PL quenching efficiency of N, S-Cdots.

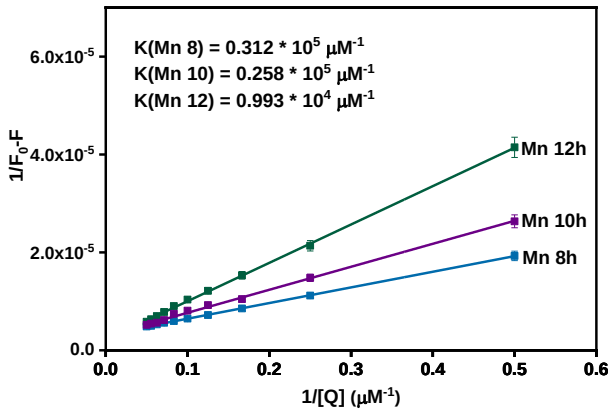

Figure 5.6. The B-H binding plot of different MnO_2 nanostructures with N, S-Cdots.

Furthermore, to understand the exact stoichiometry and interactions between the N, S-Cdots, and different 1-D MnO_2 nanostructures, the values of the binding constant in the excited state were evaluated by using the 1:1 linear Benesi−Hildebrand equation (1.5) in which different 1-D MnO_2 nanostructures (i.e., Mn 8h, Mn 10h, and Mn 12h) act as quencher. A linear plot among ($1/F-F_0$) and 1/[Q] for all morphologies of 1-D MnO_2 nanostructure was observed (Figure 5.6). These plots were used to evaluate the binding constants (K) for N, S-Cdots that are 0.312 $\times 10^5$, 0.258 $\times 10^5$, and 0.993 $\times 10^4$ μM^{-1} with the addition of Mn 8 h, Mn 10 h, and Mn 12 h, respectively. It was found that the values of the binding constant steadily reduce as the morphologies and aspect ratio of 1-D MnO_2 nanostructures decrease from Mn 8 h to Mn 12 h. Thus, it can be concluded that the change in the morphologies of 1-D MnO_2 nanostructures, played a great role in the interaction or electron transfer of N, S-Cdots and MnO_2 nanostructure which further led to the change in the binding constant of N, S-Cdots. Mn

8 h represented the maximum binding constant value for N, S-Cdots owing to a high number of surface-active sites, a great specific surface area, and a high aspect ratio in comparison with other morphologies of 1-D MnO_2 nanostructures. Further, the exact PL quenching mechanism followed by the as-prepared N, S-Cdots-MnO_2 nanostructure sensing system was also explored in detail. There are generally different PL quenching mechanisms of carbon dots on which it depends, i.e., static or dynamic quenching, IFE, FRET, and PET.[4,26]

Generally, the ground-state complex formation leads to the occurrence of static quenching with the variation of UV-visible absorption spectra of fluorescent material while no change in the decay time has observed due to the presence of an analyte.[27,28] However, the change in the decay time of the fluorescent material with the addition of a quencher results in dynamic quenching. Further, PET is a redox process in which fluorescence quenching occurs when a molecule can accept or donate the electrons of fluorescent material present in the excited state.[4] Furthermore, the IFE and FRET quenching mechanisms depend upon the transfer of energy, but they still have many significant differences.[29] FRET arises due to effective spectral overlap between the PL emission spectrum of the fluorescent material (donor) and the UV-visible spectra of the quencher (acceptor).[30] There must have appropriate dipole-dipole interactions among donor and acceptor, as well as the separation between them, should be less than 10 nm.[4]

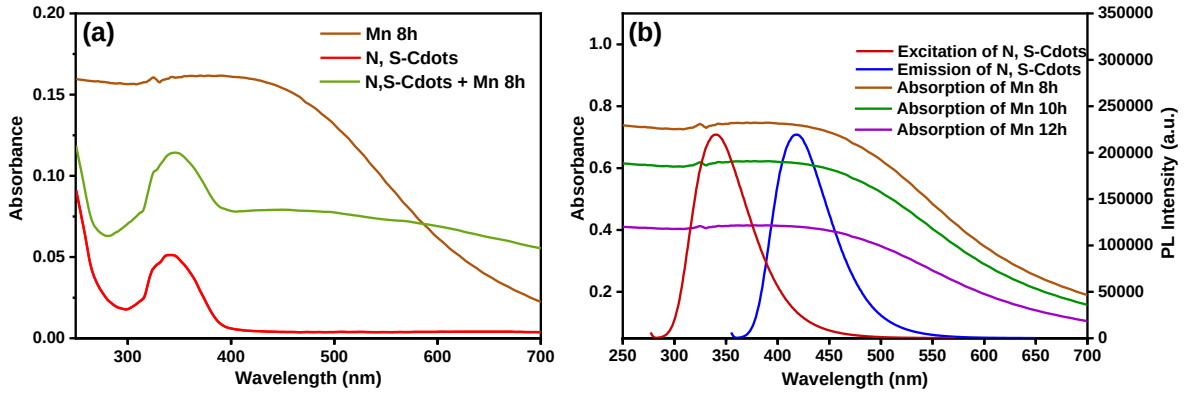

Figure 5.7 (a) UV-visible absorption spectrum of N, S-Cdots, MnO_2 nanostructure, and N, S-Cdots in the presence of MnO_2 nanostructure and (b) spectral overlap between the PL emission/excitation spectra of N, S-Cdots with absorption spectra of different 1-D MnO_2 nanostructures (Mn 8h, Mn 10h, and Mn 12h).

In the case of IFE, there is significant spectral overlap among the UV-Visible absorption spectra of the quencher and the excitation and/or emission band of the fluorescent material.[31]

Mostly, the IFE-based sensing platform does not involve covalent bonding or intermolecular interactions among the fluorescent material and the quencher.[27] The distance between the fluorescent material and the quencher must be greater than 10 nm; thus, the FRET between them is not possible. Significantly, the IFE cannot relate to the static or dynamic quenching. Therefore, it becomes very important to conclude the exact quenching mechanism followed by a prepared sensing system. To infer the quenching mechanism, UV–vis absorption spectra and PL emission spectra were measured (Figure 5.7(a) & (b)). The effective spectral overlap of the broad UV-visible absorption spectra of different MnO_2 nanostructures with the excitation/emission spectra of N, S-Cdots is shown in Figure 5.7(b). Therefore, the chances of the IFE mechanism of N, S-Cdots is maximum in Mn 8 h, and it follows the order Mn 8 h>Mn 10 h> Mn 12 h. However, at the same time, one can conclude that the FRET mechanism is also possible, which occurs due to the spectral overlap among the emission spectrum of carbon dots and the absorption spectrum of the quencher.[32]

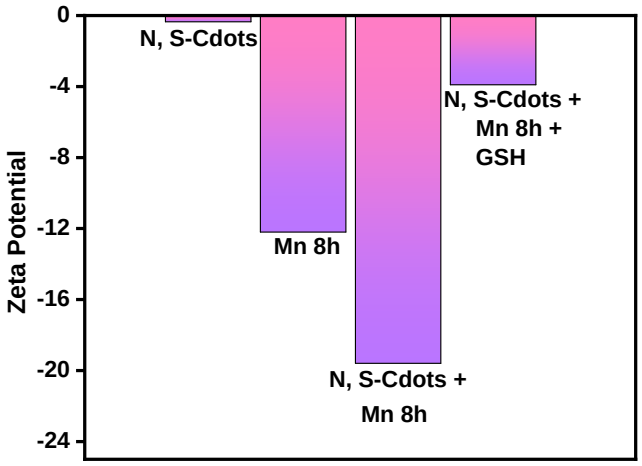

Figure 5.8. Zeta potentials of N, S-Cdots, Mn 8h, N, S-Cdots-Mn 8h, and N, S-Cdots-Mn 8h in the presence of GSH.

To understand the proper mechanism between the IFE and FRET, the zeta potential values were also evaluated which are -0.3 and -12.2 mV for N, S-Cdots and Mn 8 h, respectively (Figure 5.8, Table 5.2). Thus, the adsorption of Mn 8 h on the surface of the N, S-Cdots via electrostatic interactions might not occur due to the existence of negative charge on both of them. This demonstrates that the FRET quenching mechanism is not possible between them.[26,33] Furthermore, the fluorescence decay time studies were also performed to infer the exact mechanism. It was observed there has no significant effect in the PL lifetime of N, S-Cdots with the addition of Mn 8 h.

Table 5.2. The values of quantum yield and zeta potential of different systems.

System	Zeta Potential
N, S-Cdots	-0.3
N, S-Cdots + Mn 8h	-19.6
N, S-Cdots +Mn 8h + GSH	-3.9
Mn 8h	-12.2
N, S-Cdots + Mn 10h	-18.8
N, S-Cdots + Mn10h + GSH	-7.8
Mn 10h	-17.5
N, S-Cdots + Mn 12h	-19.0
N, S-Cdots + Mn 12h + GSH	-12.2
Mn 12h	-23.7

Table 5.3. The different parameters for the estimation of IFE on the PL quenching of N, S-Cdots by Mn 8h.[g]

Mn 8h (μM)	A_{ex}	A_{em}	CF	F_{obsd}	F_{cor}	E_{obsd}	E_{cor}	$F_{cor}/F_{cor,0}$
0	0.050	0.004	1.060	219185	232336.100	0.000	0	1
2	0.144	0.101	1.301	168421	219115.721	0.231	0.056	0.94
4	0.260	0.223	1.671	129796	216889.116	0.407	0.066	0.93
6	0.362	0.329	2.067	103310	213541.770	0.528	0.080	0.92
8	0.491	0.457	2.673	81239	217151.847	0.629	0.065	0.93
10	0.621	0.585	3.435	65789	225985.215	0.699	0.027	0.97

[g]Experimental error ±5 %

Furthermore, to clarify the IFE process the Parker equation (1.12) was used.[4] The study of various parameters by using Parker equation for the validation of the IFE was examined and is tabulated in Table 5.3. The ratio of F_{cor}/F_{obsd} is denoted as the CF. The CF values were evaluated at various concentrations of Mn 8 h. It was found that the CF value enhances with Mn 8 h (Figure 5.9(a)), and this result follows the Parker equation (1.12). This demonstrated that the IFE quenching mechanism was followed by the prepared sensing system. The suppressed efficiency for the PL emission of N, S-Cdots with the addition of Mn 8 h was estimated by a PL spectrophotometer, and further, the corresponding corrected values were explored (Figure

5.9(b)). The value of E was examined via the equation $E = 1-F/F_0$, where F_0 and F are the PL intensities of N, S-Cdots without and with the addition of Mn 8 h, respectively. It demonstrated that the IFE has a great influence in suppressing the fluorescent behavior of N, S-Cdots. Also, the maximum spectral overlap among the excitation or emission spectra of N, S-Cdots and the absorption spectra of Mn 8 h was observed as compared to Mn 10 h and Mn 12 h. This shows that the rate of the IFE could be maximum for Mn 8 h in comparison with other MnO_2 nanostructures.

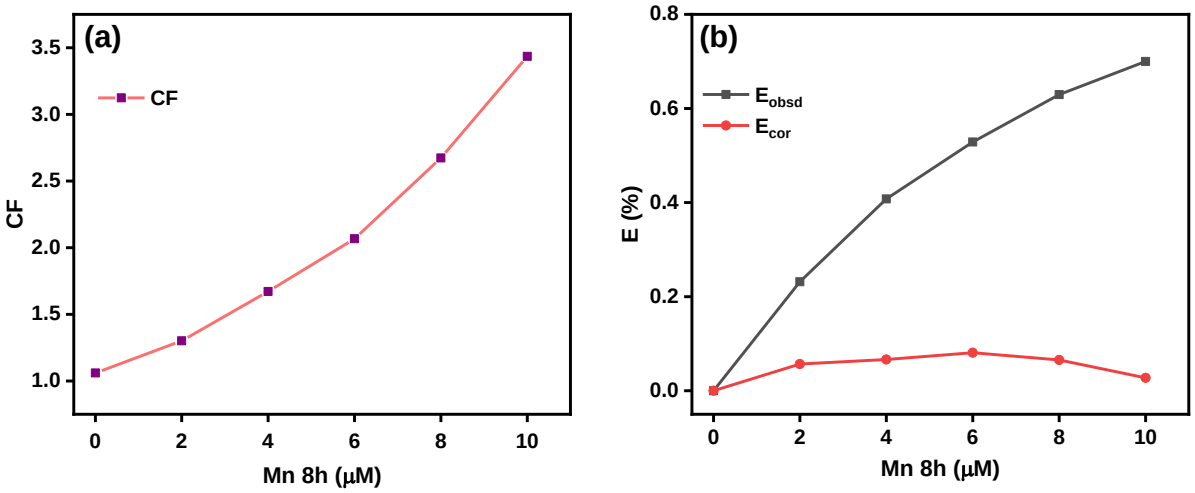

Figure 5.9. (a) The plot among the correction factor (CF) and various concentrations of Mn 8h and (b) observed suppressed efficiency (E_{obsd}) and corrected suppressed efficiency by eliminating IFE (E_{cor}) with the addition of Mn 8h.

5.3.4 Restoration mechanism of Cdots and detection of GSH

The quenched PL intensity of N, S-Cdots was restored with GSH concentration to the prepared sensing systems. The different concentrations (50-250 µM) of GSH were added to different sensing systems based on the N, S-Cdots, and different morphologies of 1-D MnO_2 nanostructures, i.e., Mn 8 h, Mn 10 h, and Mn 12 h, has demonstrated in Figure 5.10 (a), (b), and (c), respectively. The recovery of PL intensity of N, S-Cdots enhances by increasing the concentrations of GSH in the developed sensing platforms. It was observed that Mn 8 h presents the maximum fluorescence recovery of N, S-Cdots as compared to other prepared MnO_2 nanostructures. The fluorescence restoration of N, S-Cdots depends upon the redox reaction among MnO_2 nanostructures and GSH in which MnO_2 gets reduced to Mn^{2+} while GSH gets oxidized to GSH di-sulfide as presented in the equation (2.1). This displays the exclusion of N, S-Cdots from the high surface of the different 1-D MnO_2 nanostructures, which results in restoration of the PL intensity of N, S-Cdots.

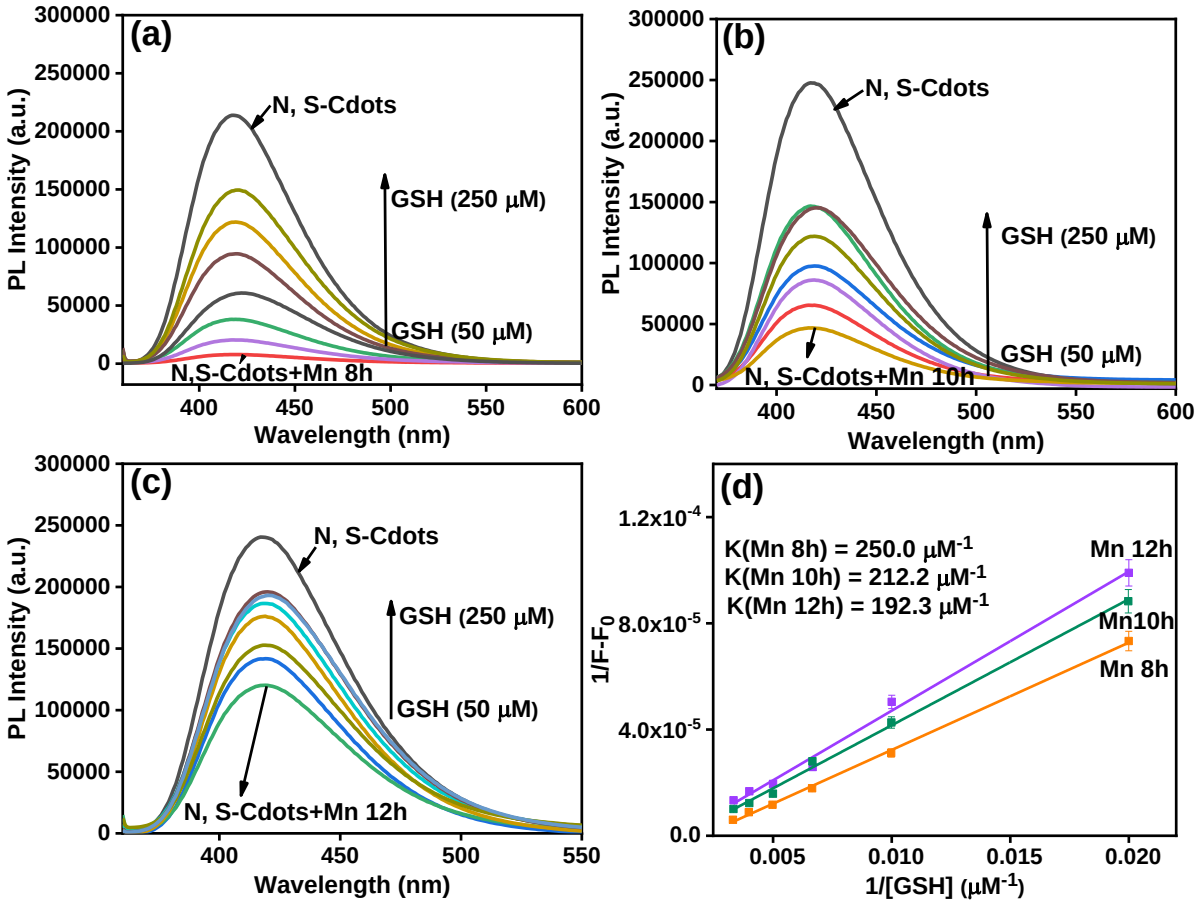

Figure 5.10. PL restoration of (a) N, S-Cdots-Mn 8h, (b) N, S-Cdots-Mn 10h, and (c) N, S-Cdots-Mn 12h sensing systems with addition of varying GSH concentration (50 - 250 μM) and (d) The B-H binding plot of MnO_2 nanostructures with different aspect ratio in the presence of GSH.

To study the interaction between N, S-Cdots-MnO_2 nanostructure as a fluorescent probe and GSH, they were investigated via the Benesi-Hildebrand method.[35] The addition of GSH to the prepared system significantly varies the binding constant values for N, S-Cdots, which are 250.0, 212.2, and 192.3 μM^{-1} in the case of Mn 8 h, Mn 10 h, and Mn 12 h, respectively (Figure 5.10(d)). It was observed that the binding constants get reduced with the addition of GSH, which shows that the N, S-Cdots get eliminated from the surface of MnO_2 nanostructures and follow the trend Mn 8 h > Mn 10 h > Mn 12 h. Among the three different MnO_2 nanostructures, Mn 8 h showed a maximum restoration of PL intensity of N, S-Cdots with the addition of GSH because of having large surface area. The variation of the morphology of different MnO_2 nanostructures in prepared sensing systems has an impact on the PL recovery of N, S-Cdots.

For investigating selectivity of N, S-Cdots-MnO_2 nanostructures, different amino acids like Asp, Lys, Gly, Arg, Cys, glutamic acid (Glu), Met, Leu, AA, His, Val, Trp, GSH were used. A particular concentration of the above amino acids was added to the developed sensing

platform. It was observed that the developed sensor had a great selectivity for GSH in comparison with other amino acids (Figure 5.11(a)). The prepared sensor showed high selectivity and sensitivity for GSH as compared to other sensing probes based on the different detection methods (Table 1.1). Figure 5.11(b) shows a straight line between the $F\text{-}F_0/F_0$ (PL responses of developed sensing platform) and various concentrations within the range of 0 to 250 µM with $F\text{-}F_0/F_0 = 0.053[GSH]\text{-}0.490$ linear equation and $R^2 = 0.992$. The limit of detection (LOD) was evaluated to be 28.5 µM. Similarly, a linear plot between the $F\text{-}F_0/F_0$ and the different concentrations (0-250 µM) was observed for Mn 10 h (Figure 5.11(c)) and Mn 12 h (Figure 5.11(d)). The developed N, S-Cdots-Mn 8 h system exhibited great selectivity for GSH sensing. The prepared sensing system is efficient in comparison with sensors based on the different methods reported in the literature (Table 1.1).

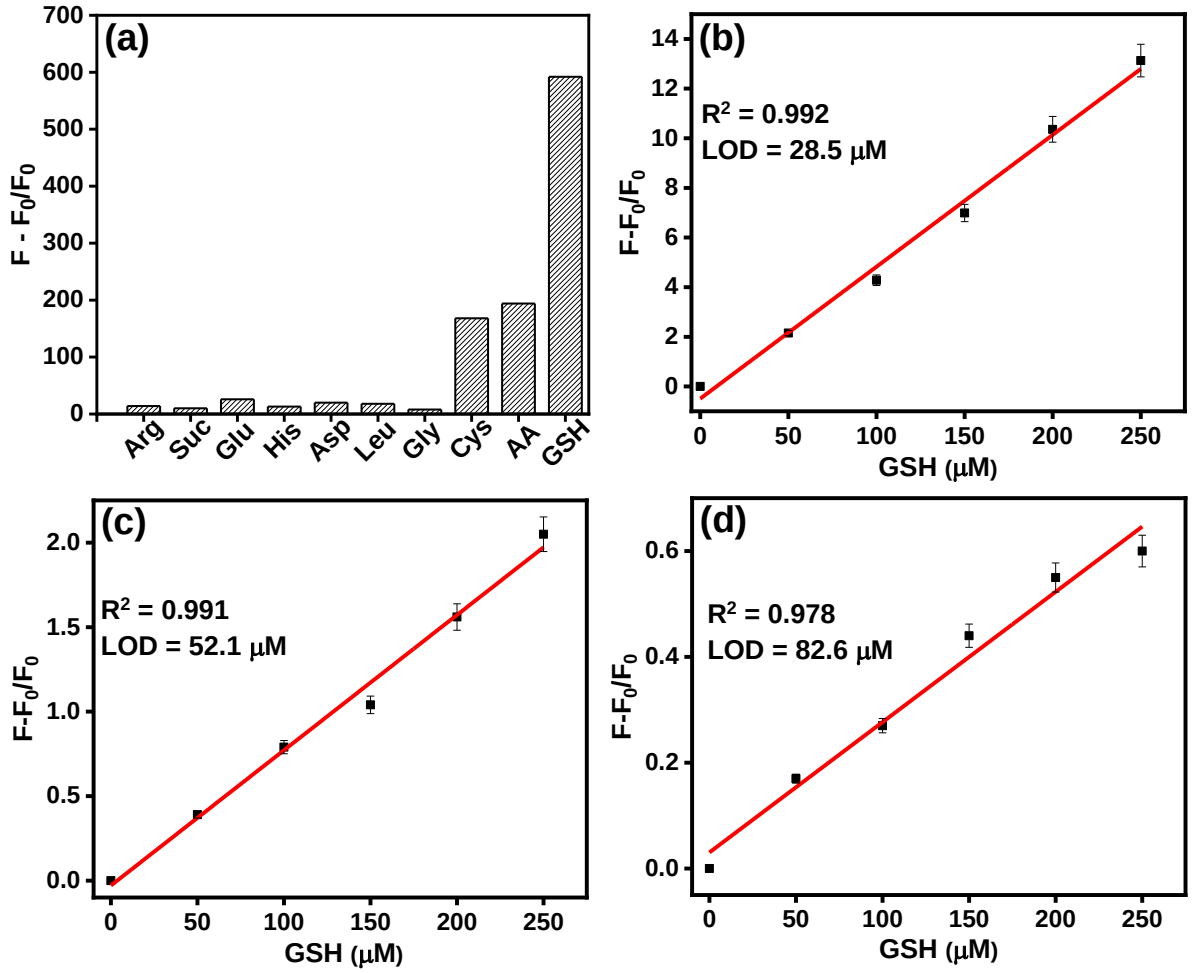

Figure 5.11. (a) The PL responses of the N, S-Cdots-MnO_2 nanostructure as sensor with the addition of several analytes and plot between PL responses ($F\text{-}F_0/F_0$) of prepared different sensing probes (b) N, S-Cdots-Mn 8h, (c) N, S-Cdots-Mn 10h, (d) N, S-Cdots-Mn 12h with various concentrations of GSH.

5.3.5 Fluorescence quantum yield measurements

The Φ values for N, S-Cdots with the addition of different 1-D MnO_2 nanostructures were also examined (Table 5.4). The change in morphology of 1-D MnO_2 nanostructures from Mn 8 h to Mn 12 h resulted in the reduction of Φ values ~7.2, ~4.5, and ~2.6 times for Mn 8 h, Mn 10 h, and Mn 12 h, respectively. The fluorescence quenching of N, S-Cdots depends upon the following order, i.e., Mn 8 h > Mn 10 h > Mn 12 h. Therefore, Mn 8 h showed a maximum fluorescence quenching of N, S-Cdots as compared to other MnO_2 nanostructures. The Φ values for different sensing systems with the addition of GSH were also estimated (Table 5.4). For a different morphology of 1-D MnO_2 nanostructures, the value of Φ was recovered in the presence of particular amounts of GSH that are ~5.0, ~2.8, and ~1.4 times for Mn 8 h, Mn 10 h, and Mn 12 h, respectively. The fluorescence restoration of N, S-Cdots follows the trend Mn 8 h > Mn 10 h > Mn 12 h. This demonstrated that the variation in the aspect ratio of 1-D MnO_2 nanostructure from Mn 8 h to Mn 12 h in N, S-Cdots-MnO_2 sensing probe leads to less significant removal of N, S-Cdots from the surface of 1-D MnO_2 nanostructures. Therefore, Mn 8h and GSH showed a strong redox reaction between them in comparison with other MnO_2 nanostructures.

Table 5.4. The values of quantum yield of different systems.

System	Quantum Yield (%)
N, S-Cdots	73.4
N, S-Cdots + Mn 8h	10.1
N, S-Cdots +Mn 8h + GSH	51.4
Mn 8h	-
N, S-Cdots + Mn 10h	16.3
N, S-Cdots + Mn10h + GSH	45.7
Mn 10h	-
N, S-Cdots + Mn 12h	27.7
N, S-Cdots + Mn 12h + GSH	38.4
Mn 12h	-

[h]Experimental error ±5 %

Conclusion

The as-prepared N, S-Cdots showed high water solubility, excellent quantum yield, and significant fluorescence properties. Further, N, S-Cdots were used as a fluorescent material in

the presence of 1-D MnO_2 nanostructures for the detection of GSH. The different morphologies of 1-D MnO_2 nanostructures were prepared by using a hydrothermal method by varying the reaction time (8, 10, and 12 h). The variations in the morphology and the aspect ratio of the different 1-D MnO_2 nanostructures were determined by TEM images. The surface area of different 1-D MnO_2 nanostructures was estimated by BET and shows the following trend in the surface area: Mn 8 h > Mn 10 h > Mn 12 h. Mn 8 h had a nanowire-like morphology along with a large specific surface area, a high surface-to-volume ratio, and a high aspect ratio, which will make it a better quencher as compared to other morphologies. Further, Mn 8 h exhibited maximum fluorescence quenching of N, S-Cdots and a large Stern-Volmer quenching constant (K_{SV}) value attributed to the specific surface area. The values of fluorescence quenching, Stern-Volmer constants, binding constants, and quantum yields for different MnO_2 nanostructures showed that Mn 8 h was the best fluorescence quencher for N, S-Cdots. The quenching mechanism between the N, S-Cdots and 1-D MnO_2 nanostructures was the IFE, which was confirmed by using the Parker equation, UV−vis absorption studies, and lifetime studies. The developed sensing platform displayed the fluorescence restoration of N, S-Cdots based on the redox reaction among GSH and MnO_2, which resulted in the transformation of MnO_2 to Mn^{2+}. The lowest value of the limit of detection, i.e., 28.5 μM, for GSH was determined for N, S-Cdots-Mn 8h sensing platform. Thus, the change in the morphology of 1-D MnO_2 nanostructures in the prepared sensor plays a great role in the determination of GSH.

References

(1) Wang, Y.; Kim, S.-H.; Feng, L. Highly Luminescent N, S- Co-Doped Carbon Dots and Their Direct Use as Mercury(II) Sensor. *Anal. Chim. Acta* **2015**, *890*, 134–142. https://doi.org/10.1016/j.aca.2015.07.051.

(2) Zhang, Y.-Q.; Ma, D.-K.; Zhuang, Y.; Zhang, X.; Chen, W.; Hong, L.-L.; Yan, Q.-X.; Yu, K.; Huang, S.-M. One-Pot Synthesis of N-Doped Carbon Dots with Tunable Luminescence Properties. *J. Mater. Chem.* **2012**, *22* (33), 16714. https://doi.org/10.1039/c2jm32973e.

(3) Li, L.; Dong, T. Photoluminescence Tuning in Carbon Dots: Surface Passivation or/and Functionalization, Heteroatom Doping. *J. Mater. Chem. C* **2018**, *6* (30), 7944–7970. https://doi.org/10.1039/C7TC05878K.

(4) Zu, F.; Yan, F.; Bai, Z.; Xu, J.; Wang, Y.; Huang, Y.; Zhou, X. The Quenching of the Fluorescence of Carbon Dots: A Review on Mechanisms and Applications. *Microchim. Acta* **2017**, *184* (7), 1899–1914. https://doi.org/10.1007/s00604-017-2318-9.

(5) Wang, Y.; Jiang, K.; Zhu, J.; Zhang, L.; Lin, H. A FRET-Based Carbon Dot–MnO_2 Nanosheet Architecture for Glutathione Sensing in Human Whole Blood Samples. *Chem. Commun.* **2015**, *51* (64), 12748–12751. https://doi.org/10.1039/C5CC04905A.

(6) Garg, D.; Mehta, A.; Mishra, A.; Basu, S. A Sensitive Turn on Fluorescent Probe for Detection of Biothiols Using MnO_2@carbon Dots Nanocomposites. *Spectrochim. Acta Part A Mol. Biomol. Spectrosc.* **2018**, *192*, 411–419. https://doi.org/10.1016/j.saa.2017.11.041.

(7) Sohal, N.; Maity, B.; Shetti, N. P.; Basu, S. Biosensors Based on MnO_2 Nanostructures: A Review. *ACS Appl. Nano Mater.* **2021**, *4* (3), 2285–2302. https://doi.org/10.1021/acsanm.0c03380.

(8) Ede, S. R. a.; Anantharaj, S.; Nithiyanantham, U.; Kundu, S. DNA-Encapsulated Chain and Wire-like β-MnO_2 Organosol for Oxidative Polymerization of Pyrrole to Polypyrrole. *Phys. Chem. Chem. Phys.* **2015**, *17* (7), 5474–5484. https://doi.org/10.1039/c4cp04236k.

(9) Shen, H.; Huang, J.; Wei, Y.; Guo, X.; Wang, M.; Wang, L. Effect of Morphology of ϵ-MnO_2 on Hydrogen Peroxide Sensing. *ChemistrySelect* **2019**, *4* (14), 4035–4043. https://doi.org/10.1002/slct.201900312.

(10) Chen, S.; Zhu, J.; Han, Q.; Zheng, Z.; Yang, Y.; Wang, X. Shape-Controlled Synthesis of One-Dimensional MnO_2 via a Facile Quick-Precipitation Procedure and Its Electrochemical Properties. *Cryst. Growth Des.* **2009**, *9* (10), 4356–4361. https://doi.org/10.1021/cg900223f.

(11) Zhao, S.; Shen, Y.; Yan, X.; Zhou, P.; Yin, Y.; Lu, R.; Han, C.; Cui, B.; Wei, D. Complex-Surfactant-Assisted Hydrothermal Synthesis of One-Dimensional ZnO Nanorods for High-Performance Ethanol Gas Sensor. *Sensors Actuators B Chem.* **2019**, *286*, 501–511. https://doi.org/10.1016/j.snb.2019.01.127.

(12) Feng, J.-J.; Zhang, P.-P.; Wang, A.-J.; Zhang, Y.; Dong, W.-J.; Chen, J.-R. One-Pot Hydrothermal Synthesis of Uniform β-MnO_2 Nanorods for Nitrite Sensing. *J. Colloid Interface Sci.* **2011**, *359* (1), 1–8. https://doi.org/10.1016/j.jcis.2011.03.087.

(13) Liu, Y.; Chi, X.; Han, Q.; Du, Y.; Huang, J.; Liu, Y.; Yang, J. α-MnO_2 Nanofibers/Carbon Nanotubes Hierarchically Assembled Microspheres: Approaching Practical Applications of High-Performance Aqueous Zn-Ion Batteries. *J. Power Sources* **2019**, *443*, 227244. https://doi.org/10.1016/j.jpowsour.2019.227244.

(14) Yang, J.; Wang, J.; Ma, S.; Ke, B.; Yu, L.; Zeng, W.; Li, Y.; Wang, J. Insight into the Effect of Crystalline Structure on the Oxygen Reduction Reaction Activities of One-

Dimensional MnO_2. *Phys. E Low-dimensional Syst. Nanostructures* **2019**, *109*, 191–197. https://doi.org/10.1016/j.physe.2018.07.032.

(15) Su, D.; Ahn, H.-J.; Wang, G. Hydrothermal Synthesis of α-MnO_2 and β-MnO_2 Nanorods as High Capacity Cathode Materials for Sodium Ion Batteries. *J. Mater. Chem. A* **2013**, *1* (15), 4845. https://doi.org/10.1039/c3ta00031a.

(16) Arul, V.; Edison, T. N. J. I.; Lee, Y. R.; Sethuraman, M. G. Biological and Catalytic Applications of Green Synthesized Fluorescent N-Doped Carbon Dots Using Hylocereus Undatus. *J. Photochem. Photobiol. B Biol.* **2017**, *168*, 142–148. https://doi.org/10.1016/j.jphotobiol.2017.02.007.

(17) Bu, L.; Luo, T.; Peng, H.; Li, L.; Long, D.; Peng, J.; Huang, J. One-Step Synthesis of N-Doped Carbon Dots, and Their Applications in Curcumin Sensing, Fluorescent Inks, and Super-Resolution Nanoscopy. *Microchim. Acta* **2019**, *186* (10), 675. https://doi.org/10.1007/s00604-019-3762-5.

(18) Fu, Z.; He, J.; Jia, F.; Wang, M.; Cui, F. Utilizing the Interfacial Reaction of Naphthalenyl Thiosemicarbazide-Modified Carbon Dots for the Ultrasensitive Determination of Fe (III) Ions. *Spectrochim. Acta Part A Mol. Biomol. Spectrosc.* **2020**, *225*, 117485. https://doi.org/10.1016/j.saa.2019.117485.

(19) Liu, Y.; Zhu, C.; Gao, Y.; Yang, L.; Xu, J.; Zhang, X.; Lu, C.; Wang, Y.; Zhu, Y. Biomass-Derived Nitrogen Self-Doped Carbon Dots via a Simple One-Pot Method: Physicochemical, Structural, and Luminescence Properties. *Appl. Surf. Sci.* **2020**, *510*, 145437. https://doi.org/10.1016/j.apsusc.2020.145437.

(20) Chen, C.; Zhao, D.; Hu, T.; Sun, J.; Yang, X. Highly Fluorescent Nitrogen and Sulfur Co-Doped Graphene Quantum Dots for an Inner Filter Effect-Based Cyanide Sensor. *Sensors Actuators B Chem.* **2017**, *241*, 779–788. https://doi.org/10.1016/j.snb.2016.11.010.

(21) Wang, Z.; Liao, H.; Wu, H.; Wang, B.; Zhao, H.; Tan, M. Fluorescent Carbon Dots from Beer for Breast Cancer Cell Imaging and Drug Delivery. *Anal. Methods* **2015**, *7* (20), 8911–8917. https://doi.org/10.1039/C5AY01978H.

(22) Chen, X.; Wang, X.; Fang, D. A Review on C1s XPS-Spectra for Some Kinds of Carbon Materials. *Fullerenes, Nanotub. Carbon Nanostructures* **2020**, *28* (12), 1048–1058. https://doi.org/10.1080/1536383X.2020.1794851.

(23) Cui, X.; Wang, Y.; Liu, J.; Yang, Q.; Zhang, B.; Gao, Y.; Wang, Y.; Lu, G. Dual Functional N- and S-Co-Doped Carbon Dots as the Sensor for Temperature and Fe^{3+} Ions. *Sensors Actuators B Chem.* **2017**, *242*, 1272–1280.

https://doi.org/10.1016/j.snb.2016.09.032.

(24) Mondal, J.; Revuri, V.; Choochana, P.; Ganesan, P.; Kang, W. J.; Lee, Y. Sulfur and Nitrogen Doped Carbon Quantum Dots for Detection of Glutathione and Reduction of Cellular Nitric Oxide in Microglial Cells. *J. Pharm. Investig.* **2020**, *50* (2), 209–218. https://doi.org/10.1007/s40005-019-00466-8.

(25) Zhang, Y.; He, J. Facile Synthesis of S, N Co-Doped Carbon Dots and Investigation of Their Photoluminescence Properties. *Phys. Chem. Chem. Phys.* **2015**, *17* (31), 20154–20159. https://doi.org/10.1039/C5CP03498A.

(26) Liu, J.; Chen, Y.; Wang, W.; Feng, J.; Liang, M.; Ma, S.; Chen, X. "Switch-On" Fluorescent Sensing of Ascorbic Acid in Food Samples Based on Carbon Quantum Dots–MnO_2 Probe. *J. Agric. Food Chem.* **2016**, *64* (1), 371–380. https://doi.org/10.1021/acs.jafc.5b05726.

(27) Yang, B.; Li, X.; Wang, L.; An, J.; Wang, T.; Zhang, F.; Ding, B.; Li, Y. A Water-Stable MOF-$AgClO_4$-Abtz as Fluorescent Sensor for Detection of Folic Acid Based on Inner Filter Effect. *Talanta* **2020**, *217*, 121019. https://doi.org/10.1016/j.talanta.2020.121019.

(28) Yang, B.; Li, X.; An, J.; Zhang, H.; Liu, M.; Cheng, Y.; Ding, B.; Li, Y. Designing an "Off–On" Fluorescence Sensor Based on Cluster-Based Ca^{II}-Metal–Organic Frameworks for Detection of l-Cysteine in Biological Fluids. *Langmuir* **2019**, *35* (30), 9885–9895. https://doi.org/10.1021/acs.langmuir.9b01479.

(29) Yu, X.; Zhang, C.-X.; Zhang, L.; Xue, Y.-R.; Li, H.-W.; Wu, Y. The Construction of a FRET Assembly by Using Gold Nanoclusters and Carbon Dots and Their Application as a Ratiometric Probe for Cysteine Detection. *Sensors Actuators B Chem.* **2018**, *263*, 327–335. https://doi.org/10.1016/j.snb.2018.02.072.

(30) Sohal, N.; Maity, B.; Basu, S. Carbon Dot-MnO_2 Nanosphere Composite Sensors for Selective Detection of Glutathione. *ACS Appl. Nano Mater.* **2020**, *3* (6), 5955–5964. https://doi.org/10.1021/acsanm.0c01088.

(31) Chen, S.; Yu, Y.-L.; Wang, J.-H. Inner Filter Effect-Based Fluorescent Sensing Systems: A Review. *Anal. Chim. Acta* **2018**, *999*, 13–26. https://doi.org/10.1016/j.aca.2017.10.026.

(32) Dong, W.; Wang, R.; Gong, X.; Dong, C. An Efficient Turn-on Fluorescence Biosensor for the Detection of Glutathione Based on FRET between N, S Dual-Doped Carbon Dots and Gold Nanoparticles. *Anal. Bioanal. Chem.* **2019**, *411* (25), 6687–6695. https://doi.org/10.1007/s00216-019-02042-3.

(33) Fang, A.; Long, Q.; Wu, Q.; Li, H.; Zhang, Y.; Yao, S. Upconversion Nanosensor for

Sensitive Fluorescence Detection of Sudan I–IV Based on Inner Filter Effect. *Talanta* **2016**, *148*, 129–134. https://doi.org/10.1016/j.talanta.2015.10.048.

(34) Sohal, N.; Maity, B.; Basu, S. Morphology-Dependent Performance of MnO_2 Nanostructure–Carbon Dot-Based Biosensors for the Detection of Glutathione. *ACS Appl. Bio Mater.* **2021**, *4* (6), 5158–5168. https://doi.org/10.1021/acsabm.1c00353.

(35) Hildebrand, J. H.; Benesi, H. A. Interaction of Iodine with Aromatic Hydrocarbons [15]. *Nature* **1949**, *164* (4179), 963. https://doi.org/10.1038/164963b0.

CHAPTER-6

Transformation of Bulk MnO_2 to Fluorescent Quantum Dots for Selective and Sensitive Detection of Ferric ions and Ascorbic acid by Turn-Off-On Strategy

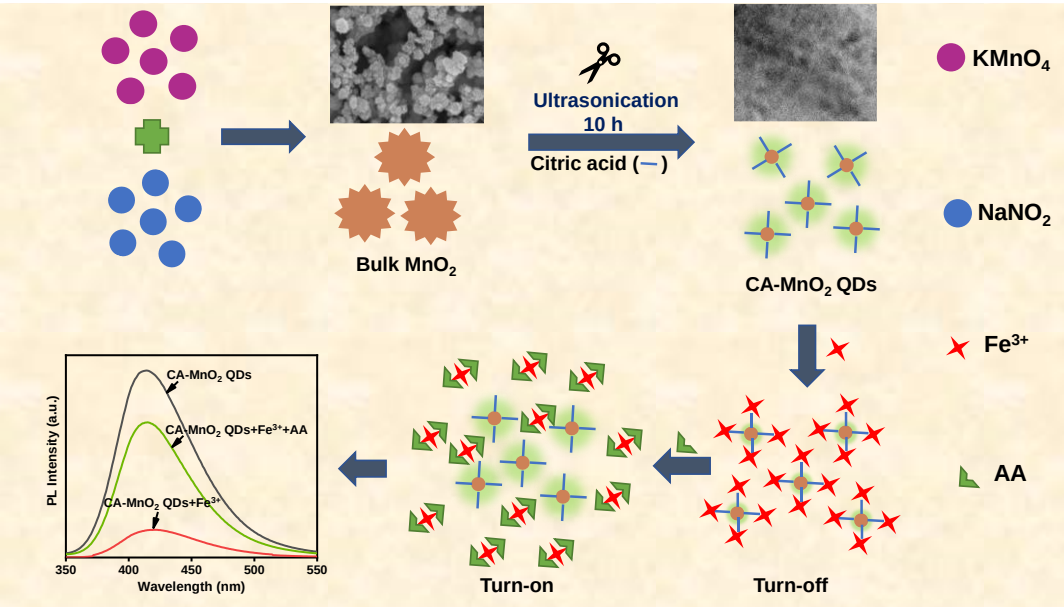

Highlights

- Synthesis of fluorescent CA-MnO_2 QDs using bulk MnO_2 and CA by simple ultrasonication.
- Synthesized QDs show high photostability, good water solubility, and highly fluorescence behaviour.
- Development of fluorescent nanosensor for the detection of Fe^{3+} ions and ascorbic acid.
- Study of different photophysical parameters to confirm dynamic quenching mechanism.
- CA-MnO_2 QDs as a nanosensor for application in real sample analysis.

6.1 Introduction

Among various inorganic materials, MnO_2 has gained large attention in different research fields such as electrocatalysis, supercapacitors, drug delivery, photothermal treatment, and optical sensing due to exceptional large charge transfer rate, high active surface area, non-toxicity, and cost-effectiveness.[1] MnO_2 has been largely used as a dynamic material for the optical sensing of biomolecules (such as GSH, AA, Cys, etc.) due to its exceptional physical, electrochemical, and optical properties.[2] The exclusive light absorption capability and redox features of MnO_2 nanostructure lead to consider it as fluorescence quenchers and further, used in the preparation of "turn off−on" fluorescence sensing probes.[3,4] The "turn off−on" biosensors for the detection of glutathione were already reported in previous chapters, based on carbon dots-MnO_2 nanostructure in which carbon dots act as a fluorescent probe and MnO_2 nanostructure act as a recognizer. The combination of fluorescent probes and MnO_2 nanostructure as sensing platforms with synergistic properties are reported in the literature for the detection of different biomolecules. These biosensors need a fluorescent probe such as carbon quantum dots, graphene quantum dots, and dyes which are highly responsible for their sensing activity. Moreover, various reductive biomolecules can be oxidized by MnO_2 nanostructure due to its oxidizing property that will confine the selectivity of sensing platforms.[5] Hence, the synthesis of a self-fluorescent MnO_2 nanomaterial with particular functional groups is highly needed.

Quantum dots (QDs) are a type of quasi-0-D semiconductor nanocrystal having a radius lesser than or near to their exciton Bohr radius.[6,7] Fluorescent QDs have several exclusive optical properties, like excellent brightness, good photostability, broad excitation spectrum, tunable fluorescence emission spectrum, nanoscale size, etc.[8,9] The luminescent quantum dots like CdSe, CdS, and CdTe QDs are reported in the literature with many practical applications due to their excellent electronic and optical properties. But these QDs are toxic, due to which they cannot be used for optical and biological detection.[10] MnO_2 QDs have good biocompatibility and a less toxic nature which makes them a good alternative for other QDs.[5]

Fluorescence detection of metal ions is one of the application that has gained significant attention.[11] Fe^{3+} ions play an essential part in various biological processes in living organisms, such as oxygen storage, development of red cells, enzyme catalysis, oxygen transportation, etc.[12] The irregular range of Fe^{3+} ions in the human body can become a reason for several diseases, for example, anaemia, malaria, cancer, Parkinson's disease, and Alzheimer's

disease.[13] Thus, the sensitive determination of Fe^{3+} ions has been seeking great attention for the safety of human health. Similarly, ascorbic acid (AA, also called vitamin C) acts as an antioxidant and also plays a significant role in different biochemical processes in living organisms and its quantitative detection is very helpful in pharmaceutical analysis.[14,15] Different methods have been reported for the detection of both metal ion and biomolecule, such as electrochemical, high-performance liquid chromatography, electrochemiluminescence, surface-enhanced Raman scattering, etc. Still, they are complicated, expensive, and lengthy detection processes. Fluorescence spectroscopy is simple, cost-effective, and very sensitive for the sensing of metal ions and biomolecules.[16]

Herein, MnO_2 QDs functionalized with citric acid (CA-MnO_2 QDs) from bulk MnO_2 were synthesized. The obtained CA-MnO_2 QDs showed high photoluminescence (PL) intensity, good water solubility, and excellent photostability. Citric acid act as an acidifying agent which helps in the exfoliation and breaking of bulk MnO_2 to MnO_2 QDs. Therefore, the presence of citric acid is responsible for the exclusive optical properties of the prepared CA-MnO_2 QDs. The PL intensity of CA-MnO_2 QDs was highly quenched in the presence of Fe^{3+} ions based on a dynamic quenching mechanism which was confirmed by determining the various photophysical parameters. Further, the PL intensity of the CA-MnO_2 QDs-Fe^{3+} system was recovered with the addition of AA based on the redox reaction.

6.2 Experimental Section

6.2.1 Material and reagents

Potassium permanganate ($KMnO_4$) (99%), sodium nitrite ($NaNO_2$) (99%), and sulfuric acid (H_2SO_4) (98%) were obtained from Loba Chemie, India, for the preparation of bulk MnO_2. For the functionalization of MnO_2 QDs, citric acid (99%), glutathione (99%), ascorbic acid (99%), and L-cysteine (99%) were used and purchased from Loba Chemie, India. Ferric nitrate ($Fe(NO_3)_3$) with 99% purity was also obtained from Loba Chemie, India. All the stock solutions were formed in the ultrapure deionized (DI) water.

6.2.2 Synthesis of bulk MnO_2

Bulk MnO_2 was synthesized by using $KMnO_4$ (5 mM) and $NaNO_2$ (7.5 mM) as precursors via mixing both in 40 ml of water. Then, the gradual addition of 2 ml of H_2SO_4 (0.5 M) in the above solution along with constant stirring was done.[17] The color of the solution changes to brown which confirms the formation of MnO_2. Further, the solution was

centrifuged, and the obtained brown precipitates were washed with water and ethanol. The final obtained product was dried in an oven at 60° C.

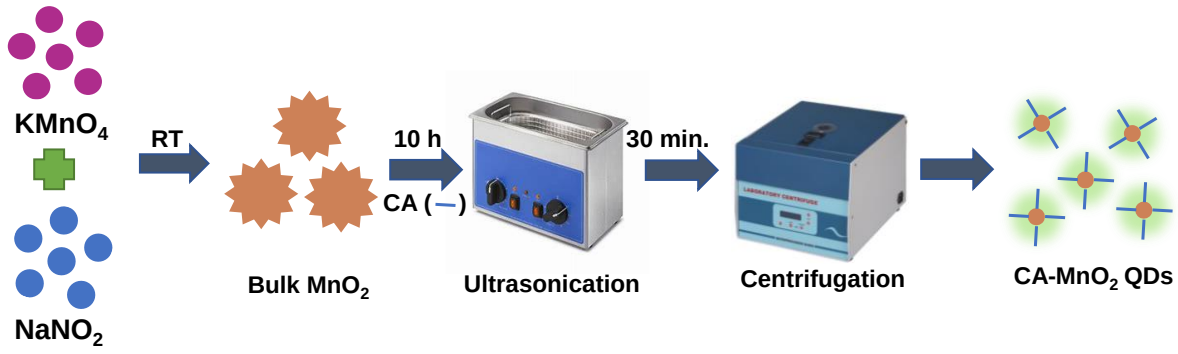

Scheme 6.1: Schematic illustration of the synthesis of citric acid functionalized MnO_2 QDs.

6.2.3 Synthesis of Citric acid-MnO_2 quantum dots (CA-MnO_2 QDs)

CA-MnO_2 QDs were prepared by using bulk MnO_2 as a precursor by using the ultra-sonication method. In detail, 10 mg of bulk MnO_2 and 10 mg of citric acid were mixed in 10 ml of distilled water. Further, the above solution was sonicated for 10 h and then centrifuged for a continuous 30 min. at 10,000 rpm and the supernatant was collected as CA-MnO_2 QDs (Scheme 6.1).

6.2.4 Characterization

The UV-visible absorption spectrum of prepared CA-MnO_2 QDs was obtained by a UV−vis spectrophotometer (Shimadzu, UV-2600). The PL emission spectra were recorded via a spectrofluorometer (Shimadzu, RF-6000). The morphology and size of bulk MnO_2 were obtained by field emission scanning electron microscopy (FESEM). The morphology, shape, and size of CA-MnO_2 QDs were obtained by TEM analysis (FEI TecnaiG2 F20). The crystal structure of the prepared CA-MnO_2 QDs was examined via XRD (PANALYTICAL X'Pert PRO) in which Cu Kα ($\lambda = 1.540^{\circ}A$) acts as a source of radiation ($0^{\circ} \leq 2\theta \leq 90^{\circ}$). Average lifetime studies were performed by TCSPC spectrometer (Horiba Jobin Yvon IBH) with an excitation laser source at 375 nm.

6.3 Result and Discussion

6.3.1 Characterization

The morphology and shape of prepared bulk MnO_2 were investigated by FESEM analysis. Figure 6.1(a, b) showed the aggregated nanowires-like morphology of bulk MnO_2. Figure 6.1(c) shows the EDS spectrum of the bulk MnO_2, which confirms the formation as well

as purity of MnO_2. Further, the prepared CA-MnO_2 QDs from bulk MnO_2 was characterized by different analysis. The morphology, shape, and size of the prepared CA-MnO_2 QDs were analyzed by using TEM analysis.

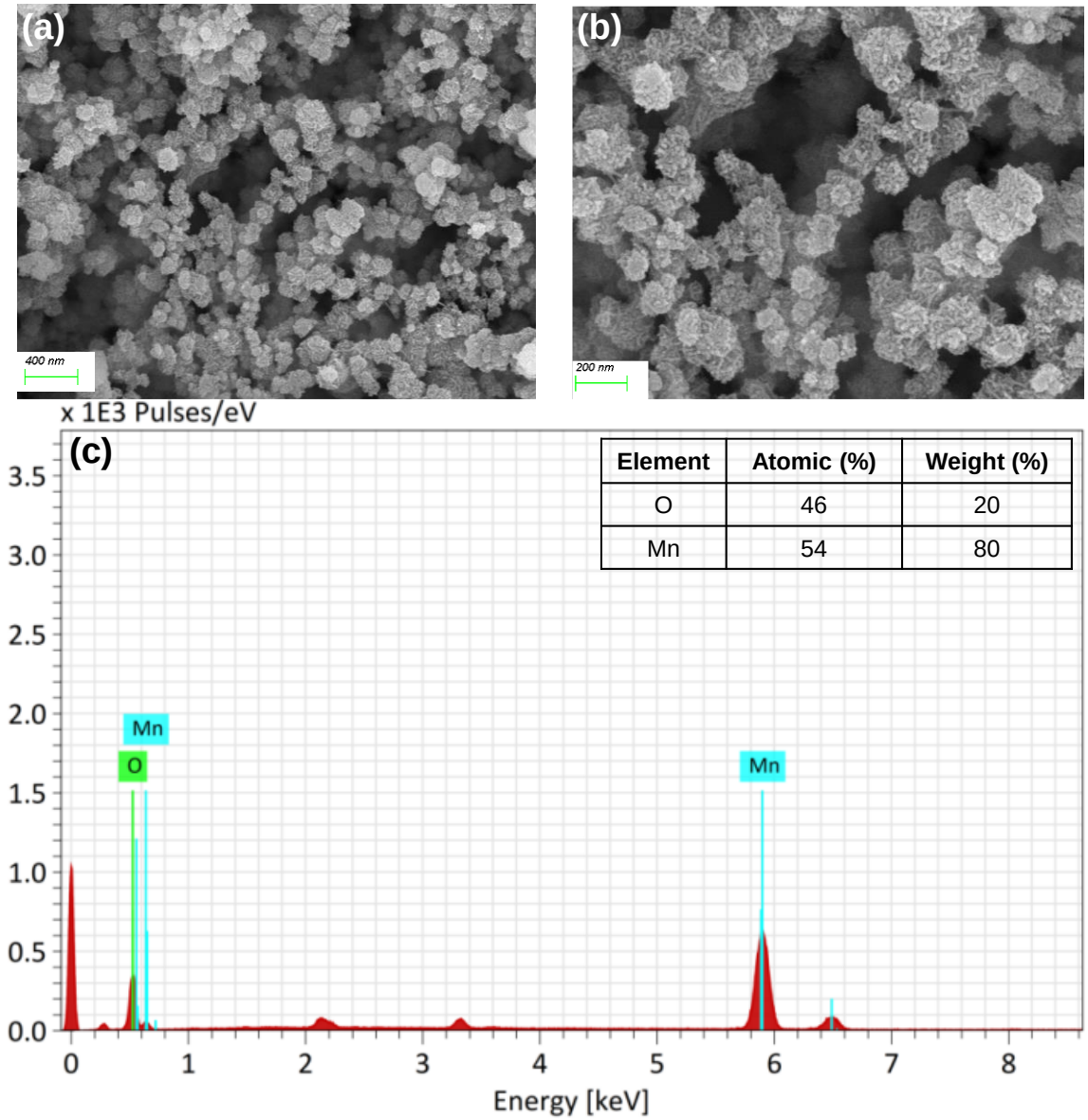

Figure 6.1: (a) and (b) shows the FESEM images of bulk MnO_2, and (c) EDS spectra of bulk MnO_2.

CA-MnO_2 QDs were developed by using bulk MnO_2 as a precursor and citric acid as an exfoliating agent through the ultra-sonication method. The preparation method of CA-MnO_2 QDs includes the exfoliation of bulk MnO_2 into QDs in the presence of citric acid, which acts as an acidifying agent and stabilizing agent.[18]

Figure 6.2(a, b) shows the TEM images of CA-MnO_2 QDs in which particles are dispersed uniformly and nearly in a spherical shape. Figure 6.2(c) shows the histogram

distribution of particle size with a range of 1 to 4 nm and the average particle size was measured to be 3.5 nm.

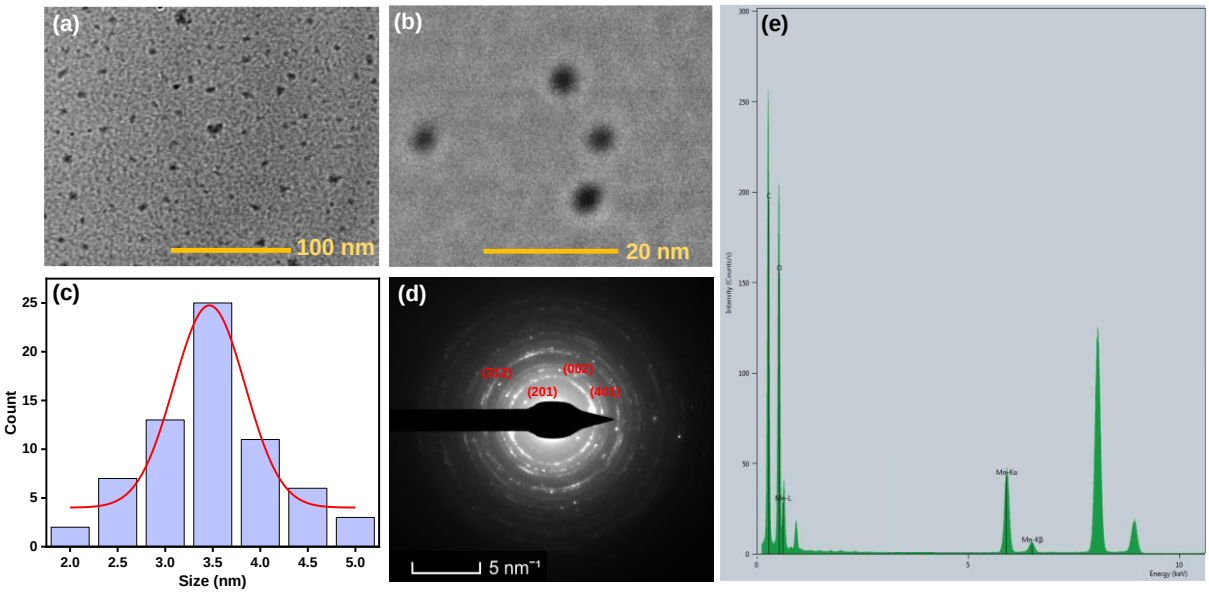

Figure 6.2: (a) and (b) represents the TEM images of CA-MnO_2 QDs and the inset image of (a) shows its lattice fringes with d-spacing value, (c) particle size distribution, (d) SAED pattern, and (e) EDS spectrum of CA-MnO_2 QDs.

Figure 6.2(d) displays the SAED ring pattern of CA-MnO_2 QDs, which shows that they are crystalline. The diameter of the diffraction rings present in the SAED pattern is related to $(h^2 + k^2 + l^2)^2$ in which (*hkl*) corresponds to Miller indices of the lattice planes, which are measured from the center of the ring. The major rings represent the (201), (401), (002), and (312) planes of MnO_2 corresponding to the ICDD-JCPDS No. 72-1983. Figure 6.2(e) shows the EDS spectra of CA-MnO_2 QDs, which exhibit the presence of Mn, O, and C elements. Figure 6.3(a) shows the XRD spectra of the prepared CA-MnO_2 QDs, which exhibit the major peaks at 36.1°, 50.5°, and 65.4° corresponding to (201), (401), and (002) planes of MnO_2 (ICDD-JCPDS No. 72-1983). A broad peak was also observed in the XRD pattern due to the overlapping of the 19.0° and 22.0° which indexed to the (200) and (110) planes of MnO_2, respectively. Further, the composition and chemical state of CA-MnO_2 QDs was confirmed by the XPS analysis. The survey spectrum of CA-MnO_2 QDs shows prominent peaks which validate the presence of C, O, and Mn (Figure 6.3(b)). Figure 6.3(c) shows two major peaks at 639.5 eV and 651.4 eV, corresponding to Mn $2p_{3/2}$ and Mn $2p_{1/2}$ and their energy gap is 11.7 eV which confirmed the formation of MnO_2. Figure 6.3(d) shows the peak at 529.9 eV attributed to the O1s.

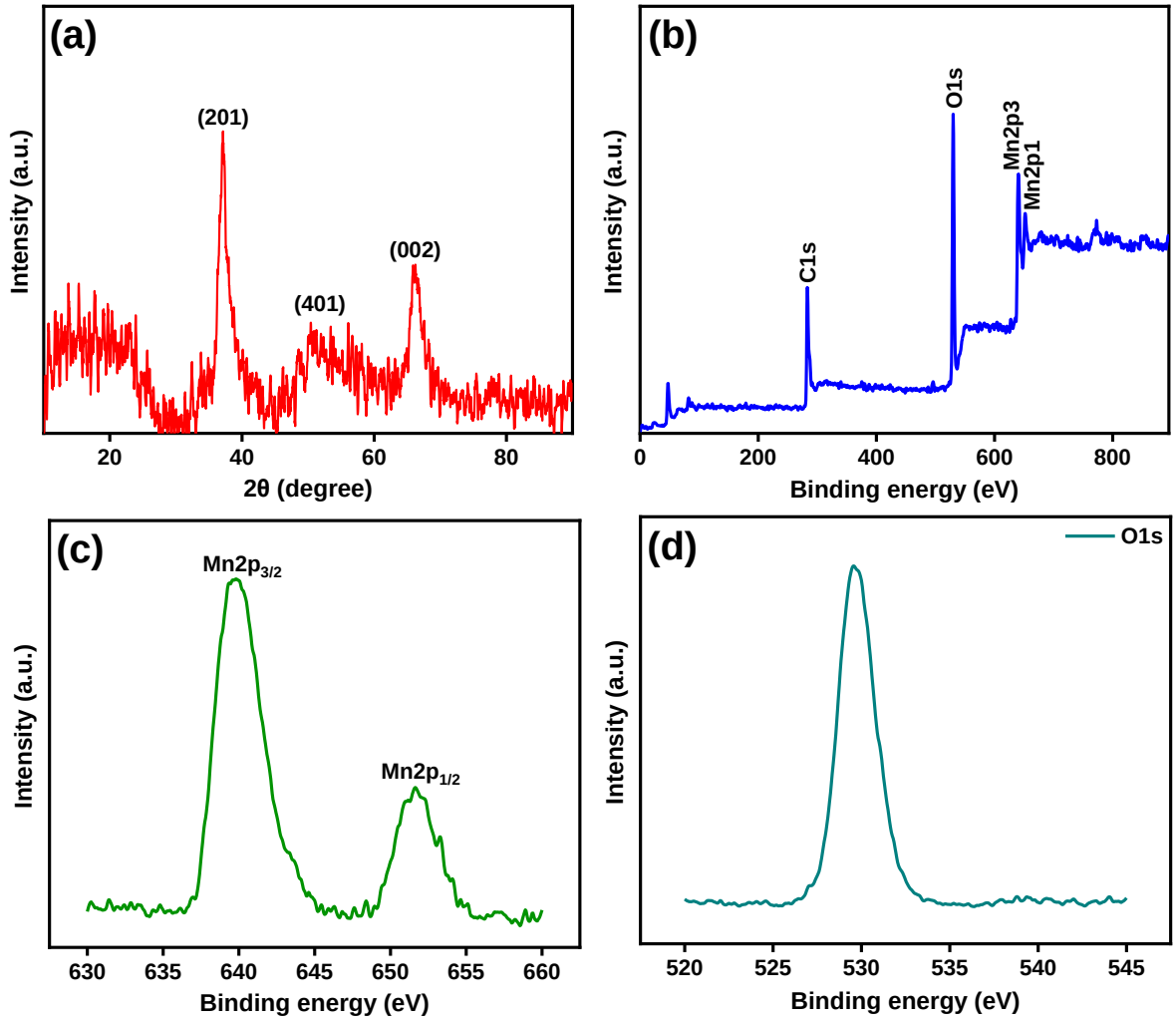

Figure 6.3: (a) XRD pattern, (b) XPS survey spectrum, (c) XPS graph of Mn2p and (d) O1s of CA-MnO_2 QDs.

6.3.2 Optical properties

CA-MnO_2 QDs were prepared from bulk MnO_2 nanomaterial in the presence of citric acid by continuous ultrasonication of 10 h. Similarly, MnO_2 QDs were also prepared in the presence of other reductive biomolecules such as Cys, GSH, and AA. The influence of citric acid and other biomolecules on the photophysical properties of MnO_2 QDs was analyzed by UV-visible spectrum and PL emission spectra. Figure 6.4(a) shows the bar graph of MnO_2 QDs functionalized with different biomolecules. Among all different functionalized MnO_2 QDs, the CA-MnO_2 QDs showed a high PL intensity (Figure 6.4(b)). This indicates that citric acid provides a more stabilizing environment in the enhancement of fluorescence of MnO_2 QDs as compared to the other biomolecules. Figure 6.4(c) displays the UV-Vis absorbance, excitation, and emission spectra of CA-MnO_2 QDs, which consist of peaks near about 245 nm, 300 nm,

and 420 nm, respectively. Figure 6.4(d) shows the PL emission spectra of CA-MnO_2 QDs when excited at different wavelengths (280-380 nm). The maximum PL emission intensity of CA-MnO_2 QDs was observed with an excitation wavelength of 300 nm. The PL emission peak gets red-shifted from 418 nm to 460 nm, with the variation in the excitation wavelength ranging from 280 to 380 nm. Therefore, CA-MnO_2 QDs showed an excitation-dependent PL emission behaviour which may be due to the quantum confinement effect and surface defects of CA-MnO_2 QDs.[19] The PL quantum yield of the prepared CA-MnO_2 QDs was evaluated to be 13.3 % using equation (1.1), in which quinine sulphate was used as a reference solution.

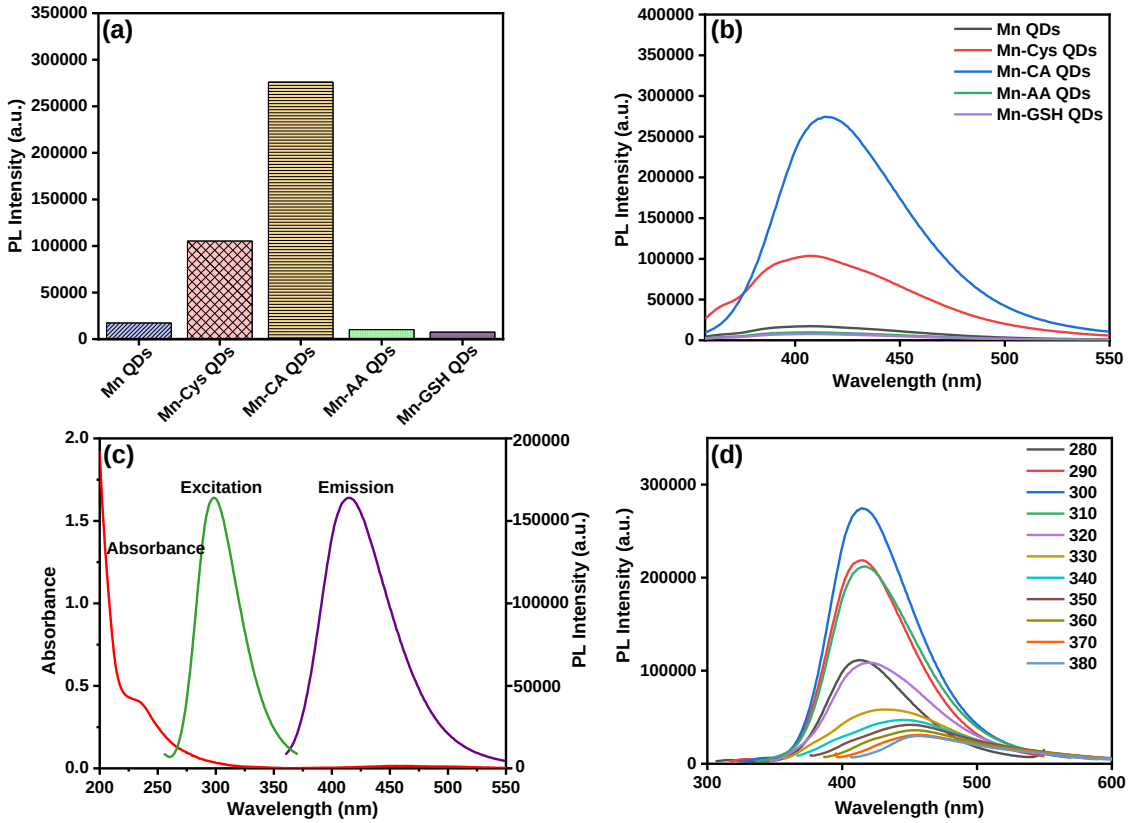

Figure 6.4. (a) Bar graph representing the PL intensity of MnO_2 QDs in the presence of different biomolecules, (b) PL emission spectra of different types of MnO_2 QDs in the presence of various biomolecules, (c) UV-visible absorbance, excitation, and emission spectra of CA-MnO_2 QDs, and (d) PL emission spectra of CA-MnO_2 QDs at different excitation wavelengths.

Further, the PL emission of CA-MnO_2 QDs was observed in the different concentrations of citric acid (Figure 6.5(a)). The PL emission intensity was maximum observed when an equal ratio of MnO_2 and citric acid was added for the preparation of CA-MnO_2 QDs. The PL stability of CA-MnO_2 QDs was also investigated by recording the PL intensity at different irradiation times (Figure 6.5(b)). This shows that the prepared CA-MnO_2 QDs have

high photostability. The PL intensity of prepared CA-MnO_2 QDs was measured at different pH range from 2 to 12 (Figure 6.5(c)). It was found that the PL intensity gets increased from the pH value of 2 to 4, further, it becomes constant up to 9 pH value, and then it gets decreased from 10 to 12.

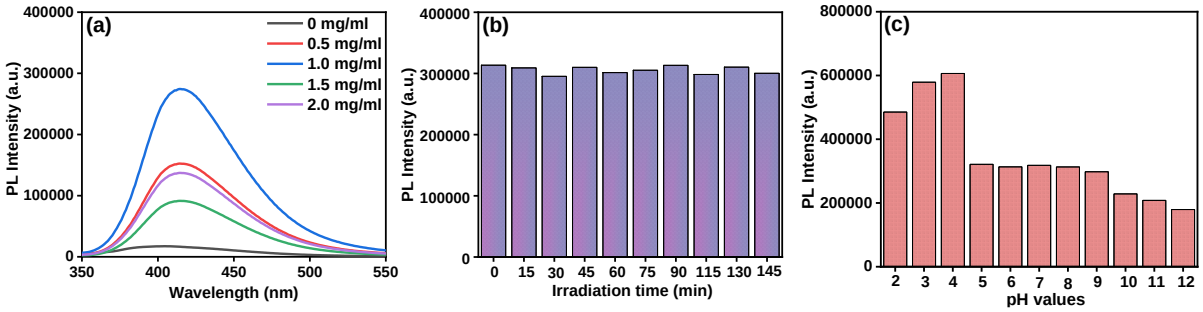

Figure 6.5. (a) PL intensity of CA-MnO_2 QDs with different concentrations of citric acid, (b) bar graph showing the PL intensity of CA-MnO_2 QDs at different irradiation times, and (c) PL intensity of as-prepared CA-MnO_2 QDs at different pH values.

The increase or decrease in the pH values was because of protonation or deprotonation of different emissive traps of CA-MnO_2 QDs, which leads to a change in the PL intensity. Therefore, the pH ranges from 5 to 9 correspond to the buffer zone of the prepared sensing system, which was used for further application. The prepared CA-MnO_2 QDs have shown good photophysical properties, due to which they can be further used for sensing applications.

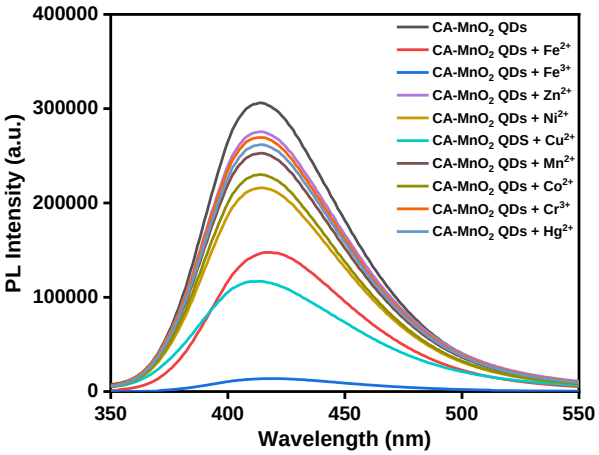

Figure 6.6. PL emission spectra of CA-MnO_2 QDs in the presence of different metal ions.

6.3.3 Sensing of Fe^{3+} ions by CA-MnO_2 QDs

The PL intensity of CA-MnO_2 QDs was measured in the presence of different metal ions (Fe^{2+}, Fe^{3+}, Zn^{2+}, Ni^{2+}, Cu^{2+}, Mn^{2+}, Co^{2+}, Cr^{3+}, Hg^{2+}) with a specific concentration (Figure

6.6). The PL intensity of the prepared fluorescent probe gets effectively quenched in the case of Fe^{3+} ions. Further, the relative percentage change in the PL intensity of CA-MnO_2 QDs with the addition of different metal ions was also estimated (Figure 6.7(a)). It was observed that the CA-MnO_2 QDs-Fe^{3+} system has 4.7 % PL intensity w.r.t. CA-MnO_2 QDs (100 %). This may be due to the formation of a coordination complex between CA-MnO_2 QDs and Fe^{3+} ions.

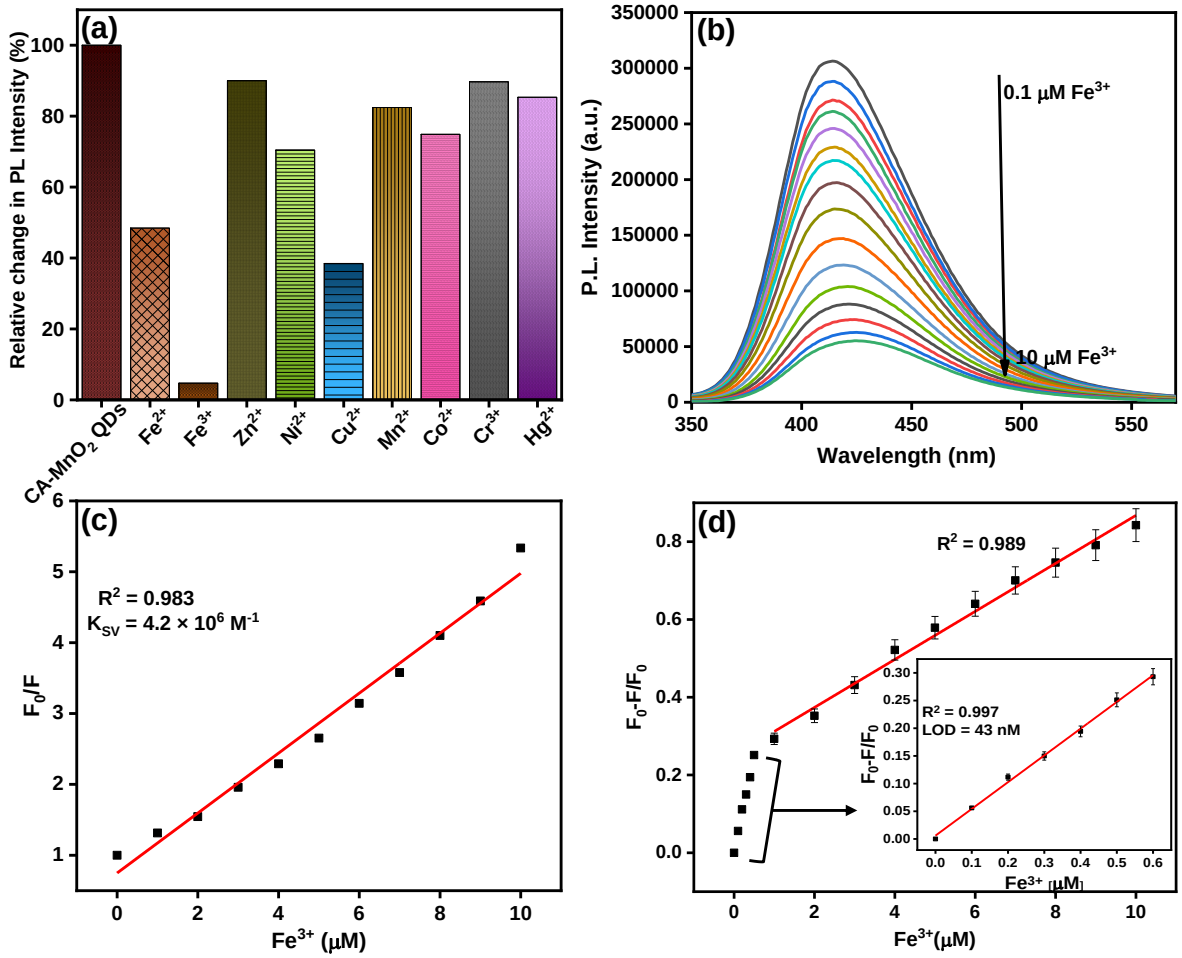

Figure 6.7. (a) Relative percentage change in PL intensity of CA-MnO_2 QDs in the presence of different metal ions, (b) variation of PL intensity of CA-MnO_2 QDs in the presence of different concentrations of Fe^{3+} ions, (c) Stern-Volmer plot between F_0/F and different concentrations of Fe^{3+} ions, and (d) a linear relationship between PL responses (F_0-F/F_0) and various concentrations of Fe^{3+} ions (0-10 μM) with inset image of a linear relationship between PL responses (F_0-F/F_0) and various concentrations of Fe^{3+} ions (0-0.6 μM).

To demonstrate the sensitivity of prepared CA-MnO_2 QDs for Fe^{3+} ions the different concentrations (0.1 μM to 10 μM) of Fe^{3+} ions were added to the prepared fluorescent probe. Figure 6.7(b) represents that the PL intensity of CA-MnO_2 QDs was reduced by increasing the concentration of Fe^{3+} ions in the sensing system. The Stern-Volmer graph was plotted to examine and comprehend the PL quenching behavior of the prepared fluorescent sensing probe (CA-MnO_2 QDs) with the addition of Fe^{3+} ions as a quencher. Figure 6.7(c) shows a linear

Stern–Volmer plot between the PL responses (F_0/F) and different concentrations of Fe^{3+} ions based on the relation in which F_0 and F are PL intensities of CA-MnO_2 QDs without and with the addition of Fe^{3+} ions. The Stern-Volmer constant was calculated to be 4.2×10^6 M^{-1} with the R^2 value of 0.983 from Figure 6.7(c). Figure 6.7(d) shows a linear plot between PL responses (F_0-F/F_0) and various concentrations of Fe^{3+} ions (0 µM to 10 µM) with the R^2 value of 0.989. The inset image of Figure 6.7(d) shows a linear relationship between the PL responses (F_0-F/F_0) and different concentrations of Fe^{3+} ions (0 µM to 0.6 µM) with the value of R^2 i.e., 0.997. From the above plot, the limit of detection (LOD) for Fe^{3+} was calculated to be 43 nM. The prepared CA-MnO_2 QDs show an outstanding LOD value in comparison with other sensing platforms (Table 6.1).

Table 6.1: The different sensing platforms for the detection of Fe^{3+} ions and AA with LODs values.

	Sensing Systems	Detection Range	LOD	Ref.
Detection of Fe^{3+}	Nitrogen, Sulfur-doped Carbon dots	0-500 µM	0.2 µM	[20]
	Cranberry Beans Derived Carbon Dots	30-600 µM	9.55 µM	[21]
	Nitrogen, Phosphorous-doped Carbon dots	20–200 µM	20 µM	[22]
	MoS_2 quantum dots	0-50 µM	1 µM	[23]
	D-Penicillamine functionalized GQDs	0.004-1.8 mM	1.2 µM	[24]
	Boron, Nitrogen, Sulfur-doped Carbon dots	0.3–546 µM	0.09 µM	[25]
	Rhodamine B derivative-functionalized GQDs	0-65 µM	0.02 µM	[26]
	Citric acid functionalized MnO_2 quantum dots	0-10 µM	43 nM	Present work
Detection of AA	Nitrogen, Sulfur-Carbon dots	10-200 µM	4.69 µM	[27]
	rGO-SnO_2/GCE	400-1600 µM	38.7 µM	[28]
	Pt/CeO_2	0.5-30 µM	80 nM	[29]
	Flake hexagonal boron nitride	30-1000 µM	3.77 µM	[30]
	Microporous sulfur-doped carbon microspheres	10-50 µM	1 µM	[31]
	Ferrocene derivative stabilized Au NPs/carbon dots nanocomposite with graphene glassy carbon electrode	8-180 µM	1 µM	[32]
	Carbon dots-MnO_2 nanosheet	0-80 µM	2.89 µM	[33]
	Citric acid functionalized MnO_2 quantum dots	0-25 µM	90 nM	Present work

6.3.4 Sensing of Ascorbic acid

Ascorbic acid act as a brilliant natural antioxidant and a good reducing agent for the reduction of Fe^{3+} to Fe^{2+}.[16] It was observed from the above studies that the PL intensity of CA-MnO_2 QDs gets quenched highly in the case of Fe^{3+} as compared to Fe^{2+}. Therefore, CA-MnO_2 QDs can become an efficient sensing platform for the detection of AA based on the "turn-off-on" approach. The quenched PL intensity of the CA-MnO_2 QDs-Fe^{3+} sensing system was recovered by the addition of AA. Figure 6.8 shows the PL intensity of the CA-MnO_2 QDs-Fe^{3+} sensing system in the presence of different analytes such as AA, GSH, diphenylcarbzide (DPC), DA, Potassium hydrogen phosphate (monobasic) (M-PO_4), Potassium dihydrogen phosphate (dibasic) (M-PO_4), ethylenediaminetetraacetic acid (EDTA), sodium fluoride (NaF), Glu, Cys, Met, melamine (Mel), Glu acid, and thiourea.

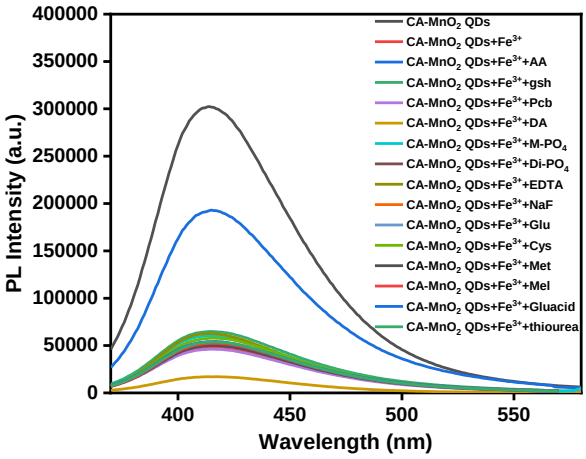

Figure 6.8. Selectivity graph of CA-MnO_2 QDs-Fe^{3+} sensing system.

Figure 6.9(a) exhibits a bar graph in which the PL intensity of CA-MnO_2 QDs-Fe^{3+} gets highly recovered in the presence of AA as compared to the other analytes. The fluorescence restoration of CA-MnO_2 QDs was obtained by the addition of different concentrations of AA in the CA-MnO_2 QDs-Fe^{3+} sensing system (Figure 6.9(b)). This shows that the increase in the concentration of AA in the CA-MnO_2 QDs-Fe^{3+} sensing system results in gradual fluorescence enhancement ("turn-on") of CA-MnO_2 QDs. The PL intensity was 80% recovered with the addition of 25 µM of AA and further, no change was observed in PL intensity of CA-MnO_2 QDs by increasing the concentration of AA. Figure 6.9(c) shows a linear fit plot of PL responses ($F-F_0/F_0$) with concentration of AA (0-25 µM) with a linear equation $F-F_0/F_0$ = 0.124[AA] + 0.828 (R^2 = 0.989). The inset image of Figure 6.9(c) illustrates a linear relationship between PL responses ($F-F_0/F_0$) and at lower concentrations of AA (0-1.0 µM)

with the linear equation $F\text{-}F_0/F_0 = 1.126[AA] + 0.016$ ($R^2 = 0.996$). It shows an excellent LOD value, i.e., 90 nM for AA. In comparison with various sensing probes, the prepared sensing system showed the best LOD value (Table 6.1).

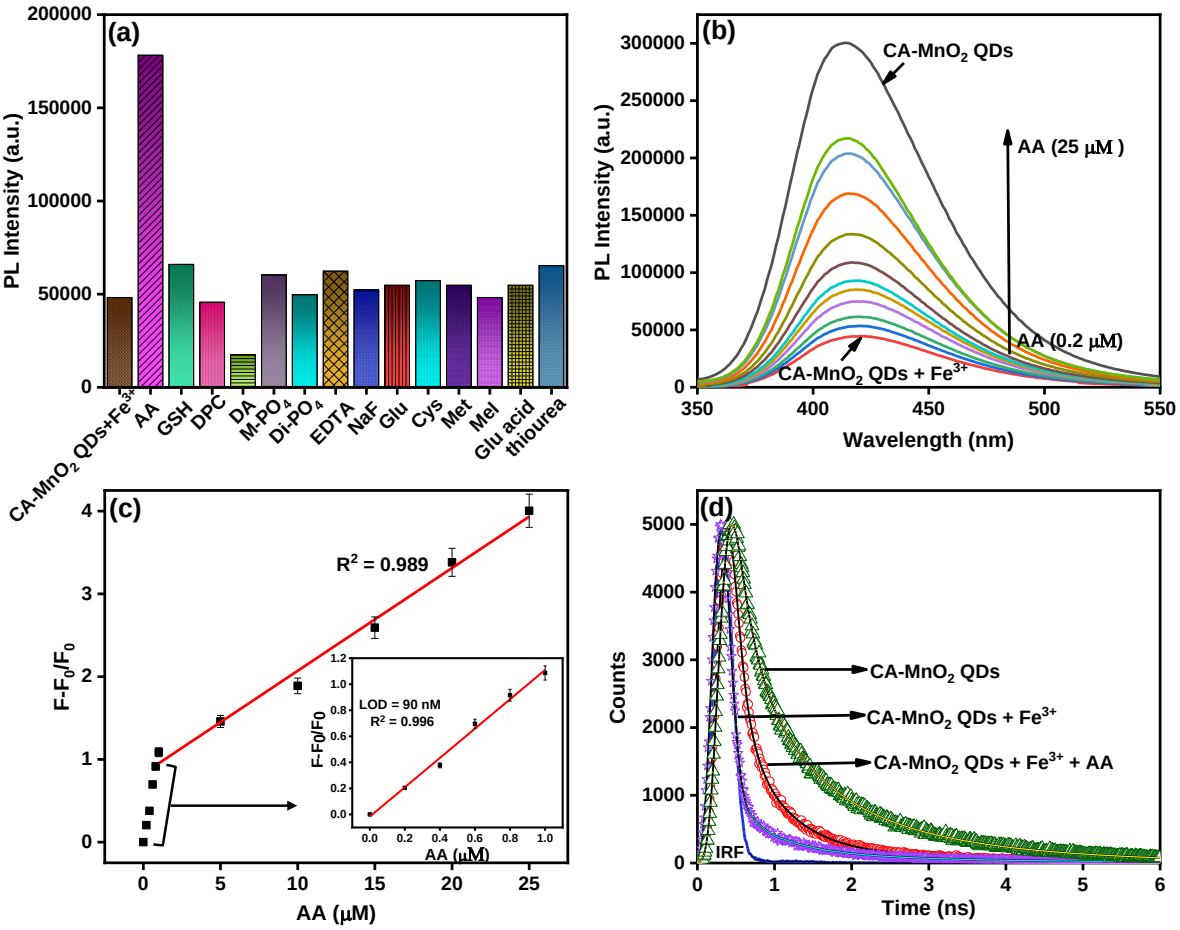

Figure 6.9. (a) Selectivity bar graph of CA-MnO_2 QDs-Fe^{3+} sensing system for the detection of AA, (b) The variation in PL intensity of CA-MnO_2 QDs-Fe^{3+} with the addition of AA, (c) A linear relationship of PL responses ($F\text{-}F_0/F_0$) vs concentration of AA (0-25 µM) and inset image of shows a linear plot of PL responses ($F\text{-}F_0/F_0$) and different concentrations of AA (0-1.0 µM), and (d) Fluorescence lifetime decays of CA-MnO_2 QDs in the presence of Fe^{3+} ions and AA.

Table 6.2: The average lifetime values of different systems.

Systems	a_1	τ_1	a_2	τ_2	a_3	τ_3	$\#<\tau_{av}>$
CA-MnO_2 QDs	0.14	0.89	0.30	3.35	0.56	9.21	6.29
CA-MnO_2 QDs+Fe^{3+}	0.66	0.09	0.13	1.82	0.21	6.84	1.73
CA-MnO_2 QDs+Fe^{3+}+AA	0.22	0.43	0.33	2.30	0.45	8.44	4.65

$\#<\tau_{av}> = a_1\tau_1+a_2\tau_2+a_3\tau_3$

6.3.5 Plausible Mechanism

The PL quenching mechanism for a fluorescent molecule in the presence of hindering molecules is mostly static or dynamic quenching.[12] The high PL intensity of CA-MnO_2 QDs gets quenched in the presence of Fe^{3+} ions (quencher). The static quenching occurs when the interaction between fluorescent molecule and quencher results in the formation of a non-fluorescent complex in the ground state.[19] While, the dynamic quenching occurs due to the collision of fluorescent molecule and quencher in the excited state, and then complex come back to the ground state by charge transfer.[34] In the case of static quenching, the ratio of fluorescence lifetime of the excited state to the ground state is equal to unity ($\tau_0/\tau = 1$). In dynamic quenching the fluorescence lifetime changes in the presence and absence of a quencher. The time-resolved lifetime measurements of CA-MnO_2 QDs without and with the addition of Fe^{3+} ions showed variation in the average lifetime (Figure 6.9(d)) (Table 6.2). The average lifetime of CA-MnO_2 QDs was found to be 6.29 ns, which demonstrates a very fast exciton recombination process. Further, the average lifetime of CA-MnO_2 QDs was found to be 1.73 ns after the addition of Fe^{3+} ions. This indicates that the fluorescence quenching mechanism between the CA-MnO_2 QDs and Fe^{3+} ions is dynamic quenching. The dynamic quenching mechanism can be attributed to the charge transfer process in the excited state, which occurs from the surface of CA-MnO_2 QDs to the half-filled 3d orbital of Fe^{3+} ions. The prepared CA-MnO_2 QDs contain oxygen-functionalized groups on their surface, which were confirmed by XPS analysis. This leads to the binding of Fe^{3+} ions on the surface of CA-MnO_2 QDs, which results in non-radiative electron-hole recombination annihilation and further, it shows the fluorescence quenching.[35] Fe^{3+} ions exhibited a great chelating speed for the development of a chelation or coordination complex in comparison with the other metal ions because of large thermodynamic affinity.[36]

Moreover, to demonstrate the fluorescence quenching mechanism, the radiative (k_r) and non-radiative (k_{nr}) rate constants were calculated through the equation (1.2 and 1.3). The values of k_r and k_{nr} values are mentioned in Table 6.3. The value of k_r gets decreased, whereas the value of k_{nr} gets increased with the addition of Fe^{3+} ions in the CA-MnO_2 QDs. This results suggest that the fluorescence quenching mechanism is based on the excited-state electron transfer.[2] The rate of electron transfer (k_{ET}) was estimated to find the excited-state dynamics of the prepared sensing system via the equation (1.6). The electron transfer efficiency (Φ_{EET}) is determined through the equation (1.7). The effective values of k_{ET} and Φ_{EET} leads to the transfer of electron in the excited state that results in dynamic quenching among the CA-MnO_2 QDs

and Fe^{3+} ions (Table 6.3). The addition of AA in the CA-MnO_2 QDs-Fe^{3+} sensing system leads to the fluorescence recovery of CA-MnO_2 QDs, which was also confirmed by the fluorescence quantum yield and average lifetime values (Table 6.3). The increase in the value of k_r and decrease in the value of k_{nr} shows the removal of Fe^{3+} ions from the surface of the CA-MnO_2 QDs. Furthermore, the variation in the values of k_{ET} and Φ_{EET} with the addition of AA in CA-MnO_2 QDs-Fe^{3+} demonstrates the interruption of the energy-transfer process. This was due to a redox reaction between the AA and Fe^{3+} ions, which leads to the reduction of Fe^{3+} ions to Fe^{2+} ions by AA.[37]

Table 6.3. The photophysical parameters of CA-MnO_2 QDs with the addition of Fe^{3+}ions and AA.[i]

System	Φ	#<τ_{av}> (ns)	k_r (10^9 s^{-1})	k_{nr} (10^9 s^{-1})	k_{ET} (10^9 s^{-1})	Φ_{EET} (τ_D)	Φ_{EET} (Φ_D)
CA-MnO_2 QDs	0.133	6.29	0.021	0.137	-	-	-
CA-MnO_2 QDs + Fe^{3+}	0.020	1.73	0.011	0.567	0.42	0.72	0.850
CA-MnO_2 QDs + Fe^{3+} +AA	0.090	4.65	0.019	0.196	0.06	0.26	0.324

[i]Experimental error ±5 %, #<τ_{av}> =$a_1\tau_1+a_2\tau_2+a_3\tau_3$

6.3.6 Real sample analysis

Table 6.4. Determination of Fe^{3+} ions and AA by using prepared sensing system.[k]

Sample	Amount added to our system	Amount detected by our system	Recovery error (%)	Recovery rate (%)	RSD (%)
Iron supplement	0.5 µM	0.51 µM	1.96	102.0	1.77
	1.0 µM	0.99 µM	1.00	99.0	1.45
	2.5 µM	2.44 µM	2.40	97.6	1.66
Vitamin C supplement	1 µM	0.98 µM	1.02	98.0	1.27
	5 µM	5.10 µM	1.96	102.0	1.02
	10 µM	9.96 µM	0.40	99.6	1.81

[k]Experimental error ±5 %

The practicability of our prepared CA-MnO_2 QDs for the detection of Fe^{3+} ions and AA in a real sample was analyzed. The iron supplement (Fericit (ferric citrate), Septalyst) and vitamin C supplement (Limcee Vitamin C 500 mg) was bought from the local market. The above iron supplement contains 210 mg of iron and the vitamin C supplement contains 500 mg of ascorbic

acid. The values of recovery rate (%), recovery error (%), relative standard deviation (RSD) is summarized in Table 6.4, which shows that the experiment has given satisfactory results for practical applications. These results demonstrated that this PL "turn-off-on" sensor based on CA-MnO_2 QDs is applicable for real sample analysis.

Conclusion

In this Chapter, citric acid-functionalized MnO_2 quantum dots (CA-MnO_2 QDs) have been successfully developed by using bulk MnO_2 as a precursor and citric acid as an exfoliating agent. The morphology and size of the prepared CA-MnO_2 QDs were confirmed by TEM images and their surface composition was determined by XPS analysis. The synthesized CA-MnO_2 QDs show high PL intensity and excitation-dependent fluorescence behavior due to variation in the particle size and surface defects. CA-MnO_2 QDs exhibited good fluorescence quantum yield, high photostability, good pH stability within the range of 5-9, and high aqueous solubility. CA-MnO_2 QDs were used as a "turn-off" sensor for the detection of Fe^{3+} ions with a limit of detection of 43 nM. The decrease in the value of fluorescence quantum yield and the average lifetime of CA-MnO_2 QDs in the presence of Fe^{3+} ions confirmed the dynamic quenching mechanism between the CA-MnO_2 QDs and Fe^{3+} ions. Further, the different photophysical parameters were also calculated which explain the proposed fluorescence quenching mechanism in detail. The PL intensity of CA-MnO_2 QDs was restored ("turn-on") with the addition of AA in the prepared CA-MnO_2 QDs-Fe^{3+} sensing probe based on the redox reaction. The facile, cost-effective, fast, and environmentally friendly prepared sensing probe was also used in real sample analysis.

References

(1) Tehseen, B.; Rehman, A.; Rahmat, M.; Bhatti, H. N.; Wu, A.; Butt, F. K.; Naz, G.; Khan, W. S.; Bajwa, S. Z. Solution Growth of 3D MnO_2 Mesh Comprising 1D Nanofibres as a Novel Sensor for Selective and Sensitive Detection of Biomolecules. *Biosens. Bioelectron.* **2018**, *117*, 852–859. https://doi.org/10.1016/j.bios.2018.06.061.

(2) Sohal, N.; Maity, B.; Basu, S. Morphology-Dependent Performance of MnO_2 Nanostructure–Carbon Dot-Based Biosensors for the Detection of Glutathione. *ACS Appl. Bio Mater.* **2021**, *4* (6), 5158–5168. https://doi.org/10.1021/acsabm.1c00353.

(3) Yan, X.; Song, Y.; Zhu, C.; Song, J.; Du, D.; Su, X.; Lin, Y. Graphene Quantum Dot-MnO_2 Nanosheet Based Optical Sensing Platform: A Sensitive Fluorescence "Turn Off-

On" Nanosensor for Glutathione Detection and Intracellular Imaging. *ACS Appl. Mater. Interfaces* **2016**, *8* (34), 21990–21996. https://doi.org/10.1021/acsami.6b05465.

(4) Wang, Y.; Jiang, K.; Zhu, J.; Zhang, L.; Lin, H. A FRET-Based Carbon Dot–MnO_2 Nanosheet Architecture for Glutathione Sensing in Human Whole Blood Samples. *Chem. Commun.* **2015**, *51* (64), 12748–12751. https://doi.org/10.1039/C5CC04905A.

(5) Ma, Z.; Sun, Y.; Xie, J.; Li, P.; Lu, Q.; Liu, M.; Yin, P.; Li, H.; Zhang, Y.; Yao, S. Facile Preparation of MnO_2 Quantum Dots with Enhanced Fluorescence via Microenvironment Engineering with the Assistance of Some Reductive Biomolecules. *ACS Appl. Mater. Interfaces* **2020**, *12* (13), 15919–15927. https://doi.org/10.1021/acsami.0c00917.

(6) Zhang, L.-J.; Xia, L.; Xie, H.-Y.; Zhang, Z.-L.; Pang, D.-W. Quantum Dot Based Biotracking and Biodetection. *Anal. Chem.* **2019**, *91* (1), 532–547. https://doi.org/10.1021/acs.analchem.8b04721.

(7) Kloberg, M. J.; Yu, H.; Groß, E.; Eckmann, F.; Restle, T. M. F.; Fässler, T. F.; Veinot, J. G. C.; Rieger, B. Surface-Anisotropic Janus Silicon Quantum Dots via Masking on 2D Silicon Nanosheets. *Adv. Mater.* **2021**, *33* (38), 2100288. https://doi.org/10.1002/adma.202100288.

(8) Guan, Q.; Ma, J.; Yang, W.; Zhang, R.; Zhang, X.; Dong, X.; Fan, Y.; Cai, L.; Cao, Y.; Zhang, Y.; Li, N.; Xu, Q. Highly Fluorescent Ti_3C_2 MXene Quantum Dots for Macrophage Labeling and Cu^{2+} Ion Sensing. *Nanoscale* **2019**, *11* (30), 14123–14133. https://doi.org/10.1039/C9NR04421C.

(9) Kundu, S.; Ghosh, M.; Sarkar, N. State of the Art and Perspectives on the Biofunctionalization of Fluorescent Metal Nanoclusters and Carbon Quantum Dots for Targeted Imaging and Drug Delivery. *Langmuir* **2021**, *37* (31), 9281–9301. https://doi.org/10.1021/acs.langmuir.1c00732.

(10) Mirnajafizadeh, F.; Ramsey, D.; McAlpine, S.; Wang, F.; Reece, P.; Stride, J. A. Hydrothermal Synthesis of Highly Luminescent Blue-Emitting ZnSe(S) Quantum Dots Exhibiting Low Toxicity. *Mater. Sci. Eng. C* **2016**, *64*, 167–172. https://doi.org/10.1016/j.msec.2016.03.061.

(11) Khan, T.; Vaidya, S.; Mhatre, D. S.; Datta, A. The Prospect of Salophen in Fluorescence Lifetime Sensing of Al^{3+}. *J. Phys. Chem. B* **2016**, *120* (39), 10319–10326.

https://doi.org/10.1021/acs.jpcb.6b05854.

(12) Sohal, N.; Bhatia, S. K.; Basu, S.; Maity, B. Nanomolar Level Detection of Metal Ions by Improving the Monodispersity and Stability of Nitrogen-Doped Graphene Quantum Dots. *New J. Chem.* **2021**, *45* (42), 19941–19949. https://doi.org/10.1039/D1NJ04551B.

(13) Li, S.; Li, Y.; Cao, J.; Zhu, J.; Fan, L.; Li, X. Sulfur-Doped Graphene Quantum Dots as a Novel Fluorescent Probe for Highly Selective and Sensitive Detection of Fe^{3+}. *Anal. Chem.* **2014**, *86* (20), 10201–10207. https://doi.org/10.1021/ac503183y.

(14) Peng, J.; Ling, J.; Zhang, X.-Q.; Zhang, L.-Y.; Cao, Q.-E.; Ding, Z.-T. A Rapid, Sensitive and Selective Colorimetric Method for Detection of Ascorbic Acid. *Sensors Actuators B Chem.* **2015**, *221*, 708–716. https://doi.org/10.1016/j.snb.2015.07.002.

(15) Meng, H.; Yang, D.; Tu, Y.; Yan, J. Turn-on Fluorescence Detection of Ascorbic Acid with Gold Nanolcusters. *Talanta* **2017**, *165*, 346–350. https://doi.org/10.1016/j.talanta.2016.12.047.

(16) Lv, X.; Man, H.; Dong, L.; Huang, J.; Wang, X. Preparation of Highly Crystalline Nitrogen-Doped Carbon Dots and Their Application in Sequential Fluorescent Detection of Fe^{3+} and Ascorbic Acid. *Food Chem.* **2020**, *326*, 126935. https://doi.org/10.1016/j.foodchem.2020.126935.

(17) Feng, J.-J.; Zhang, P.-P.; Wang, A.-J.; Zhang, Y.; Dong, W.-J.; Chen, J.-R. One-Pot Hydrothermal Synthesis of Uniform β-MnO_2 Nanorods for Nitrite Sensing. *J. Colloid Interface Sci.* **2011**, *359* (1), 1–8. https://doi.org/10.1016/j.jcis.2011.03.087.

(18) Rivera-Quintero, P. A.; Mercado, D. F.; Ballesteros-Rueda, L. M. Influence of the Functionalization Agent and Crystalline Phase of MnO_2 Janus Nanomaterials on the Stability of Aqueous Nanofluids and Its Catalytic Activity to Promote Asphaltene Oxidation. *Colloid Interface Sci. Commun.* **2021**, *45*, 100525. https://doi.org/10.1016/j.colcom.2021.100525.

(19) Sohal, N.; Maity, B.; Basu, S. Recent Advances in Heteroatom-Doped Graphene Quantum Dots for Sensing Applications. *RSC Adv.* **2021**, *11* (41), 25586–25615. https://doi.org/10.1039/D1RA04248C.

(20) Sun, C.; Zhang, Y.; Wang, P.; Yang, Y.; Wang, Y.; Xu, J.; Wang, Y.; Yu, W. W. Synthesis of Nitrogen and Sulfur Co-Doped Carbon Dots from Garlic for Selective

Detection of Fe^{3+}. *Nanoscale Res. Lett.* **2016**, *11* (1), 110. https://doi.org/10.1186/s11671-016-1326-8.

(21) Zulfajri, M.; Gedda, G.; Chang, C.-J.; Chang, Y.-P.; Huang, G. G. Cranberry Beans Derived Carbon Dots as a Potential Fluorescence Sensor for Selective Detection of Fe^{3+} Ions in Aqueous Solution. *ACS Omega* **2019**, *4* (13), 15382–15392. https://doi.org/10.1021/acsomega.9b01333.

(22) Chandra, S.; Laha, D.; Pramanik, A.; Ray Chowdhuri, A.; Karmakar, P.; Sahu, S. K. Synthesis of Highly Fluorescent Nitrogen and Phosphorus Doped Carbon Dots for the Detection of Fe^{3+} Ions in Cancer Cells. *Luminescence* **2016**, *31* (1), 81–87. https://doi.org/10.1002/bio.2927.

(23) Ma, J.; Yu, H.; Jiang, X.; Luo, Z.; Zheng, Y. High Sensitivity Label-Free Detection of Fe^{3+} Ion in Aqueous Solution Using Fluorescent MoS_2 Quantum Dots. *Sensors Actuators B Chem.* **2019**, *281*, 989–997. https://doi.org/10.1016/j.snb.2018.11.039.

(24) Xuan, W.; Ruiyi, L.; Saiying, F.; Zaijun, L.; Guangli, W.; Zhiguo, G.; Junkang, L. D-Penicillamine-Functionalized Graphene Quantum Dots for Fluorescent Detection of Fe^{3+} in Iron Supplement Oral Liquids. *Sensors Actuators B Chem.* **2017**, *243*, 211–220. https://doi.org/10.1016/j.snb.2016.11.150.

(25) Liu, Y.; Duan, W.; Song, W.; Liu, J.; Ren, C.; Wu, J.; Liu, D.; Chen, H. Red Emission B, N, S- Co -Doped Carbon Dots for Colorimetric and Fluorescent Dual Mode Detection of Fe^{3+} Ions in Complex Biological Fluids and Living Cells. *ACS Appl. Mater. Interfaces* **2017**, *9* (14), 12663–12672. https://doi.org/10.1021/acsami.6b15746.

(26) Guo, R.; Zhou, S.; Li, Y.; Li, X.; Fan, L.; Voelcker, N. H. Rhodamine-Functionalized Graphene Quantum Dots for Detection of Fe^{3+} in Cancer Stem Cells. *ACS Appl. Mater. Interfaces* **2015**, *7* (43), 23958–23966. https://doi.org/10.1021/acsami.5b06523.

(27) Luo, X.; Zhang, W.; Han, Y.; Chen, X.; Zhu, L.; Tang, W.; Wang, J.; Yue, T.; Li, Z. N,S Co-Doped Carbon Dots Based Fluorescent “on-off-on” Sensor for Determination of Ascorbic Acid in Common Fruits. *Food Chem.* **2018**, *258*, 214–221. https://doi.org/10.1016/j.foodchem.2018.03.032.

(28) Sha, R.; Badhulika, S. Facile Green Synthesis of Reduced Graphene Oxide/Tin Oxide Composite for Highly Selective and Ultra-Sensitive Detection of Ascorbic Acid. *J.*

Electroanal. Chem. **2018**, *816*, 30–37. https://doi.org/10.1016/j.jelechem.2018.03.033.

(29) Liu, X.; Wang, X.; Qi, C.; Han, Q.; Xiao, W.; Cai, S.; Wang, C.; Yang, R. Sensitive Colorimetric Detection of Ascorbic Acid Using Pt/CeO_2 Nanocomposites as Peroxidase Mimics. *Appl. Surf. Sci.* **2019**, *479*, 532–539. https://doi.org/10.1016/j.apsusc.2019.02.135.

(30) Li, Q.; Huo, C.; Yi, K.; Zhou, L.; Su, L.; Hou, X. Preparation of Flake Hexagonal BN and Its Application in Electrochemical Detection of Ascorbic Acid, Dopamine and Uric Acid. *Sensors Actuators B Chem.* **2018**, *260*, 346–356. https://doi.org/10.1016/j.snb.2017.12.208.

(31) Emran, M. Y.; Shenashen, M. A.; Abdelwahab, A. A.; Abdelmottaleb, M.; El-Safty, S. A. Facile Synthesis of Microporous Sulfur-Doped Carbon Spheres as Electrodes for Ultrasensitive Detection of Ascorbic Acid in Food and Pharmaceutical Products. *New J. Chem.* **2018**, *42* (7), 5037–5044. https://doi.org/10.1039/C7NJ05047J.

(32) Yang, L.; Huang, N.; Lu, Q.; Liu, M.; Li, H.; Zhang, Y.; Yao, S. A Quadruplet Electrochemical Platform for Ultrasensitive and Simultaneous Detection of Ascorbic Acid, Dopamine, Uric Acid and Acetaminophen Based on a Ferrocene Derivative Functional Au NPs/Carbon Dots Nanocomposite and Graphene. *Anal. Chim. Acta* **2016**, *903*, 69–80. https://doi.org/10.1016/j.aca.2015.11.021.

(33) Wang, H.; Na, X.; Liu, S.; Liu, H.; Zhang, L.; Xie, M.; Jiang, Z.; Han, F.; Li, Y.; Cheng, S.; Tan, M. A Novel "Turn-on" Fluorometric and Magnetic Bi-Functional Strategy for Ascorbic Acid Sensing and in Vivo Imaging via Carbon Dots-MnO_2 Nanosheet Nanoprobe. *Talanta* **2019**, *201*, 388–396. https://doi.org/10.1016/j.talanta.2019.04.022.

(34) Zu, F.; Yan, F.; Bai, Z.; Xu, J.; Wang, Y.; Huang, Y.; Zhou, X. The Quenching of the Fluorescence of Carbon Dots: A Review on Mechanisms and Applications. *Microchim. Acta* **2017**, *184* (7), 1899–1914. https://doi.org/10.1007/s00604-017-2318-9.

(35) Ma, J.; Yu, H.; Jiang, X.; Luo, Z.; Zheng, Y. High Sensitivity Label-Free Detection of Fe^{3+} Ion in Aqueous Solution Using Fluorescent MoS_2 Quantum Dots. *Sensors Actuators B Chem.* **2019**, *281*, 989–997. https://doi.org/10.1016/j.snb.2018.11.039.

(36) Wang, R.; Fan, H.; Jiang, W.; Ni, G.; Qu, S. Amino-Functionalized Graphene Quantum Dots Prepared Using High-Softening Point Asphalt and Their Application in Fe^{3+}

Detection. *Appl. Surf. Sci.* **2019**, *467–468*, 446–455. https://doi.org/10.1016/j.apsusc.2018.10.104.

(37) Shamsipur, M.; Molaei, K.; Molaabasi, F.; Alipour, M.; Alizadeh, N.; Hosseinkhani, S.; Hosseini, M. Facile Preparation and Characterization of New Green Emitting Carbon Dots for Sensitive and Selective off/on Detection of Fe^{3+} Ion and Ascorbic Acid in Water and Urine Samples and Intracellular Imaging in Living Cells. *Talanta* **2018**, *183*, 122–130. https://doi.org/10.1016/j.talanta.2018.02.042.

CONCLUSIONS AND FUTURE PERSPECTIVES

In summary of thesis, Cdots act as an active fluorescent nanomaterial to be used in the sensing applications due to owing attractive properties such as exceptional biocompatibility, good water solubility, photo-stability, and tunable photoluminescence. Biomolecules have great affinity for metal surfaces. Therefore, the combinations of fluorescent probes and nanomaterial-based quenchers used as promising sensor for the detection of biomolecules. So, MnO_2 nanoparticles with a high specific surface area and great capacity to absorb light can act as efficient fluorescence quencher and used for the development of "turn off−on" fluorescence sensing platforms. The main target of the thesis is to study the role of different sizes of MnO_2 nanospheres and different morphologies of MnO_2 nanostructures for the detection of biomolecules by using fluorescence spectroscopy.

In Chapter 2, the sensors were prepared based on fluorescent nanomaterials i.e., Cdots which were prepared by using ascorbic acid under microwave irradiations. The different sized (large, medium, small) MnO_2 nanospheres were prepared by changing the ratio of $KMnO_4$ (as a precursor) and methionine (as a capping agent) at room temperature. Cdots with large size MnO_2 nanospheres act as the best sensor for GSH detection due to the large size of MnO_2 nanospheres. It can be demonstrated that the sensing activity of prepared sensors was dependent on the size of MnO_2 nanospheres. A redox reaction occurs between GSH and MnO_2 leading to the decomposition of the Cdots-MnO_2 nanocomposite and results in the fluorescence restoration (turn on) of Cdots due to the transformation from MnO_2 to Mn^{2+}. Further, in Chapter 3 the different morphologies (Mn NF, Mn NF+NR, Mn NR) of MnO_2 nanostructure were prepared by hydrothermal method at different reaction times. Mn NF showed high quenching efficiency of Cdots and high fluorescence restoration of Cdots in presence of GSH among different morphologies of MnO_2 nanostructure due to the high surface area of Mn NF. Therefore, the different morphologies of MnO_2 nanostructure also affect the sensing activity of sensors for GSH detection.

In Chapter 4, the role of different heteroatom doped carbon dots in Cdots-MnO_2 based sensor for the detection of GSH were studied in detail. Four different heteroatoms doped Cdots have been synthesized, including U-Cdots, N-Cdots, S-Cdots, and N, S-Cdots by high-temperature treatment for 5 min. N, S-Cdots showed a high value of the quantum yield and attractive properties as compared to others. N, S-Cdots with MnO_2 nanospheres showed a high fluorescence restoration of Cdots as compared to other prepared Cdots due to the synergistic

effect of nitrogen and sulfur. Further, in Chapter 5, the different morphologies of 1-D MnO_2 nanostructures were prepared by using a hydrothermal method by varying the reaction time (8, 10, and 12 h). The variations in the morphology and the aspect ratio of the different 1-D MnO_2 nanostructures were determined by TEM images. MnO_2 nanowires prepared at 8 h showed the best result for the detection of GSH due to the high aspect ratio, large specific surface area, and high surface-to-volume ratio. It can be concluded that the variation in the aspect ratio of MnO_2 nanostructure put an impact on their sensing activity for GSH.

The variation in the different photophysical parameters of Cdots such as quantum yield (ϕ), average lifetime values [τ_{av} (ns)], radiative (k_r) rate constant, non-radiative (k_{nr}) rate constant, rate of electron transfer (k_{ET}), the efficiency of electron transfer (ϕ_{EET}), FRET efficiency (E), and Förster distance (R_0) were dependent on the different shapes and sizes of the MnO_2 nanostructure. The prepared sensors for the detection of GSH were based on different fluorescence quenching mechanisms which were also confirmed by these photophysical parameters. In prepared all above sensors for the GSH detection N, S-Cdots with MnO_2 nanospheres showed the best limit of detection i.e., 80 nM. This may be due to good optical and electronic properties of heteroatom doped Cdots and high surface-to-volume ratio of MnO_2 nanospheres as compared to the other MnO_2 nanostructures.

At last, in Chapter 6, there was an approach to prepare self-fluorescent MnO_2 quantum dots for the detection of biomolecules. Citric acid-functionalized MnO_2 quantum dots (CA-MnO_2 QDs) was prepared through one-step ultrasonication of bulk MnO_2 in the presence of citric acid as acidifying and stabilizing agent. CA-MnO_2 QDs in the presence of Fe^{3+} ions were used as a sensor for the detection of AA based on the redox reaction between Fe^{3+} ions and AA.

Future Perspectives

- Modification in the surface functionalisation of Cdots to enhance the limit of detection for biomolecules.
- Implementation of prepared best sensor in real-time portable sensor.
- The prepared best sensor for the GSH detection can be used in biomedical applications.
- Development of self-fluorescent MnO_2 QDs with other capping molecules for selective sensing of different biomolecules and applicable in biomedical applications.

LIST OF PUBLICATIONS

1. **N. Sohal**, B. Maity, S. Basu, Carbon Dot-MnO_2 Nanosphere Composite Sensors for Selective Detection of Glutathione. *ACS Applied Nano Materials* **2020**, *3*, 5955–5964. https://doi.org/10.1021/acsanm.0c01088 (**I.F. = 6.140**)

2. **N. Sohal**, B. Maity, S. Basu, Morphology-Dependent Performance of MnO_2 Nanostructure–Carbon Dot-Based Biosensors for the Detection of Glutathione. *ACS Applied Bio Materials* **2021**, *4*, 5158–5168. https://doi.org/10.1021/acsabm.1c00353 (**I.F. = Yet to come**)

3. **N. Sohal**, B. Maity, S. Basu, Morphology Effect of One-Dimensional MnO_2 Nanostructures on Heteroatom-Doped Carbon Dot-Based Biosensors for Selective Detection of Glutathione. *ACS Applied Bio Materials* **2022**, *5*, 2355-2364. https://doi.org/10.1021/acsabm.2c00189 (**I.F. = Yet to come**)

4. **N. Sohal**, S. Sharma, D. Choudhury, B. Maity, S. Basu, Deciphering the Mechanism of Inner Filter Effect on Heteroatom Doped Carbon dots-MnO_2 Nanoprobe for Selective Detection of Glutathione and Intracellular Imaging. (**Under Review**)

5. **N. Sohal**, B. Maity, B, S. Basu, Transformation of Bulk MnO_2 to Fluorescent Quantum Dots for Selective and Sensitive Detection of Ferric ions and Ascorbic acid by Turn-Off-On Strategy. *Journal of Photochemistry and Photobiology A: Chemistry*, **2022**, *434*, 114280. https://doi.org/10.1016/j.jphotochem.2022.114280 (**I.F.= 5.141**)

6. **N. Sohal**, B. Maity, N. P. Shetti, S. Basu, Biosensors Based on MnO_2 Nanostructures: A Review. *ACS Applied Nano Materials* **2021**, *4*, 2285-2302. https://doi.org/10.1021/acsanm.0c03380 (**I.F. = 6.140**)

7. P. Sharma, **N. Sohal**, B. Maity, Encapsulation and release of non-fluorescent crystal violet confined in bile-salt aggregates. *RSC Advances* **2021**, *11*, 10912-10921. https://doi.org/10.1039/D0RA06599D (**I.F. = 4.036**)

8. **N. Sohal**, B. Maity, S. Basu, Recent advances in heteroatom-doped graphene quantum dots for sensing applications. *RSC Advances* **2021**, *11*, 25586-2561. https://doi.org/10.1039/D1RA04248C (**I.F. = 4.036**)

9. **N. Sohal**, S. K. Bhatia, S. Basu, B. Maity, Nanomolar level detection of metal ions by improving the monodispersity and stability of nitrogen-doped graphene quantum dots. *New Journal of Chemistry*, **2021**, *45*, 19941-19949. https://doi.org/10.1039/D1NJ04551B (**I.F. = 3.925**)

10. **N. Sohal**, S. Basu, B. Maity, Deciphering the mechanism of undoped and heteroatom doped-carbon dots for detection of lead ions at nanomolar level. **(Under revesion)**

11. **N. Sohal**, S. Singla, S. J. Malode, N. P. Shetti, S. Basu, B. Maity, Bioresource-based graphene quantum dots: An innovative platform for environmental applications. **(Communicated)**

PAPERS PRESENTED IN CONFERENCES /WORKSHOPS ATTENDED

- **Poster Presentation** on "A Rapid Turn off/on Fluorescence Sensor for the Detection of Glutathione Using Carbon dots-MnO_2 Nanocomposites" at the **National Conference, RTCES – 2019 held at Punjabi University, Patiala** in February 2019. (**2nd position**)
- **Oral Presentation** on "Fluorescent sensing platform based on carbon dots-MnO_2 nanospheres for the detection of glutathione" at **International virtual conference ACS SPRING 2021** on April 2021.
- **DST & ACS virtual workshop** "Mastering the publishing process" on July 28, 2020.